Hot electron bolometer sensors for millimetre-wave and terahertz wave detection

by
David Bernard Northeast

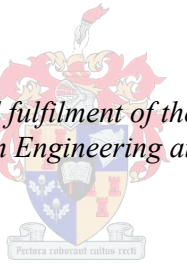

Thesis presented in partial fulfilment of the requirements for the degree
of *Master of Science in Engineering at Stellenbosch University*

Supervisor: Dr. Coenrad Johann Fourie
Department of Electrical & Electronic Engineering

March 2011

Declaration

By submitting this thesis electronically, I declare that the entirety of the work contained therein is my own, original work, that I am the sole author thereof (save to the extent explicitly otherwise stated), that reproduction and publication thereof by Stellenbosch University will not infringe any third party rights and that I have not previously in its entirety or in part submitted it for obtaining any qualification.

Date: 9 February 2011

Abstract

The design and simulation of hot electron bolometer sensors for the detection of millimeter and terahertz wave radiation is presented. These devices can be used for the formation of images or for spectroscopy in these frequency ranges. Many molecules resonate and have absorption spectra over these ranges, allowing for the identification, non-destructively and at a distance, of the constitution of many different materials. The penetrating ability of the radiation makes mm-wave and THz wave detectors ideal for security imaging. The design and simulation of these devices predicts performance as mixers and as interferometers. Manufacturing processes used while fabricating these thin film devices are outlined and experimental results are reported.

Opsomming

Hierdie tesis bespreek die ontwerp en simulasie van warm-elektron bolometers vir die waarneming van millimetergolf- en terahertz-straling. Sodanige toestelle kan in bogenoemde frekwensiebereike gebruik word vir beeldvorming of spektroskopie. Aangesien heelwat molekules binne hierdie bande resoneer, kan die samestelling van 'n verskeidenheid materiale oor 'n afstand en op 'n nie-vernietigende wyse gedentifiseer word. Die deurdringingsvermo van millimetergolf- en terahertz-straling maak sulke detektors ideaal vir beeldvorming in veiligheidstoepassings. Met die ontwerp en simulasie van hierdie toestelle word gewys wat hul werkverrigting as mengers en interferometers kan wees. Die prosesse wat gebruik is om hierdie dunfilmtoestelle mee te vervaardig word ook bespreek en eksperimentele resultate word aangebied.

Acknowledgment

Many people deserve my thanks because, well, if we're not standing on the shoulders of giants, we're at least leaning on a few.

I would like to thank my parents for the support they have provided while I was off adventuring in a far off land. Having the opportunity to live and study abroad was a greatly rewarding experience. I would not trade these memories and this knowledge for mere beans, no sir.

I would also like to thank the various friends who kept me sane and comfortable mostly with the warm embrace of Internet-based communications. From Michelle to Silje, I thank you all earnestly. I realize the chance of you reading this is quite near to zero, but, just in case.

Without Coenrad's suggestions, perspective, and encouragement, this thesis would likely have remained a fragmented and incoherent mess strewn across many notebooks and loose sheets of paper. Many thanks for your guidance.

The E211A crew deserve special regard as well. One can learn a lot, even if they don't want to, just from sitting around with the likes of J.P., Johan, and Jonathan.

Finally, I'd like to thank the various people who, deservedly or undeservedly, feel they are owed thanks too. I appreciate your unknown forthrightness.

Contents

List of Figures

List of Tables

Chapter 1

Introduction

Sensors are a vital component in all science and engineering projects and designs. Without the ability to sense and observe the physical world within a system of interest, any experiment or device we design would be blind and based on potentially incorrect assumptions. Be it a thermocouple that allows one to measure the temperature inside an oven, the human eye that senses select frequencies in the visible band, the human ear that allows detection of certain frequencies of matter waves in a fluid, observing physical phenomena allows us to understand the universe and to exploit this understanding in novel ways.

One of the most important phenomena to detect is the electromagnetic force. It plays a dominant role in physics with dimensions above the nuclear scale and below the gigantic distances found in astrophysics. Detectors sensing electromagnetic radiation in the mm-wave or THz range will enable non-ionizing radiation to create images of objects in a similar manner to X-rays. Additionally, many molecular substances resonate in the THz range, which can potentially allow a detector to determine the chemical composition of an object non-destructively and at a distance [2].

The physics of electromagnetic fields and radiation (with or without matter) depend on factors such as the frequency of the waves and the dimension of any physical system the waves interact with. Sensors must be specifically created to interact with every part of the spectrum (Fig. 1.1) if these differing effects are to be understood.

Superconductors-based devices can allow for the sensitive detection of pho-

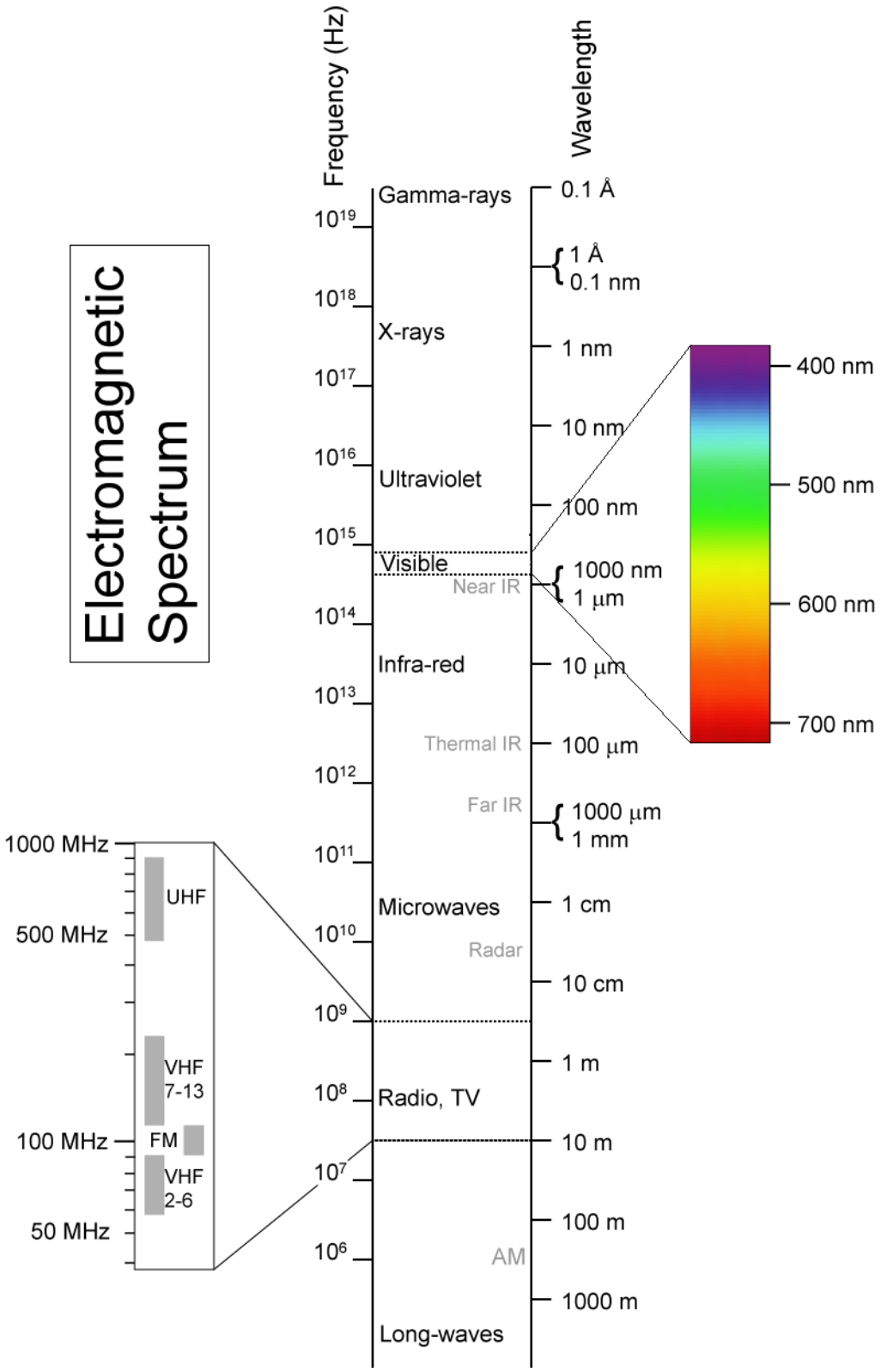

Figure 1.1: The electromagnetic spectrum with common names for frequency bands. Frequency, on the right, is contrasted with the corresponding wavelength in vacuum. Taken from [3].

tons as well as the mixing and detection of signals with frequencies as high as several terahertz (THz). Small continuous or impulse signals can create a large change in the properties of a superconductor, and so these materials can make excellent sensor devices. In scientific fields where technological deficiencies in efficient detectors exist (such as the terahertz regime[1] [4]), superconductors provide a new avenue for research and the creation of useful devices for industry.

Superconducting sensors often rely on changes in properties when superconductivity is broken. The steep change to a resistive mode provides an easily measurable output signal. Devices built on this principle can detect single photons usually of optical wavelengths, but also radiation at higher and lower frequencies. Other detectors use the change in resistance to allow for frequency down-mixing. If a system is biased in the resistive state, then any signal passing through a transitioning superconducting element will cause a nonlinear change in the element's resistance.

This thesis deals with the design and manufacturing of hot electron bolometer (HEB) devices. These devices can be used as frequency mixers to produce an intermediate frequency signal containing the information of a much higher frequency signal. They can also be used to perform spectroscopy, in particular Fourier transform spectroscopy. The design of systems using these two modes of operation is described in subsequent chapters.

1.1 Applications

The applications of hot electron bolometer devices extend to situations that require the detection of millimetre wave (mm-wave) and terahertz wave (THz-wave) radiation. Many molecules have resonant absorption peaks in the mm-wave and THz-wave range. From oxygen gas to many explosive materials [5], these absorbtion spectra provide a chemical fingerprint for material identification. Use as detectors for spectroscopy has been demonstrated [6] using a niobium superconductor as the detection element.

In this frequency range, the waves are known to penetrate clothing and allow for the imaging of concealed objects [4]. In recent years, security at

[1] Often defined from 0.1 THz to 10 THz.

airports and other buildings have begun using technology to create images of visitors for the purposes of detecting hidden threats. Similar to X-rays, that have the ability to deeply penetrate and help form images of the inside of objects, mm-waves and THz-waves also penetrate as demonstrated by Figure 1.2. A knife, concealed in a briefcase, is exposed by the 0.2 THz radiation. Unlike X-rays, THz-waves are non-ionizing and pose a minimal risk to human tissue [7]. Figure 1.3 shows an image created from a single pixel HEB imaging device. The gun carried by the man is clearly visible through his clothing.

Astronomy is another area where HEB detectors are desired. Their sensitivity and detection efficiency over mm-wave and lower THz frequency bands make them ideal devices to investigate the Cosmic Microwave Background radiation that holds information on the origins of the universe at the time of the Big Bang [9].

The technologies which rival superconductor-based systems are typically created with semiconductors. For instance, Schottky diodes are used in terahertz (THz) imaging [4], along with hot electron bolometers and superconductor-insulator-superconductor (SIS) junctions. The diodes can be operated at room temperature, and systems capable of generating images of solid objects have been made. The benefits of superconductor-based sensors lie in the inherently low noise of the systems [9] and the small characteristic times related to detection and electron recombination. This speed, sensitivity, and low noise are requirements for passive detectors used in astronomy and terrestrial imaging devices.

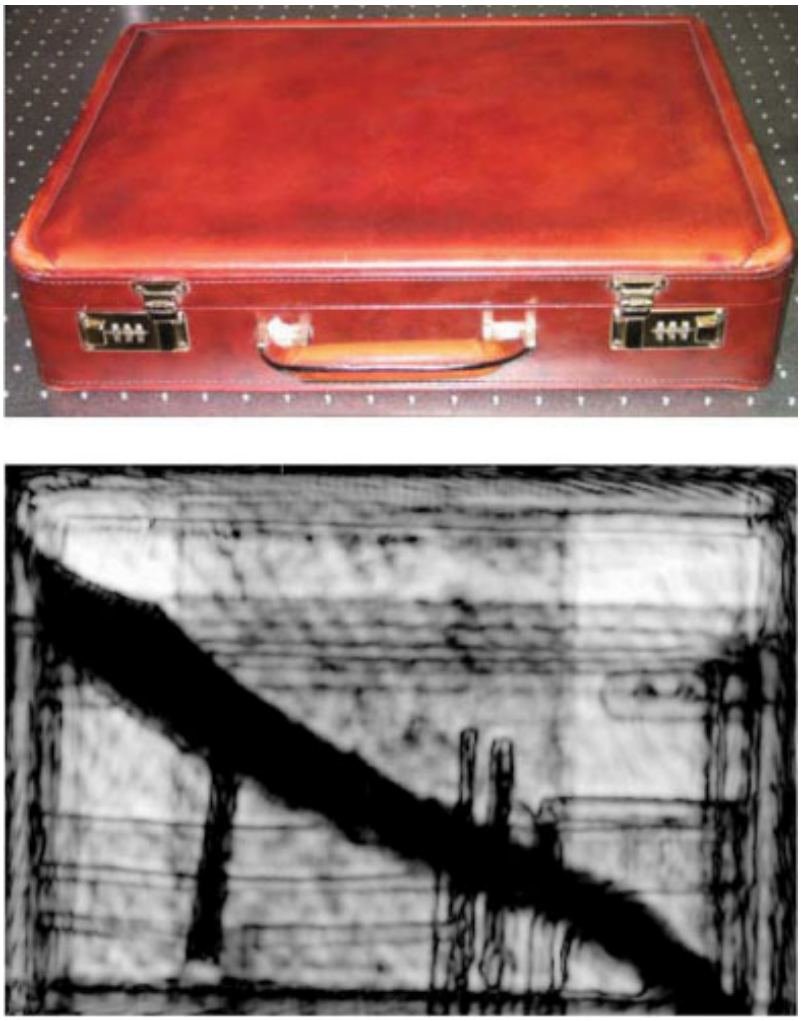

Figure 1.2: An image made of a knife, seen in the lower image, contained in a briefcase. The image was made by constructing an image based on the informations gathered by detector gathering radiation at 0.2 THz. Taken from [4].

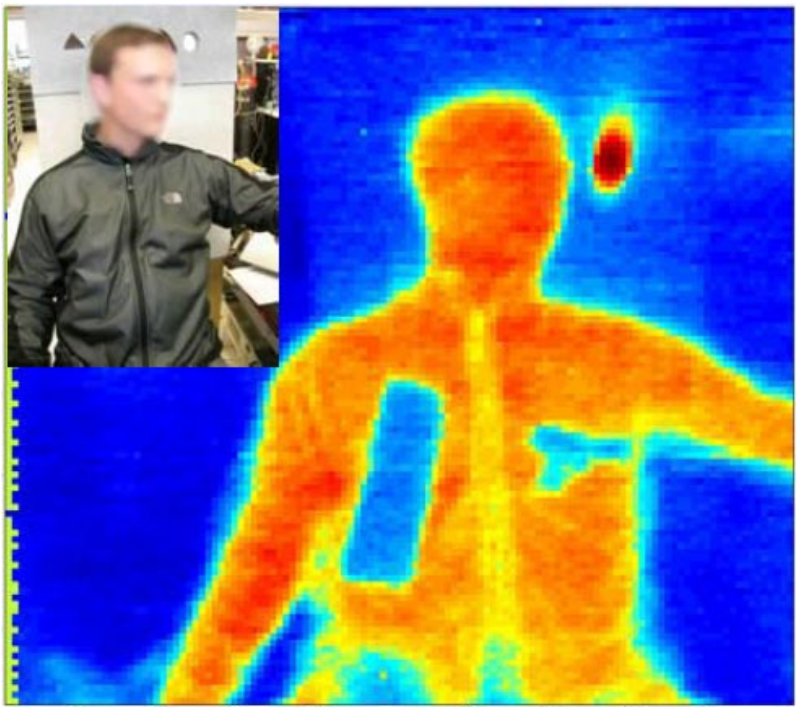

Figure 1.3: An image taken of a man (inset) carrying a gun. A single pixel HEB mixer was used to create the image [8].

1.2 Thesis outline

This thesis is structured to flow from theory to application and design to implementation of physical devices. Chapter 2 mostly deals with some theory behind superconductivity, material properties as a function of frequency, bolometers, and spectroscopy. This is followed by Chapter 3 where the design of the antennas is presented. Simulations of HEB bridges using heat balance and temperature profiles are found in Chapter 4. The simulations estimate the sensitivity of the detectors and the potential conversion efficiency if used as frequency mixing elements. A design and plan for an HEB mixer as well as HEB-based spectroscopy systems can be found in Chapter 5. The manufacturing process, including materials used in HEB fabrication, is described in Chapter 6. Results from experiments with fabricated HEB devices, and conclusions and recommendations can be found in Chapters 7 and 8.

Chapter 2

Background theory

The physics of superconductivity and of methods of designing an HEB are discussed. Relations concerning superconductors and the effects of temperature, magnetic fields, and current are important to predict the response of any device incorporating such materials. There is no general microscopic theory for all superconductor phenomena, and much work is done using macroscopic models which tend to incorporate a hybrid approach of classical and quantum mechanical solutions.

Also presented are models on the operation of hot electron bolometers that can yield information on the sensitivity to input power under operating conditions. Temperature profiles across the superconductor change due to power flow in both electrons and the crystal lattice, and these can be used to predict DC and IF voltage outputs.

Material properties in the high gigahertz (GHz) and low terahertz range (THz) are examined. The effects of low temperatures in relation to these parameters must also be taken into account for reliable and predictable simulation and experimental results.

The physical process of thermal radiation is important when understanding how a millimeter wave (mm-wave) or terahertz wave sensor might detect a signal from or through an object. This is extended with an explanation of the Fourier transform spectroscopy process and how it can be used to measure antenna and sensor performance.

2.1 Superconductivity overview

In a basic macroscopic description, superconductivity is a state in which a material conducts electricity without loss and also expels magnetic fields from within its volume. In order to describe the sensing and frequency mixing potential of a superconductor, a suitable theoretical model must be formed. A classical model, the London model, is often sufficient for macroscopic problems, akin to using Newtonian mechanics based on the scale of a problem. The phenomenon is also treated thermodynamically with the Ginzberg-Landau theory of superconductivity. An entirely quantum mechanical approach, the Bardeen-Cooper-Schrieffer (BCS) theory, accurately models low critical temperature (low-T_c) superconductivity, and can predict experimental results quite well for these materials. It yields some insight into the nature of superconductivity, but does not adequately explain the measured results from experiments using the high critical temperature (high-T_c) materials.

Normal conductors have an electron cloud that is able to freely move in the conductor's crystal lattice. This can be represented as a plane wave in the direction of current flow, possible by the wave-like nature of the electrons. In a perfect crystal, with no vibrations, the plane wave can move through the lattice without scattering, which gives rise to electrical resistance. Real crystals will have imperfections, like missing atoms and impurities, so, even at absolute zero, the best conductors will have some residual resistance. Moreover, practical application would ensure that a conductor is never at absolute zero temperature, so lattice vibrations will scatter electrons and resist flow in even a perfect crystal.

The hallmark quality of superconductors is demonstrated when such a material is cooled below a certain critical temperature temperature, T_c, (see Fig. 2.1), the resistivity is reduced to zero. Current (called a supercurrent) flows without loss, provided it remains inside a material in the superconducting state.

The Meissner effect is another unique property of superconductors. When transitioning to the superconducting state, magnetic fields are expelled from the material. This is what really sets superconductors apart from perfect conductors, since the latter implies only that $\partial \bar{B}/\partial t = 0$. Superconductivity requires that $\bar{B} = 0$ (perfect diamagnetic). This property is complicated by

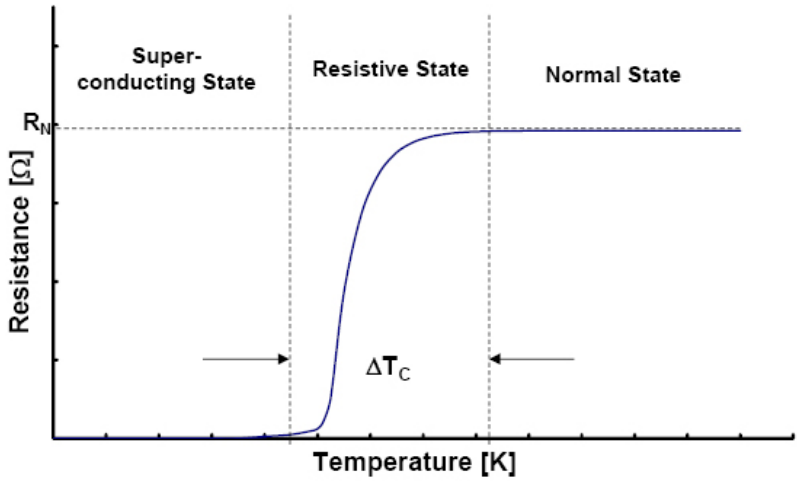

Figure 2.1: The sharp transition from the superconducting to the normal state is a sensitive mechanism for the detection of incident energy.

the fact that superconductivity can be broken by magnetic fields (B-fields) of sufficient strength, and this field is known as the critical magnetic field, B_c.

There are three major methods when measuring the critical temperature, T_c, of a material. The first is to directly measure the resistance as a function of temperature. Pure samples will transition to zero resistance quickly (millikelvin transition width), while impure samples will have broad transitions of perhaps several kelvin. Another method uses the magnetic permeability of the material to note the transition since superconductors expel magnetic fields. This is a clear transition and a non-intrusive measurement in weak fields is possible. Difficulty may arise if one material has a higher T_c than others, since this may mask the transitions at lower temperatures. It is also noted that the specific heat of a material is discontinuous at the transition temperature, and such discontinuities can be used to determine T_c.

In practical testing, it is impossible to say with certainty that the resistance of a superconductor is indeed zero since there will always be doubt as to the sensitivity of any measuring apparatus being too low to measure a non-zero value. However, theory gives the argument, and careful testing has shown no decay in supercurrent left circulating in loops of wires, sometimes for years [10].

Superconductivity varies from other resistanceless flow types (such as cath-

ode ray tube beams) because the superconducting electrons (superelectrons) along a path are all traveling at the same velocity. This happens to maintain the neutral electric charge in the material, both to balance the stationary crystal ions, and the fact that accelerating electrons create an electric field, which cannot exist in a superconductor, at DC.

Having no voltage drop across a superconducting material only holds true at DC conditions. When the supercurrent is changing, an electric field is formed and power *is* dissipated inside the material. When the frequency of a current reaches the superconducing energy gap ($E = h\nu$, where h is Planck's constant, and ν the frequency), the superelectrons will enter the normal state. For Type I superconductors, the BCS theory predicts [11] an approximate bandgap

$$\Delta_s \approx \frac{7}{2} kT_c \tag{2.1}$$

based on the T_c of the superconductor, as well as the Boltzmann constant. This gap energy is actually a function of temperature, and approaches zero as the electron temperature approaches T_c [12], as one would expect.

Superconductors are classified into two types of materials, based on how they react to an external magnetic field. Type I superconductors abruptly change to the normal conducting state once the critical magnetic field is reached. Another kind of superconductor, Type II, enter a mixed state when the critical magnetic field is reached. The Type II superconductor gradually transitions to the normal state with further increases to the magnetic field. The mixed state sees the superconductor have regions of normal conductivity and vortex flow in the superconducting regions.

2.2 London theory of superconductors

Superconductivity, as seen in working devices, can be thought of as a macroscopic representation of clearly quantum mechanical processes. As such, the principles of quantum mechanics should describe the phenomenon better than classical physics. Fritz London, in the 1940s, formulated a theory which would treat the superelectron[1] fluid in a superconductor as a macroscopic quantum

[1] Also called Cooper pairs, to note that electrons form a pair while in this state.

wave function. All superelectrons can then be described by

$$\psi = |\psi| \, e^{i\theta} \tag{2.2}$$

where θ is the real scalar phase of the wave function. The density of superelectrons per unit volume is the square of the amplitude,

$$|\psi|^2 = n_s \tag{2.3}$$

and, for weak fields, is assumed independent of the position of the superelectrons described by this wave function.

The skin effect describes how an alternating current tends to want to flow along the surface of a conductor, mostly within a distance known as the skin depth. For a perfect conductor, the skin depth is zero. The material has infinite conductivity and can respond to any electric field instantly and move as much charge as needed to cancel the field inside. Superconductors respond to this stimulus in a different manner. At DC there is a fixed penetration of the field into the superconductor, called the London penetration depth. The free electron model predicts a DC penetration at zero kelvin, λ_0, with

$$\lambda_0 = \sqrt{\frac{m_e}{2\mu_0 n_s e^2}} \tag{2.4}$$

which uses the mass and charge of the electron, m_e and e, and the permeability of free space, μ_0.

The London brothers concluded that since the case of a perfect conductor works with superconductors only when the trapped magnetic field inside is zero, Maxwell's equations should be modified to fit with the experimental results. Two equations

$$\mu_0 \lambda_0^2 \frac{\partial \bar{J}_s}{\partial t} = \bar{E} \tag{2.5}$$

and

$$\bar{B} = -\mu_0 \lambda_0^2 \bar{\nabla} \times \bar{J}_s \tag{2.6}$$

describe the observed phenomenon. Equation (2.5) describes the resistanceless flow of current in the material. The second, (2.6), describes the supercurrent, $\bar{J}_s$, canceling the magnetic field inside the material, as seen in the Meissner

effect.

Modifications are required for time-varying harmonic fields. In such fields, the London equations are

$$\mu_0 \lambda_L^2 \frac{\partial \bar{J}}{\partial t} = \bar{E} + \sigma_n \mu_0 \lambda_L^2 \frac{\partial \bar{E}}{\partial t} \tag{2.7}$$

$$-\mu_0 \lambda_L^2 \bar{\nabla} \times \bar{J} = \bar{B} + \sigma_n \mu_0 \lambda_L^2 \frac{\partial \bar{B}}{\partial t} \tag{2.8}$$

which, along with Maxwell's equations, can describe many macroscopic phenomena observed in superconductors in time-varying harmonic fields. If one combines them with Maxwell's equations, a set of four relations emerges:

$$\bar{\nabla} \times \bar{\nabla} \times \bar{E} + \frac{1}{\lambda_L^2} \bar{E} + \sigma_n \mu_0 \frac{\partial \bar{E}}{\partial t} + \epsilon \mu_0 \frac{\partial^2 \bar{E}}{\partial t^2} = 0 \tag{2.9}$$

$$\bar{\nabla} \times \bar{\nabla} \times \bar{B} + \frac{1}{\lambda_L^2} \bar{B} + \sigma_n \mu_0 \frac{\partial \bar{B}}{\partial t} + \epsilon \mu_0 \frac{\partial^2 \bar{B}}{\partial t^2} = 0 \tag{2.10}$$

$$\bar{\nabla} \times \bar{\nabla} \times \bar{J} + \frac{1}{\lambda_L^2} \bar{J} + \sigma_n \mu_0 \frac{\partial \bar{J}}{\partial t} + \epsilon \mu_0 \frac{\partial^2 \bar{J}}{\partial t^2} = 0 \tag{2.11}$$

$$\frac{1}{\lambda_L^2} \rho_e + \sigma_n \mu_0 \frac{\partial \rho_e}{\partial t} + \epsilon \mu_0 \frac{\partial^2 \rho_e}{\partial t^2} = 0 \tag{2.12}$$

An interesting result is immediately seen when (2.12) is solved with the general solution

$$\rho_e = A_1 e^{-\gamma_1 t} + A_2 e^{-\gamma_2 t} \tag{2.13}$$

where the decay constant, $\gamma_1 \approx \sigma_n / 2\epsilon$ and $\gamma_2 \approx (\sigma_n \mu_0 \lambda_L^2)^{-1}$. The slower of the two, γ_2^{-1}, will dominate the decaying of free charges. For Nb, this time works out to, typically, less than a picosecond. Therefore, a detector based on Type I superconductors, all being simple metals, has the potential to quickly relax after an excitation and is capable of detecting photons with energies in the meV range, but below the gap energy.

2.2.1 Two-fluid model in an AC field

The flow in a superconductor can be thought of in terms of a two-fluid system of electrons in both the superconducting and normal states. The idea is

a thermodynamic take on superconductivity, but, together with the London model, can predict many macroscopic phenomena observed in superconuductors. The two-fluid model assumes the current flow is made up of a mix of electrons and superelectrons, where the total number of electrons in a volume is $n = 2n_s + n_n$. Due to the transition from superconductor to normal metal with rising temperature (to T_c), the fractions of superelectrons and electrons to the total of both are represented by

$$\frac{2n_s}{n} = 1 - \left(\frac{T}{T_c}\right)^4 \tag{2.14}$$

$$\frac{n_n}{n} = \left(\frac{T}{T_c}\right)^4 \tag{2.15}$$

at DC, as found by Gorter and Casimir [13]. As one can see, the normal conductivity can be reasoned as being affected by a factor of $(T/T_c)^4$. At T_c, the factor is unity, so the conductivity will be σ_n, the normal conductivity before transition. This value will decrease with temperature as more and more electrons form Cooper pairs.

The London penetration depth also varies with temperature as a consequence of the two-fluid model. In a DC electric field, as one would expect with normal conductors, the field penetrates the material in its entirety. So, noting that this should be a transition from the London penetration depth to infinity, the relation becomes

$$\lambda_L(T) = \frac{\lambda_0}{\sqrt{1 - \left(\frac{T}{T_c}\right)^4}} \tag{2.16}$$

which clearly satisfies the conditions at $T = 0$ K and $T = T_c$.

In an AC field, (2.14) and (2.15) start to become inaccurate at predicting the ratio of superelectrons or electrons to the total number in the current. In BCS theory, energy can only be absorbed by particles in excited states (electrons called quasi-particles) unless the energy has a frequency higher than the gap frequency. If this is true, the EM field may break up the Cooper pairs, creating quasi-particles. For a low-T_c superconductor, this gap frequency can

be predicted by the relation (in angular form)

$$\omega_g = \frac{2\Delta_s}{\hbar} \tag{2.17}$$

where Δ_s is the superconducting gap energy of the material, and the temperature is at absolute zero. At non-zero temperatures, thermal excitations create quasi-particles, which causes energy to be lost, even when the frequency is below the gap frequency.

The results for the fractional number of superelecrons and electrons in (2.14) and (2.15) can be corrected by using

$$\frac{2n_s(T,\omega)}{n} = \left(1 - \left(\frac{T}{T_c}\right)^4\right) g(T,\omega) \tag{2.18}$$

for the superelectrons, and

$$\frac{n_n(T,\omega)}{n} = 1 - \left(1 - \left(\frac{T}{T_c}\right)^4\right) g(T,\omega) \tag{2.19}$$

for the number of electrons in normal current flow. The function $g(T,\omega)$ is given by

$$g(T/T_c,\omega) = 1 - \frac{1}{\sqrt{1+\Gamma(\omega_g(T)/\omega)^\eta}} \tag{2.20}$$

where the angular frequency dependent function, Γ, and the exponent, η, are material-dependent phenomenological parameters. The gap frequency also varies with temperature, and can be given by

$$\frac{\omega_g(T/T_c,\omega)}{\omega_g(0)} = \sqrt{\cos(\frac{\pi}{2}(\frac{T}{T_c})^2)} \tag{2.21}$$

which uses (2.17) to determine the frequency at absolute zero.

The current density of a material in an AC field will be given by the complex conductivity in the relation

$$\bar{J} = \bar{J}_s + \bar{J}_n = \sigma\bar{E} = (\sigma_1 + i\sigma_2)\bar{E} \tag{2.22}$$

where the σ_1 and σ_2 can be given by

$$\frac{\sigma_1}{\sigma_{DC}} = \frac{1 - \left(1 - \left(\frac{T}{T_c}\right)^4\right) g(T,\omega)}{1 + 4(\frac{\lambda_0}{\delta_0})^4} \tag{2.23}$$

and

$$\frac{\sigma_2}{\sigma_{DC}} = \frac{1 - \left(\frac{T}{T_c}\right)^4 g(T,\omega) + 4(\frac{\lambda_0}{\delta_0})^4}{\mu\omega\sigma_{DC}\lambda_0^2(1 + 4(\frac{\lambda_0}{\delta_0})^4)} = (\omega\mu_0\lambda_L^2)^{-1} \tag{2.24}$$

respectively. The parameter, δ_0 equals $(2/\mu_0\omega\sigma_{DC})^{-1/2}$. Measured values of the normal DC electrical conductivities (above T_c) are widely available for most materials, but can also be calculated from $\sigma_{DC} = n\tau_n e^2/m_e$. The total number of conduction electrons is n, the mean scattering time of electrons is τ_n, and the charge and mass of the electron are e and m_e.

The London penetration depth is also altered in a time-varying field. Including the temperature dependence of (2.16),

$$\lambda_L(T/T_c,\omega) = \frac{\lambda_0\sqrt{1 + 4(\lambda_0/\delta_0)^4}}{\sqrt{(1 - (\frac{T}{T_c})^4)g(T/T_c,\omega) + 4(\lambda_0/\delta_0)^4}} \tag{2.25}$$

with the inclusion of a frequency dependence. The extra term in the denominator ensures that the RF field only penetrates a finite distance in the normal state.

2.2.2 Coherence length

Since superconductivity depends on Cooper pairs, it is imperative to know the distance over which they can exist, on average, without losing coherence from non-local effects. This is called the coherence length, ξ_0. Empirically,

$$\xi_0 = \gamma\frac{\hbar v_F}{k_B T_c} \tag{2.26}$$

for the length independent of impurities. For superconductors described by BCS theory, γ is found to be approximately 0.18. For niobium and YBCO, this length, ξ_0, is 39 nm and 1.5 nm, respectively [14].

In an imperfect crystal (due to impurities, grain boundaries and other

effects) the effective coherence length, ξ, is altered as

$$\frac{1}{\xi} = \frac{1}{\xi_0} + \frac{1}{\alpha l_e} \tag{2.27}$$

which takes into account the mean free path of the electrons due to impurities, grain boundaries and geometric effects. The parameter α is typically assumed to be unity. The consequences of (2.27) are, for impure samples, that the effective coherence length of most superconductors can be dominated by the mean free path of the electrons. This will increase the penetration depth into the superconductor, since the length is altered as

$$\lambda = \lambda_L \sqrt{\frac{\xi_0}{\xi}} \tag{2.28}$$

with $\xi \leq \xi_0$.

2.3 Results from the Ginzburg-Landau theory of superconductivity

The Ginzburg-Landau theory of superconductivity describes the superconductive state using thermodynamic principles. The formation of Cooper pairs from electrons is then treated as a change of state.

Under an applied magnetic field, a superconductor's critical temperature will decrease. There also exists a critical magnetic field, B_C, at which the material is no longer able to conduct a supercurrent. A mathematical prediction of the relation between critical temperature and critical magnetic field is given by [15]

$$B_c = \sqrt{\frac{\mu_0 \alpha^2(T)}{\beta(T)}} \tag{2.29}$$

which, near (but below) T_c, becomes

$$B_c = T_c \sqrt{\frac{\mu_0 \alpha_0^2(T)}{\beta(T_c)}} \left(1 - \frac{T}{T_c}\right) \tag{2.30}$$

where α and β are phenomenological coefficients.

2.3.1 Thin films solutions in the Ginzberg-Landau theory

In order to better understand systems utilizing thin films of superconducting materials, it is useful to have predictive equations relating important material properties and dimensions. The following equations are applicable to films with a thickness less than its London penetration depth and effective coherence length, ξ [14].

The critical magnetic field parallel to the film surface can be estimated by

$$B_{cf} = \frac{\lambda_L \sqrt{24}}{d} B_c. \tag{2.31}$$

The critical field perpendicular to the surface of the thin film, related to the critical field of a bulk sample, B_c, is given by

$$B_{c\perp} = \sqrt{2}\kappa(d) B_c. \tag{2.32}$$

with

$$\kappa(d) = 0.715\lambda_L(0)\left(\frac{1}{l_e} + \frac{C_d}{d}\right) \tag{2.33}$$

for film of thickness, $d < \lambda_L$. The constant, C_d, is a material-dependent parameter.

Equation (2.34) is an estimation on the critical current density inside a thin film (still thinner than the penetration depth). This equation has another form using a complex order parameter representing the phase transition from the normal to superconducting state. For $J > J_c$, this order parameter is zero.

$$J_c(T) = \frac{2\sqrt{2}}{3\sqrt{3}} \frac{B_c(T)}{\mu_0 \lambda(T)} \tag{2.34}$$

The complex order parameter in a homogeneous superconductor (which can be seen as an effective wave function [14]) can be described by (2.35). Near the superconductor-normal metal transition, the square of the complex order parameter is equal to the superelectron density, n_s,

$$|\psi_0|^2 = \frac{\alpha_0}{\beta(T_c)}(T_c - T). \tag{2.35}$$

Type II superconductors undergo two phases when exposed to high magnetic fields. The first critical point, B_c, will see the material start to transition to the normal state. Magnetic field lines will penetrate the superconductor increasingly, but not destroy all the supercurrent. The second point, B_{c2}, occurs when supercondictivity is destroyed completely. For niobium, at DC, $T_c = 9.25$ K, $B_c = 0.199$ T, $B_{c2} = 0.3$ T, $\xi = 39$ nm, $\lambda = 50$ nm, $\kappa = \lambda_0/\xi_0 = 1.28$. It is found that the second critical magnetic field strength can be found with

$$B_{c2} = \kappa\sqrt{2}B_c \tag{2.36}$$

for most type II superconductors. The magnetic fields required to break superconductivity in pure films of YBCO or Nb are stronger than the Earth's magnetic field. With magnetic shielding, it is assumed that the magnetic field is small enough to be negligible in terms of the supercurrent, J_s.

2.3.2 Superconducting bridge

A thin superconducting bridge between two normal metal contacts will display modified behaviour compared to a bulk sample. If a film is too thin (generally less than 3 nm), superconductivity will be completely supressed [16]. With increasing thickness, this film of niobium will eventually transition to a thickness that will allow superconductivity. The critical temperature will be less than a bulk sample, until the niobium layer reaches even greater thickness. If the film is in contact with a metal in the normal conducting state, the superconducting properties are altered again. The critical temperature will be suppressed, and a thin layer inside the superconductor (typically on the order of nanometres or tens of nanometres) will remain a normal metal even approaching absolute zero. Since the superconductor under the normal metal contact pads does not need to be superconducting, this will not impair the operation of superconducing HEBs.

The lumped resistance of a superconducting bridge (under a DC bias) as a function of bridge temperature, T, can be shown to be [17]

$$R_{bridge}(T) = n_n(T)\Lambda_Q(T)\frac{2R_N}{L}\frac{\cosh(\frac{L}{\Lambda_Q(T)}) - 1}{\sinh(\frac{L}{\Lambda_Q(T)})}. \tag{2.37}$$

This uses the simplification

$$\Lambda_Q(T) = \sqrt{\frac{4k_BT}{\pi\Delta_s(T)}D\tau_{in}}. \tag{2.38}$$

Equation (2.37) describes the resistive transition from normal resistance before transition, R_N, to the residual resistance value after transitioning to the superconducting state. (Ideally this is zero.) Equation (2.38) describes the length over which a current inside the bridge is dissipative [17]. Δ_s is the superconducting gap energy (in the direction of current flow), k_B is the Boltzmann constant, D is the electronic diffusion constant, and τ_{in} is the inelastic scattering time of electrons at the Fermi energy.

A microbridge of niobium that borders a normal metal (such as gold) should follow (2.37) when transitioning between normal and superconducting states.

2.3.3 Andreev reflections

Andreev reflections are a scattering event (and charge transfer event) that occurs on the interface between a normal metal and a superconductor. An electron (in a normal metal), with energy less than the superconducting energy gap, Δ_s, that is incident to the boundary between a normal metal and a superconductor will cross the boundary and form a Cooper pair inside the superconductor. As a result, an electron hole is retroreflected[2] inside the normal metal along the path the electron took. This electron hole has a spin that is opposite to that of the incident electron.

2.4 Bolometers

A thin film or similar device that is cooled down close to absolute zero can be quite sensitive to external heat energy. Superconductors, when current or voltage-biased to near its state transition, are some of the most sensitive and nonlinear of these devices. Bolometers are often called 'square law' detectors since the measured change in the signal from the detectors varies with the

[2]A retroreflection is a reflection where the wave is reflected back parallel to, but opposite in direction to, the incident wave. The angle of incidence is greater than zero.

square of the incident radiation power amplitude [18]. A time constant of the thermal change to input power can be expressed as

$$\tau_{th} = \frac{C}{G} \tag{2.39}$$

where C is the heat capacity of the absorber, and G is the thermal conductance of the device to the bath temperature. To enable devices to be quick, the thermal time constants of a bolometer should be as small as possible. This can be done by lowering the total heat capacity (typically by lowering the device volume) and choosing materials to maximize the heat transfer from the device to the surroundings (typically done by careful choice of crystal lattice materials and boundaries). Should the frequency of varying incoming radiation exceed the limit defined by the thermal time constant (equation 2.39), the measured signal will not vary in unison but rather reach a higher steady-state thermal energy. If two signals produce beats, it is possible for only the intermediate frequency to oscillate the electrons and phonons [18].

The heat capacity of the bridge can be found at a specific temperature, T, and absorbing bridge volume, V, by

$$C = \gamma_{th} T V \tag{2.40}$$

with the material parameter, $\gamma_{th} = 7 \times 10^{-4}\ JK^{-2}cm^{-3}$ for niobium [19]. The lumped thermal conductance varies with the temperature of the bridge. The thermal conductance at T_c can be estimated by assuming an effective bridge resistance, R_{eff}, and the relation

$$G_0 = \frac{L_{th} T}{R_{eff}} \tag{2.41}$$

where $L_{th} = 2.5 \times 10^{-8}$ WΩK^{-2} for niobium. R_{eff} for a bridge where heat can conduct through both ends can be estimated as $R_{eff} = R_n/12$ [19]. Due to self-heating effects, the thermal conductance at the biasing point can be estimated [19] as half of the value computed by (2.41). So,

$$G = G_0/2 \tag{2.42}$$

can be used to compute the basic thermal time constant, (2.39).

2.4.1 Hot electron bolometers

Hot electron bolometers (HEBs) make use of a phenomenon where the electrons in a solid are excited in such a way as to be out of thermal equilibrium with the crystal lattice. The power entering the system excites these quasi-particles, and also due to system properties, this power cannot leave fast enough to maintain equilibrium. Typically for metals, this does not yield a readily measureable effect[3], such as a resistance change [20], especially at low signal powers. In semiconductors, charge mobility is a function of electron temperature [21], so system properties are altered with the presence of hot electrons.

Similarly in superconductors, electromagnetic radiation will excite electrons and can noticably change the state of the system. Cooper pairs can be broken if a photon's energy is greater than $2\Delta_s$, typically 2 meV [14], with one quasi-particle gaining, approximately, the photon energy, $h\nu$, and the other remaining in its current energy state [16]. The higher energy electron will subsequently break other Cooper pairs if it has the energy to do so, and will emit phonons, continuing to lose energy until the system relaxes back to thermal equilibrium.

Superconducting HEBs can be thought of as operating under two different regimes [17]. If the device is kept just below T_C and a small local oscillator power is fed across it, the bridge resistance can be described using a charge-imbalance and Andreev reflections along with the proximity effect. Devices operating under these conditions are not as sensitive as they are when the bath temperature is much lower than T_C and the device is biased with a DC source, and, so, emphasis is placed on this regime.

2.4.2 HEB cooling mechanisms

The hot electrons in the bridge allow for a signal to be measured. To enable high bandwidth devices, the bridge temperature profile must, under a pulsed input, reset back to its low temperature state as quickly as possible. This will occur by two methods.

[3]This is not necessarily true at very low temperatures.

The first is for the electrons to give their energy in the form of phonons in the bridge lattice. This energy will then escape out into the substrate. This is known as phonon-cooling.

While under a DC bias, a temperature gradient formed inside the bridge will cause the hot electrons to diffuse out into the larger conducting pads on either side. These pads should have a larger heat capacity and are often assumed to be fixed at the bath temperature. The DC and RF power create a hot spot of normal resistance on the bridge. This length is modulated by the RF source(s) across the bridge [22].

For a phonon-cooled bolometer, the thermal constant describing the heat flow from the excited electrons into the crystal lattice of the substrate, τ_{e-ph}, largely governs the bandwidth of the sensor itself. For niobium, this has been noted to be as low as 0.6 ns to 1 ns, while NbN is noted to have a τ_{e-ph} of approximately 15 ps [18]. The bandwidth of a phonon-cooled mixer (at the 3 dB point) using niobium on silicon would then be from 150 MHz to 250 MHz [18] [19]. NbN on silicon ideally has a bandwidth (3 dB point) of about 10 GHz. In practice, due to effects like electrothermal feedback, the bandwidth is less than this theoretical value.

Diffusion-cooled bolometers have the hot electrons themselves diffuse out of the sensor into a thermal bath. Therefore, it is not the electron-phonon interaction time that governs the reset time of the sensor, but the time for the elecron diffusion to take place, τ_{diff}. This mechanism comes about from the temperature gradient that is formed from the hot spot. The DC biasing unevenly changes the temperature of the bridge so it is highest in the middle and at the bath temperature at both ends. While the system under a DC bias will reach a steady state, any additional momentary perturbation will elevate the electron temperature futher and cause these hot electrons to potentially diffuse out into the contact pads.

An estimate of the time constant, τ_{diff}, can be found, for a bridge of length L, from

$$\tau_{diff} = \frac{L^2}{16D} \tag{2.43}$$

where D is the material specific diffusion constant. For niobium, about 4 K, $D \approx 1$ cm^2/s [18][19]. For a 10 μm bridge, τ_{diff} will be approximately 62.5 ns. This is much larger than τ_{e-ph}, which is typically about 1 ns, which means

that a 10 μm bridge will be dominated by phonon cooling. If the device is 1 μm, the diffusion constant will be about 625 ps and diffusion cooling will tend to dominate.

It should be noted that both phonon-cooling and diffusion-cooling often play a role in the operation of an superconducting HEB. Phonon-cooled bridges are still biased with DC power, and thus have a temperature gradient. Diffusion-cooled devices will still have electron-phonon interactions. Materials and device dimensions determine which dominates.

2.4.3 General hot electron bolometer thermal response

A bolometer is, in essence, a heat detector. The operation of these devices can be, on a macroscopic level, modeled as heat flow with in a fixed volume. A general profile of the temperature of the varying with position or time can be estimated using the heat equation (along with both Fourier's law of heat transfer and Newton's law of cooling). Following from conservation of energy, the heat energy conducted into a body and the heat generated by that body will balance with the heat conducted out and the change in stored energy within the body [23].

Newton's law of cooling states that the rate of change of T, the temperature of a hot body, is proportional to the difference in temperature of the body and its surroundings, T_b. For a one dimensional system of decreasing temperature this is

$$\frac{dT}{dt} = -k(T - T_b) \tag{2.44}$$

and the thermal conductivity, k.

In the case of a general HEB, the electrons and phonons in the bridge will exchange energy between themselves and the surroundings. Additionally, DC biasing and any RF source will further perturb the system and add more energy to the electrons. If it is assumed that the surroundings (the substrate and other nearby metal layers) are always at a lower temperature than the bridge and that the RF signal power is dissipated evenly across the bridge[4], (2.45) and (2.46) can be used to estimate the temperature of the electrons and

[4]This is similar to a lumped model assumption, thus the wavelength of any signal should be appropriately longer than the bridge for this assumption to be accurate.

phonons in a small volume.

$$\frac{d}{dx}k_e\frac{dT_e}{dx} + P_{DC} + P_{RF} + P_{p-e} - P_{e-p} - P_{diff} = 0 \tag{2.45}$$

$$\frac{d}{dx}k_p\frac{dT_p}{dx} + P_{e-p} - P_{p-e} - P_{p-s} = 0 \tag{2.46}$$

The factors k_e and k_p are the thermal conductivity of electrons and phonons. P_{e-p} is the power from electrons given in the form of phonons in the lattice and P_{p-e} is the reverse. P_{p-e} is usually much smaller than the reverse power flow in this scenario [18] [9]. P_{p-s} is the power flowing from the phonons in the lattice of the bolometer to phonons in the substrate. P_{diff} is the term representing the outflow and inflow of power due to diffusing quasi-particles. The terms P_{DC} and P_{RF} are the DC and RF (often a local oscillator in calculations) power input into the bridge. In this model, as in [22], the RF power is assumed to be absorbed evenly along the length of the bridge. This distributed assumption is better validated while the wavelength of the highest frequency is much longer than the length of the superconducting bridge. A visualization of a small volume of a superconducting bridge can be seen in Fig. 2.2.

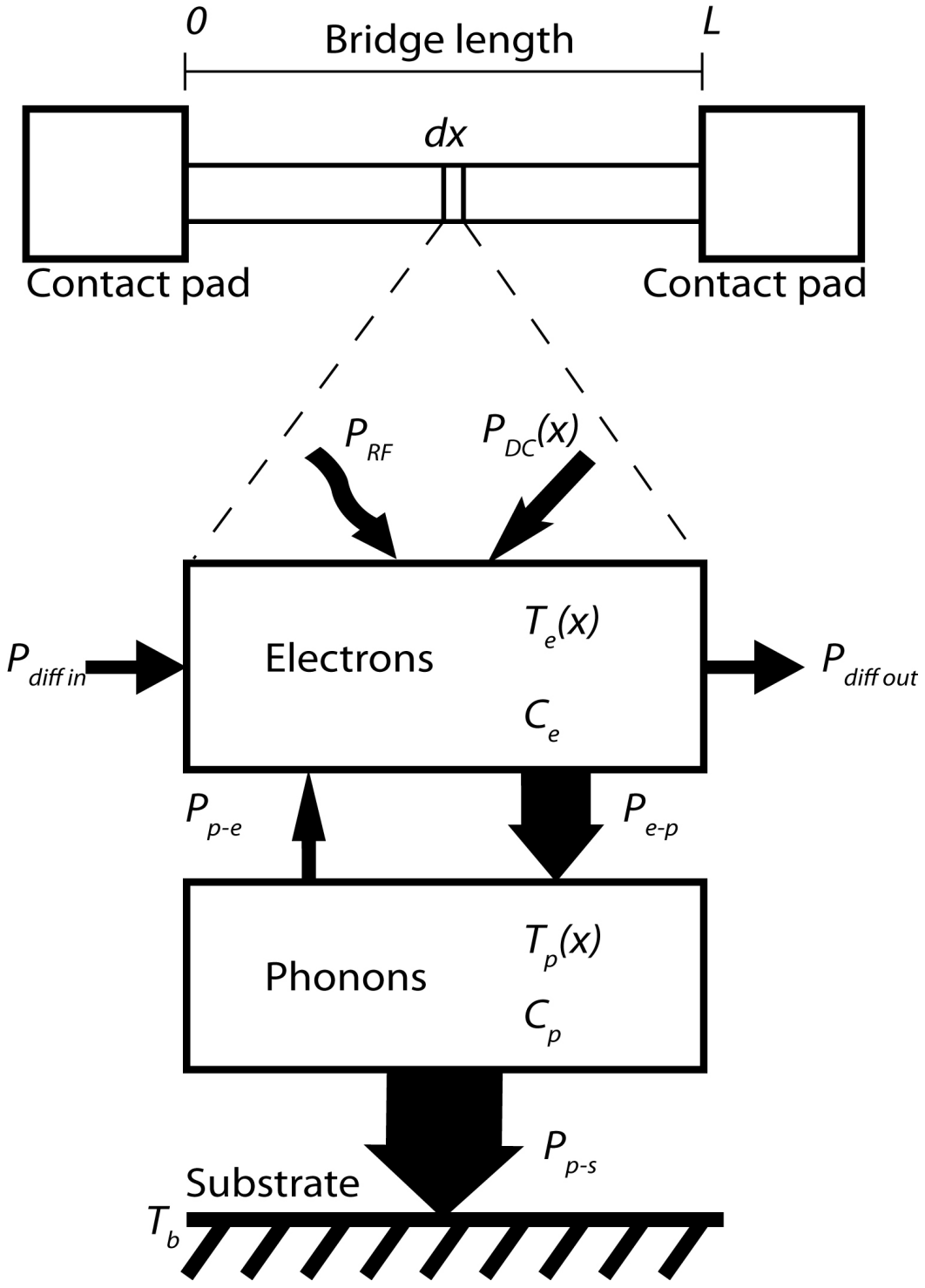

Figure 2.2: A heat balance diagram for a small slice of a superconducting bridge. Hot electrons exchange energy with phonons in the metal lattice. Similarly, these phonons release this energy to the surrounding substrate. Arrows pointing into a block indicate that power is given to the block, raising its temperature. Arrows pointing out of a block indicate power leaving a block.

2.4.4 Phonon-cooled hot electron bolometer thermal response

If one assumes that the electrons lose energy to phonons much faster than they diffuse out of the bridge (τ_{e-ph} is less than τ_{diff}), then the coupled (2.45) and (2.46) can be simplified to

$$\frac{d}{dx}k_e\frac{dT_e}{dx} + P_{DC} + P_{RF} - P_{e-p} = 0 \tag{2.47}$$

$$\frac{d}{dx}k_p\frac{dT_p}{dx} + P_{e-p} - P_{p-s} = 0 \tag{2.48}$$

The term for electron diffusion is neglected. In practical application, the term P_{p-e} is also neglected due to the long time constant for this interaction relative to the phonon energy escaping to the substrate. The DC power absorbed per unit volume is $P_{DC} = J^2\rho$, where J is the DC current density and ρ is the position dependent resistivity of the film.

The hotspot model [22] [17] adds an additional assumption where no DC power is absorbed in the bridge until the temperature of the quasi-particles, T_e is greater than the critical temperature of the superconductor.

The voltage across the bridge is expressed by the function

$$V = J\int_0^L \rho(x, T_e)dx \tag{2.49}$$

where the voltage should be across a portion of the bridge where $T_e > T_c$.

2.4.5 Diffusion-cooled hot electron bolometer thermal response

The opposing case is where the bridge is short enough to allow hot electrons to diffuse out of the bridge before they pass the heat to the crystal lattice. The temperature of the electrons can be given the differential equation

$$\frac{d}{dx}k_e\frac{dT_e}{dx} + P_{DC} + P_{RF} - P_{diff} = 0. \tag{2.50}$$

Again, the voltage can be found from (2.49). The voltage sensitivity of a

bridge to radiation is an important parameter to maximize. This is expressed by

$$S = J\rho\frac{dL_h}{dP} = I\frac{dR}{dP} \tag{2.51}$$

where dL_h/dP is the rate of change of the length of the bridge where $T_e > T_c$, with a change in input power. Maximizing the sensitivity can show the optimal biasing point for the best response to RF power. The power conversion efficiency is a maximum when the line impedance, Z_L, is equal to the differential bolometer resistance, $Z_B = dV/dI$. This efficiency can be found from

$$\eta_B = \frac{2S^2 P_{RF} Z_L}{Z_L + Z_B}. \tag{2.52}$$

The sensitivity of the detector can also be expressed in terms of the resistance changing with temperature [19]. For a bias current, I, the voltage responsivity is

$$S = \frac{I\frac{dR}{dT}}{G\sqrt{1+\omega^2\tau_{th}^2}} = \frac{S_0}{\sqrt{1+\omega^2\tau_{th}^2}} \tag{2.53}$$

for both the DC and AC components. The time constant, τ_{th}, is found from whichever thermal response mechanism dominates (diffusion or phonon-cooling) and G is from (2.42). The frequency of oscillation for the voltage, as will be seen in the next section, will be the intermediate frequency if a local oscillator is used to down mix the signal of interest. If Fourier transform spectroscopy is used, only the DC component of (2.53), S_0, is needed for analysis.

2.5 Frequency mixing

A frequency mixer is a nonlinear device that takes two input signals (typically at different frequencies) and outputs a signal at several different frequencies. As an example, for two sinusoidal signals, $V_1 = A\sin(\omega_1 t + \phi_1)$ and $V_2 = B\sin(\omega_2 t + \phi_2)$, that are passed through a device whose operation is to multiply the two signals, the output would then contain terms of the frequencies ω_1, ω_2, $(\omega_1 + \omega_2)$, and $|\omega_1 - \omega_2|$. The final term is the one most often of interest, as the two signals mixed together can produce a term of a sigificantly lower frequency. Even two signals that cannot be tracked directly, for instance, by an

oscilloscope, can be analysed indirectly by this intermediate frequency signal.

2.5.1 Superconductor-Insulator-Superconductor Mixers

Superconductor-insulator-superconductor junction detectors (hereafter called SIS mixers) use the nonlinearities of the Josephson effect [10] to mix two signal frequencies together. Photons interact with the electrons in the junction and allow them to tunnel through the insulating barrier [24]. Antennas can be coupled with the niobium junctions, allowing detection of signals limited by

$$F_{gap} = 2\Delta_s/h \tag{2.54}$$

where Δ_s is the superconducting gap energy and h is Planck's constant. This sets a physical upper frequency limit, based on the superconductor used in the junction, which must be considered before any detector is designed. For niobium-based SIS junctions, the upper frequency threshold is approximately 1.4 THz. Frequencies greater than those calculated by (2.54) will break the Cooper pairs inside a junction and lead to signal attenuation at the desired intermediate frequency.

Continued interest in SIS junctions is maintained by their most impressive quality: the sensitivity of SIS systems is quantum limited [9], making them currently the most sensitive terahertz detector design below the gap frequency from (2.17). Fabrication of junctions based on high temperature superconductor (HTS) materials may increase use of SIS mixers due to many having higher superconducting gap energies than niobium [9].

2.5.2 Hot-electron Bolometer Mixers

The term 'hot electron' comes from a decoupling (not necessarily complete) of the electron and phonon temperatures. In normal conductive materials, this phenomenon happens a temperatures below 4.2 K [18]. For superconducting materials, this distribution happens when quasi-particles are created by incoming radiation and can happen below the materials critical temperature.

Hot-electron bolometers (HEBs) operate in a similar weak link manner as

do nanowire photon detectors. The difference is that meander lines are typically used to count photons by the voltage pulses they create, while HEBs use the nonlinear resistance of materials while transitioning between the normal and superconducting state. Accordingly, the output is a frequency spectrum instead of pulses signifying photon impingement. The electron recombination physics described for photon detectors apply to HEBs too.

Hot-electron bolometers are used currently in astronomy to detect faint high frequency astronomical signals, or in frequency bands undetectable by previous technology. In theory, any two wavelengths can be heterodyned by an HEB mixer, provided the correct dimensions and system qualities (such as signal-to-noise ratio) are satisfied [9]. A mixed intermediate frequency can then be amplified and measured, with the frequency spectrum being of prime importance.

The data gathered from HEBs can be used to generate images based on material density or even chemical composition [4]. If a frequency spectrum is analyzed, absorption lines can be indicators of certain molecules absorbing radiation. In the THz spectrum, there are many such absorption lines, including many explosives. Thus objects can be identified by density and material composition. This can be done using passive radiation or by actively scanning an object with radiation either at a constant frequency or sweeping through some frequency band.

The physics of the hot electron bolometer is similar to single photon detectors in that the transition from superconductivity to normal conductivity is used to observe the phenomenon of interest. The difference is that photon detection is interested in the generation of pulses (a sign of a photon collision event) whereas hot electron bolometers use the non-linear change of resistance that occurs during the transition between normal and superconducting states [9]. This can be seen in Fig. 2.3 when looking at the bridge region. This non-linear transition allows the mixing of the source signal and local oscillator. In the case where the source and local oscillator are driving the bolometer at frequencies in the THz regime, often only the difference[5] of the two frequencies can be measured or is present at all[6]. All the required information is

[5]Source frequency minus local oscillator frequency.

[6]The driving frequencies can be so high that the electron vibrations cannot keep up [9], effectively filtering the system.

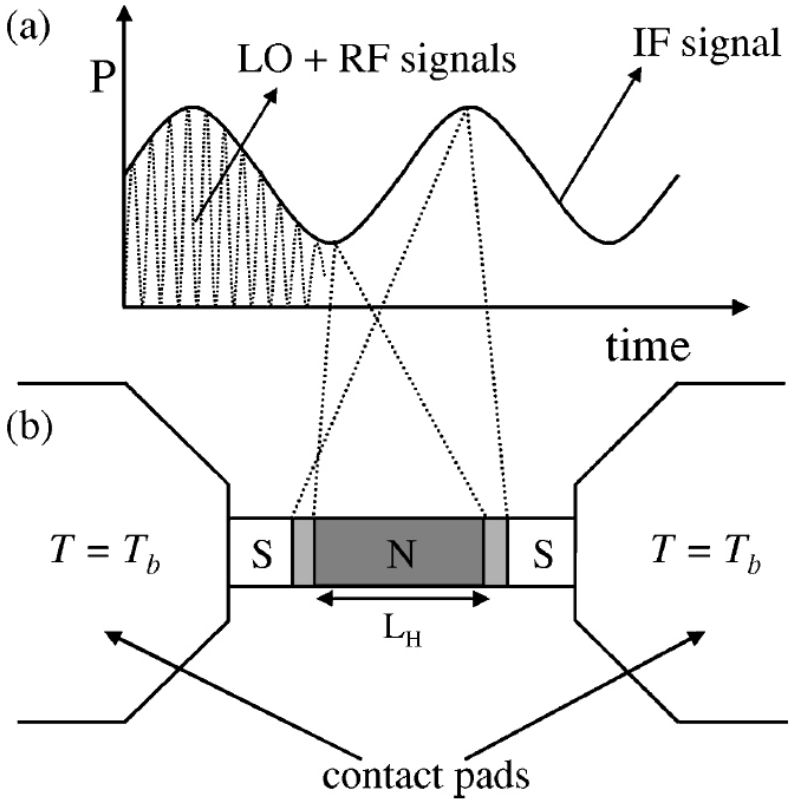

Figure 2.3: The image in (a) shows how the power from two signals can be mixed by the action of nonlinear resistance of the bridge in (b). One model (from [22]) has the area of bridge that is normal metal (N) oscillating at the intermediate frequency. The section labeled S remains in the superconducting state.

contained in the intermediate frequency, provided there is a spectrally stable local oscillator at a frequency known to be close to the source frequency.

Hot electron bolometers can be coupled with narrow band (Fig. 2.4) or broadband antennas [4], like the equiangular spiral antenna, seen in Fig. 2.5. The application dictates the required bandwidth while the source dictates the optimal polarization of the antenna. Linearly polarized, narrow band antennas are used most often for imaging, when transmission of a single-frequency signal through an object is all that is needed to form an image. Circularly polarized, broadband antennas are used when the source is polarized in a random or unknown manner and the spectral absorption of a wide frequency band is of interest.

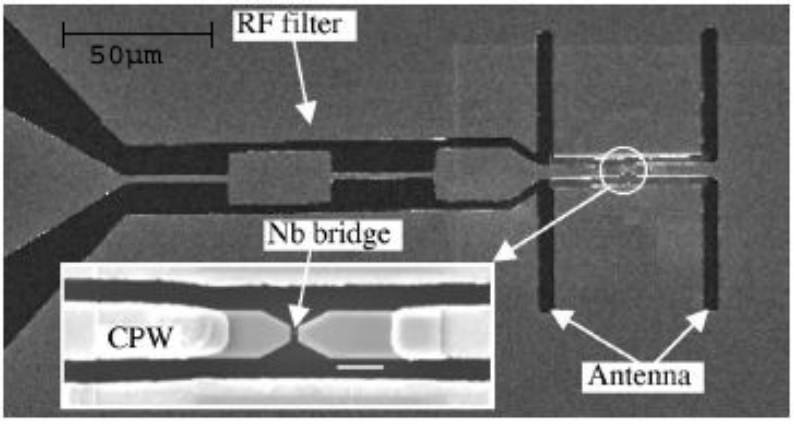

Figure 2.4: A twin-slot antenna. The inset shows the superconducting bridge in greater detail. Photo from [25].

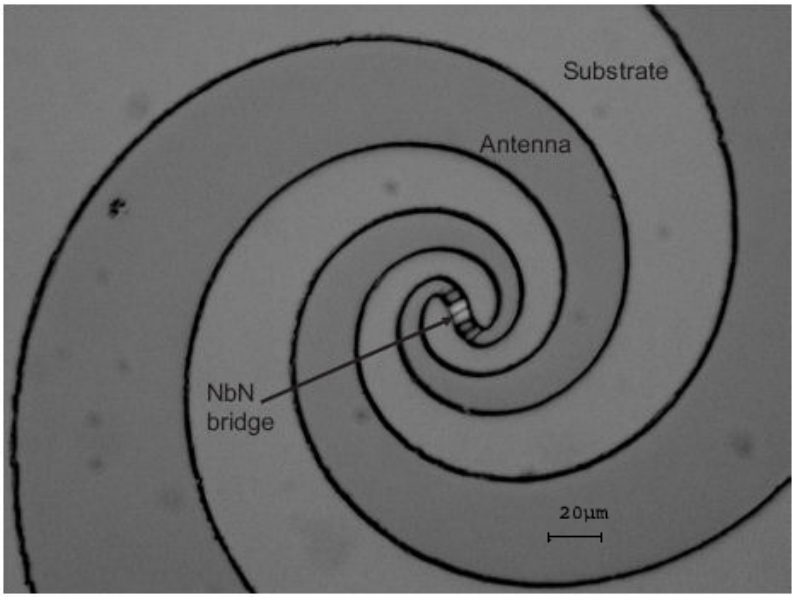

Figure 2.5: An equiangular spiral antenna. The superconducting bridge connects the two antenna arms. Photo from [9].

HEBs are currently being made in arrays for both astronomy and astrophysics research and security imaging [26]. Since most of the energy radiated in the universe is theorized to be in the THz regime[7], further development will help us learn more about the universe.

2.5.3 Frequency mixing efficiency

For two signals of frequencies ω_{LO} and ω_S, the voltage across the bridge can be represented as $V(t) = V_{LO}\cos(\omega_{LO}t) + V_S\cos(\omega_S t)$. The instantaneous power dissipated will be $P(t) = (V(t))^2/R_n$ [19]. Because the higher frequency terms of $2\omega_{LO}$ and $2\omega_S$ will average to zero [18][19], the instantaneous power will become

$$P(t) = P_{LO} + P_S + 2\sqrt{P_{LO}P_S}\cos(\omega_{IF}t) \tag{2.55}$$

containing the DC terms $P_{LO} = V_{LO}^2/(2R_n)$ and $P_S = V_S^2/(2R_n)$ and a term oscillating at $\omega_{IF} = |\omega_{LO} - \omega_S|$. Using (2.53), the intermediate frequency voltage will be

$$V_{IF}(t) = S2\sqrt{P_{LO}P_S}\cos(\omega_{IF}t) \tag{2.56}$$

which will have a DC portion given by $< V_{IF} >= S_0 2\sqrt{P_{LO}P_S}$. Assuming a matched load, the mixer conversion efficiency, η_m, can be seen from $< P_{IF} >= P_S/8$ [19], or $\eta_m = 1/8$.

2.6 Material parameters

In order to design antennas that have theoretical performances that closely follow experimental results, proper material parameters need to be used. Parameters such as permittivity vary depending on the frequency of the wave passing through it (dispersive). Some, such as the conductivity, strongly vary with temperature. This section discusses concerns raised with these parameters, their effects on these devices, and some methods of finding values appropriate for the operating conditions.

[7]The Cosmic Microwave Background [27].

2.6.1 Complex permittivity

The permittivity of a material changes with the frequency of the electric field applied to it. Complex permittivity, $\epsilon = \epsilon_1 + i\epsilon_2$ measures the resistance and loss encountered when an electric field is formed in some medium. Figure 2.6 shows how an unknown material might change with frequency. Most materials do not show all the mechanisms displayed in the figure [28], however, since the resonances are based on ionic, atomic, and electronic resonances, the trends are similar between materials.

The loss tangent, another measure used to specify the dielectric loss in a material [29], is expressed as

$$\tan\delta = \frac{\epsilon_2}{\epsilon_1}. \tag{2.57}$$

If there are charge carriers in the medium,

$$\tan\delta = \frac{\epsilon_2}{\epsilon_1} + \frac{\sigma}{\omega\epsilon_1}. \tag{2.58}$$

For silicon and magnesium oxide[8] below 10 K, both act as insulators as any charge carriers have frozen out of the conduction band [30], hence the loss tangent is lower. As seen in [31], the real part of the permittivity can be approximated as constant if the frequency band is narrow enough. This is taken as $\epsilon_1 = 9.8$ for magnesium oxide and $\epsilon_1 = 11.9$ for silicon, at 60 GHz. This is assumed constant through to 1 THz, illustrated by MgO, which has $\epsilon_1 = 10$ at 2.5 THz [32]. The loss tangent increases with frequency (from the low GHz to low THz) and decreases with temperature for both silicon and magnesium oxide. About 60 GHz, $\tan\delta$ was taken as 6×10^{-6} and 7×10^{-6} for intrinsic Si [33] and MgO [32] at 4 K, respectively. About 400 GHz, $\tan\delta$ was taken as 2×10^{-4} and 6×10^{-3} for intrinsic Si [31] and MgO [34] at 4 K, respectively. All values are for substrates with a (100) crystal orientation.

If the real or imaginary term of the complex permittivity function is known at all frequencies (or for a large enough portion from DC to a very high frequency), the other scalar function can be calculated using adapted Kramers-Kronig relations [28]. Equations (2.59) and (2.60) can be used, because causal

[8]These two materials were used as substrates for the HEB devices manufactured for this thesis.

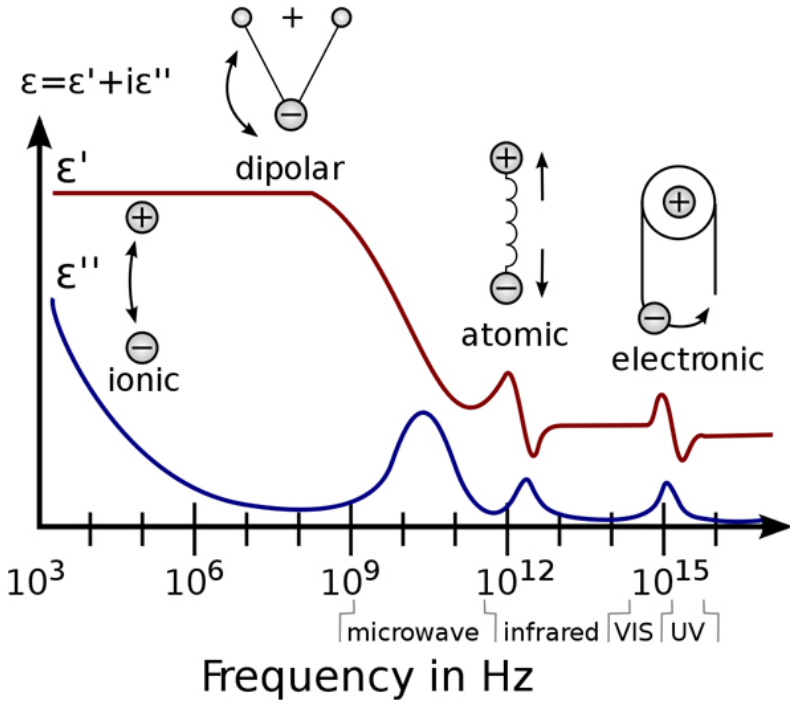

Figure 2.6: Permittivity changes with frequency. The imaginary term can be seen increasing as the electromagnetic waves resonate with various physical structures as the wavelength changes (and, hence, energy is lost to the material). Reproduced from [35].

response functions of physical systems are inherently analytic. The real (ϵ_{r1}) and imaginary (ϵ_{r2}) terms can thus be expressed as

$$\epsilon_{r1} = 1 + \frac{2}{\pi}\int_0^\infty \frac{\omega'\epsilon_{r2}(\omega')}{(\omega')^2 - \omega^2}d\omega' \tag{2.59}$$

and

$$\epsilon_{r2} = \frac{2\omega}{\pi}\int_0^\infty \frac{1 - \epsilon'_r(\omega')}{(\omega')^2 - \omega^2}d\omega'. \tag{2.60}$$

2.6.2 Admittivity

The conductivity of a metal will change with frequency, slowly decreasing with increasing frequency (at least until the 3.5 THz range [36]). The admittivity[9], $\sigma_a(\omega) = \sigma_c + i\sigma_s$, under the same range stated above, steadily gains an imag-

[9]Admittivity is also known as complex conductivity.

inary susceptivity term, σ_s. The real conductivity of gold[10] remains largely constant over this span, lowering to about 0.96 (fractionally) of its DC value at 2.5 THz [36]. Admittivity varying with frequency can be approximated by the Drude-Smith model,

$$\sigma_a(\omega) = \frac{\epsilon_0 \omega_p^2 \tau_{scatter}}{1 - i\omega\tau_{scatter}} \left[1 + \sum_j \frac{c_j}{(1 - i\omega\tau_{scatter})^j} \right] \tag{2.61}$$

The carrier scattering time is $\tau_{scatter}$ (which is 18 fs for gold thicker than 8 nm [36]), ω_p is the plasma frequency of the metal (2080 THz for gold thicker than 20 nm [36]), and c_j is the fraction of initial electron velocity after the jth collision. In most practical applications, $j = 1$, and $c_1 = 0$ for gold films of 10 nm or thicker[11]. Simplifying yields the following, which approximates the admittivity well to 2.75 THz [36].

$$\sigma_a(\omega) = \frac{\epsilon_0 \omega_p^2 \tau_{scatter}}{1 - i\omega\tau_{scatter}} \tag{2.62}$$

2.6.3 Skin depth and temperature

The conductive losses in a normal conductor will increase with increasing frequency, due to the skin effect. The alternating current will be confined to a thinner and thinner layer on the surface of a conductor [37]. An approximation of this depth is given by

$$\delta = \sqrt{\frac{2}{\omega \sigma_c \mu}}. \tag{2.63}$$

For gold at room temperature, $\sigma_c = 4.1 \times 10^7$ S/m [38] and $\mu \approx \mu_0 = 4\pi \times 10^{-7}$, the skin depth will be about 320 nm at 60 GHz and 125 nm at 400 GHz. At 10 K, the conductivity of gold is $\sigma = 4.4 \times 10^9$ S/m [39] which decreases the skin depth of gold to about 30 nm and 12 nm at 60 GHz and 400 GHz, respectively. Since an elecromagnetic plane wave will attenuate to about 0.368 of the total at one skin depth, two or more skin depths are advisable to help minimize conductive losses in normal metals.

[10] Gold is the preferred normal metal used to define the physical antennas, filters, and waveguides on the crystal substrates.

[11] For thinner films, gold acts more and more like an insulator, and a transition to $c_1 = -1$ happens. This represents backscattering of the electrons.

2.7 Thermal radiation

Thermal radiation is the elecromagnetic radiation emitted by all matter. Matter will radiate at many frequencies, and this distribution will depend on an object's temperature[40]. The blackbody curve, called Planck's law, was described by Max Planck and is given by

$$I_{th}(\nu, T) = \frac{2h\nu^3}{c^2} \frac{1}{e^{\frac{h\nu}{kT}} - 1}. \tag{2.64}$$

This is the spectral radiance curve of a blackbody radiator, and describes the emitted power per unit area of the heated blackbody's surface, per unit solid angle, per unit frequency [41]. It is a function of the frequency of the radiation, ν, and the temperature of the emitting object, T. The constants are the Boltzmann constant, k, the speed of light, c, and Planck's constant, h. Planck used h and the idea of quantized energy, $h\nu$, just as a mathematical device to fit a curve to measured data, initially unaware that this would begin the revolutionary field of quantum physics.

A real body cannot be as efficient as a blackbody at absorbing and emitting EM radiation. The emissivity of an object, ϵ_m, relates how close an object is to a blackbody, which has $\epsilon_m = 1$. Silicon carbide has an emissivity of $\epsilon_m = 0.96$.

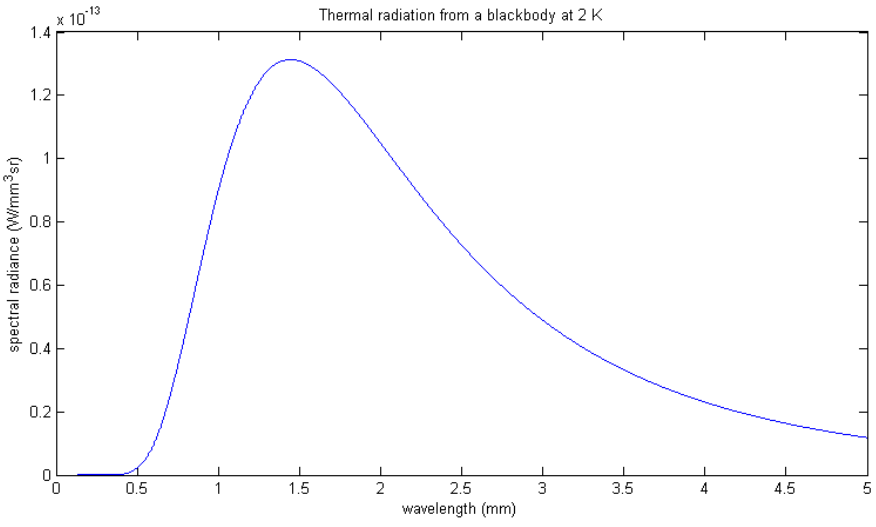

Figure 2.7: Blackbody radiation from a body with a temperature of 2K.

The distribution of spectral radiance as a function of wavelength can be seen in Fig. 2.7. The curve shows a steep drop as energy (or, frequency) increases from the peak. A more gradual decrease in spectral radiance output is seen from longer wavelengths. At 2 K, the radiation peaks at a wavelength of about 1.5 mm. This corresponds, approximately, to a frequency of 200 GHz. The total output of radiation can be seen to increase exponentially with increasing temperature. Fig. 2.8 shows the spectral intensity curve at 600 K, 900 K, and 1100 K. The increase in radiation output is consistently higher at all frequencies, with higher temperatures.

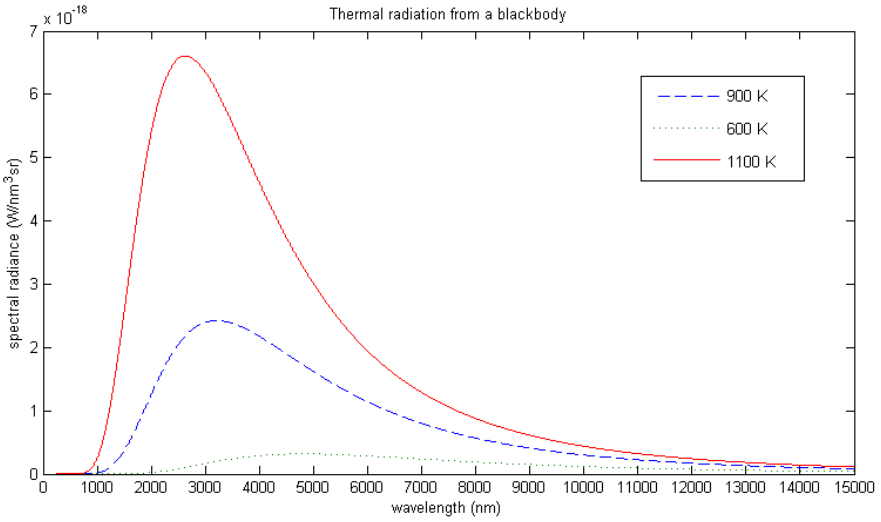

Figure 2.8: Thermal radiation from a blackbody at 600 K, 900 K, and 1100 K. The radiation output increases exponentially as temperature increases.

2.7.1 Fourier transform spectroscopy

The experimental system response to radiation at the frequencies of interest must be measured by either mixing the detected signal down with a local oscillator, or by self-interference and Fourier transform spectroscopy [42]. The latter works by splitting a coherent beam into two and introducing a path length difference, l, along one path. The beams are combined back into one and interfere constructively or destructively, depending on the value of l. A schematic of a Michelson interferometer is seen in Figure 2.9. From the Nyquist

Criterion, the sampling interval must be at least twice the highest wavenumber. The retardation must move no more than

$$\Delta l = (2\tilde{\nu}_{max})^{-1} \tag{2.65}$$

where the highest wavenumber to be measured is represented by $\tilde{\nu}_{max}$.

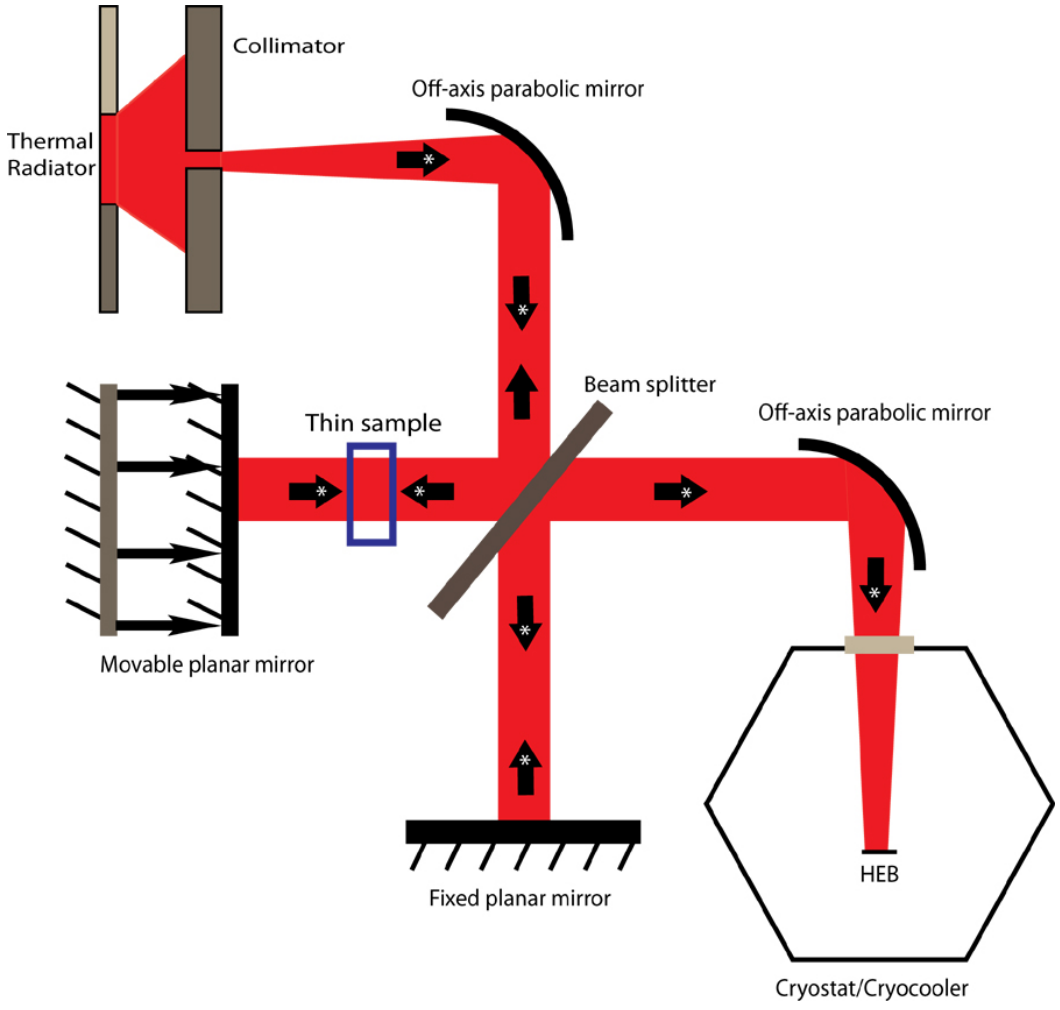

Figure 2.9: Schematic diagram of a Michelson interferometer. The arrows indicate that thermal radiation is traveling in that direction. The asterixes denote radiation along a path leading to the sensor. If a sample is placed along the beam path, it can be placed anywhere (preferably close to the sensor to minimize interference), though a sample is not needed for interferometer operation.

The thermal source is partially collimated by a metallic Jacquinot stop that has an aperture size and positioning such that the half-angle of the beam passing through does not exceed

$$\alpha = \sqrt{\Delta\tilde{\nu}/\tilde{\nu}_{max}}. \tag{2.66}$$

The wavenumber resolution is given by $\Delta\tilde{\nu}$.

Wavenumber, $\tilde{\nu}$, is converted to frequency, ν, simply by

$$\nu = c\tilde{\nu}, \tag{2.67}$$

with c the speed of light in the medium of transport, and $\tilde{\nu} = \lambda^{-1}$. The Jacquinot stop in relation to the thermal radiation source is seen in Figure 2.10. The distance between the thermal radiation source and the stop is d. The thermal radiator will have a maximum dimension in which the radiation originates (heating length, in the case of a rod) which is x_h. The radius of the Jacquinot stop, r, can then be found with the maximum half-angle, α, by

$$r = d\tan(\alpha) - \frac{x_h}{2} \tag{2.68}$$

So, for a sensor operating at a highest frequency of 410 GHz, an interferometer might range to 450 GHz. This would mean $\tilde{\nu}_{max} \approx 15$ cm^{-1}. If a resolution of 2 GHz is adequate, $\Delta\tilde{\nu} \approx 0.07$ cm^{-1}. The angle, as determined by (2.66), will be 0.068 radians. If the thermal source is a silicon carbide rod[12] with a heating length of 10 cm, and the distance between the rod and the Jacquinot stop is 1 m, the aperture radius will be approximately 1.8 cm.

As an example, using the same silicon carbide rod above, with a radius of 0.5 cm, and integrating (2.64) between 380 GHz to 440 GHz, the amount of radiation power passing through the area of a circular aperture, of radius 1.8 cm, 1 m away will be on the order of 100 nW. With a reflective backing behind the thermal radiation source, the power output will be larger than this 100 nW estimate.

For a beam with equal intensities at all frequencies, the path difference, l, translates into a small time delay which, when the two beams are recom-

[12]SiC was the thermal radiation source used in this thesis.

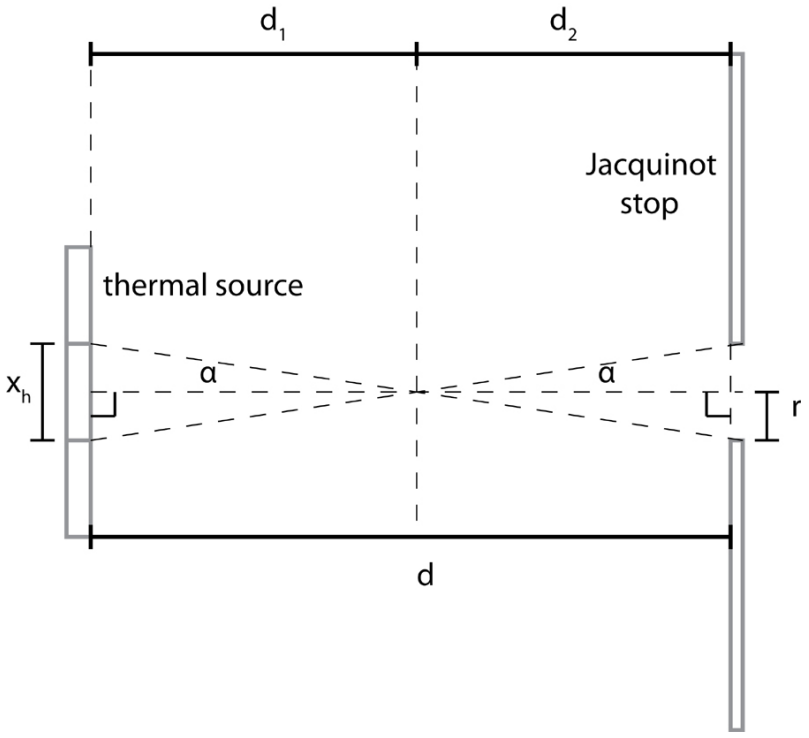

Figure 2.10: The radius of a Jacquinot stop in relation to the position of a thermal radiation source.

bined, will cause complete destructive interference for all $l \neq 0$. A detector placed after beam recombination will show a delta function centred at $l = 0$, which transforms to a constant non-zero value in the wavenumber domain, as expected. For this measurement to take place, the moveable mirror must travel an infinite distance in order to resolve to DC. For more narrow bands of interest, the mirror need only move through one wavelength of the lowest frequency [43], or $(\Delta\tilde{\nu})^{-1}$.

The intensity at the detector, for retardation (or path difference), l, is given by

$$I'(l) = \frac{I(\tilde{\nu})}{2}\left(1 + \cos(2\pi\tilde{\nu}l)\right) \tag{2.69}$$

where $I(\tilde{\nu})$ is the total possible intensity emitted at wavenumber, $\tilde{\nu}$, that can be received by the detector. As one would expect, the intensity at a specific wavenumber, $\tilde{\nu}_0$ (or λ^{-1}), would be at a maximum when the retardation is equal to $n\lambda_0$. Equation (2.69) is composed of two terms, one of which is constant in space, $I(\tilde{\nu})/2$. The second term yields the information on how the

signal interferes with itself (constructively and destructively) over a varying path difference.

The intensity read at the detector can be converted to the intensity as a function of wavenumber by Fourier transforming $I'(l)$.

$I(\tilde{\nu})$ is affected by the system[13] before measurement, so care must be taken to chose non-dispersive mirrors, windows and beamsplitters. If this quality can be assumed, the actual frequency response seen in measurement will actually be

$$M(\tilde{\nu}) = \epsilon_{sys} S(\tilde{\nu}) F_{sys}(\tilde{\nu}) I(\tilde{\nu}) \tag{2.70}$$

where ϵ_{sys} is the fraction of the beam remaining after passing through the system, $F_{sys}(\tilde{\nu})$ is the attenuation of the signal in the atmosphere[14], and $S(\tilde{\nu})$ is the wavenumber response of the sensor and system electronics. $S(\tilde{\nu})$ can be compared with the expected antenna response to determine the accuracy of the design and simulations. The signal measured at a given retardation becomes

$$M'(l) = \frac{M(\tilde{\nu})}{2} \left(1 + \cos 2\pi\tilde{\nu}l\right). \tag{2.71}$$

2.7.2 Detector antenna response to thermal radiation

The power received by a detector due to the thermal radiation delivered to the receiving antennas can be estimated using the Friis equation. The transmitted power will be represented by a thermal radiator. Assuming no multipath effects, the power received by the detector antenna, at one wavelength, will be

$$P_r = (1 - |\Gamma|^2)\eta_{ant} D_{ant} \frac{\lambda^2}{4\pi} I(l) A_{sys} P_{th} \left|\bar{p}_{th} \cdot \bar{p}_{ant}\right| \tag{2.72}$$

which takes into account the polarization of the antenna and thermal radiation source. For the case of a linearly polarized antenna for the detector, it is assumed $|\bar{p}_{th} \cdot \bar{p}_{ant}| = 0.5$ since a thermal radiation source will typically emit in a random polarization. It can be thought of similarly to circular polarization, and, due to the non-preferential circular distribution, two orthogonal linearly polarized perfect antennas should receive all of the radiation. Hence one perfect

[13]For instance, the beam intensity can be attenuated in air, or potentially scattered in a random direction from a poor mirror.

[14]One could also include a sample mass for absorption peak identification.

antenna will receive half of the radiation at this one wavelength. I_k in (2.72) is not in terms of wavenumber, but wavelength at a given retardation. Similarly, the other factors can be expressed in terms of wavenumber.

2.7.3 Detector response by Fourier transform spectroscopy

Once the mirror has been moved through one full distance equal to the longest wavelength of interest[15], this spatial response interferogram can be converted to a frequency response by performing a Fourier transformation on (2.72). What is likely to be measured is the voltage response to the input radiation.

The Fourier transform of (2.71) will give the wavenumber response distribution of the entire spectronomer, given by

$$M(\tilde{\nu}) = 2\int_{-\infty}^{\infty}(M'(l) - \frac{M'(0)}{2})\cos(2\pi\tilde{\nu}l)dl. \tag{2.73}$$

This integral can be halved by recognizing that the interferogram should be an even function.

One further complication comes when converting the retardation/time delay space to wavenumber space. Fourier transforms include an integral from $-\infty$ to ∞ or, for even functions, twice an integral from zero to ∞. It is impossible to achieve this by varying a mirror displacement to infinity, so the data set is truncated, as indicated above, to within a span of $\Delta(\tilde{\nu})^{-1}$. This defines the resolution of the interferogram and the subsequent wavenumber transform distribution. The true wavenumber distribution is desired, so one can think of $M'(l)$ being convolved with a boxcar truncation function

$$D(l) = \begin{cases} 1 & \text{for } -(\Delta\tilde{\nu})^{-1} \leq l \leq (\Delta\tilde{\nu})^{-1} \\ 0 & \text{otherwise} \end{cases} \tag{2.74}$$

which introduces what is known as an instrument function that is convolved with $M(\tilde{\nu})$ after Fourier transformation. The natural instrument function of a finite retardation length (the boxcar function) is the sinc function, seen in

[15]If one wants a resolution of 1 GHz in the frequency response, the translating mirror must move through a wavelength equivalent to a 1 GHz electromagnetic wave in air or vacuum.

Figure 2.11b, which introduces fringing effects into the convolved spectrum, $M(\tilde{\nu})$.

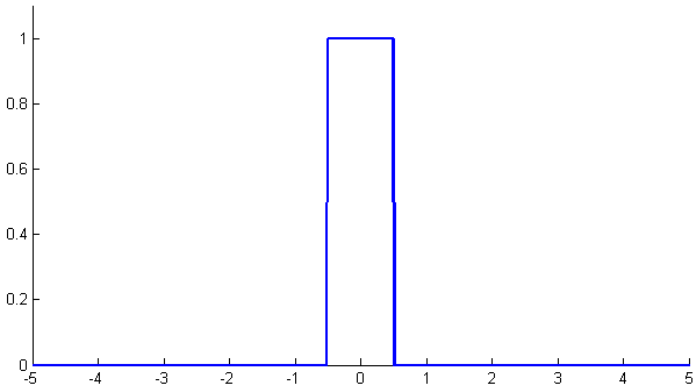

(a) A boxcar function.

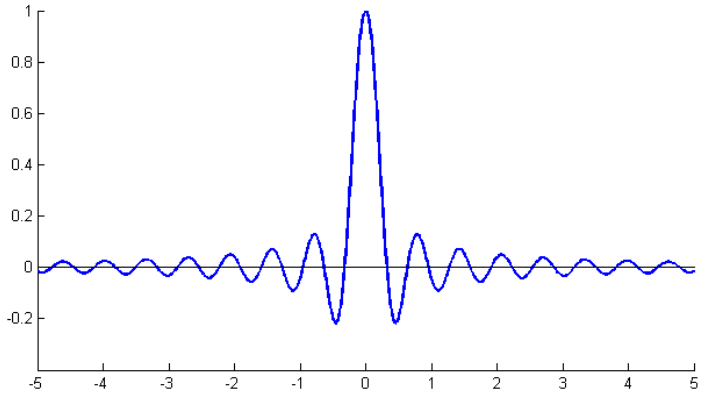

(b) A sinc function.

Figure 2.11: The boxcar function, which represents the truncation of a data set, becomes a sinc function after being Fourier transformed.

To mitigate the effect of finite retardation, $M'(l)$ can be multiplied by an apodization function, $A(l)$, such as a triangle function or a Happ-Genzel function, seen below, centred on $l = 0$. These functions provide a smoother transition to zero at the edge of the the data set.

$$A(l) = 0.54 + 0.46\cos(\pi \frac{l}{(\Delta\tilde{\nu})^{-1}}) \tag{2.75}$$

Apodization is not explicitly needed if the features of interest are greater than the wavenumber resolution [43]. With apodization, the system response is

$$M(\tilde{\nu}) = 2\int_{-\infty}^{\infty}(M'(l) - \frac{M'(0)}{2})A(l)\cos(2\pi\tilde{\nu}l)dl \tag{2.76}$$

Chapter 3

Antenna and filter design

This chapter outlines the design of the antenna and filter subsystems that direct signal power to the superconducting bridge. A general schematic outline of the system dynamics is shown to explain the role each subsystem plays. An integral part of the process is a low-pass filter, and designs and simulations of stepped-impedance filters are shown. Designs of planar antennas used to couple signal radiation into the integrated circuit device are also outlined and simulated.

The intention is to design with both Nb on Si and YBCO on MgO[1]. Material requirements and industrial realities are discussed throughout the discussion and also summarized at the end.

For all simulations, the conductor is assumed to be gold, with $\sigma = 4.4 \times 10^9$ S/m [39].

3.1 Sensor operation schematic

As discussed in Chapter 2, a superconducting thin film bridge can react greatly to DC and high frequency power that is fed across it. Sensing the radiation from afar requires an antenna system to couple the radiation into a microstrip line or coplanar waveguide feed line and, subsequently, to the superconducting bridge. A low-pass filtering system is used to keep the high frequency power contained with the bridge while still allowing the desired response to escape and be detected. Figure 3.1 outlines this idealized operation.

[1]Both substrate crystals are of the (100) orientation.

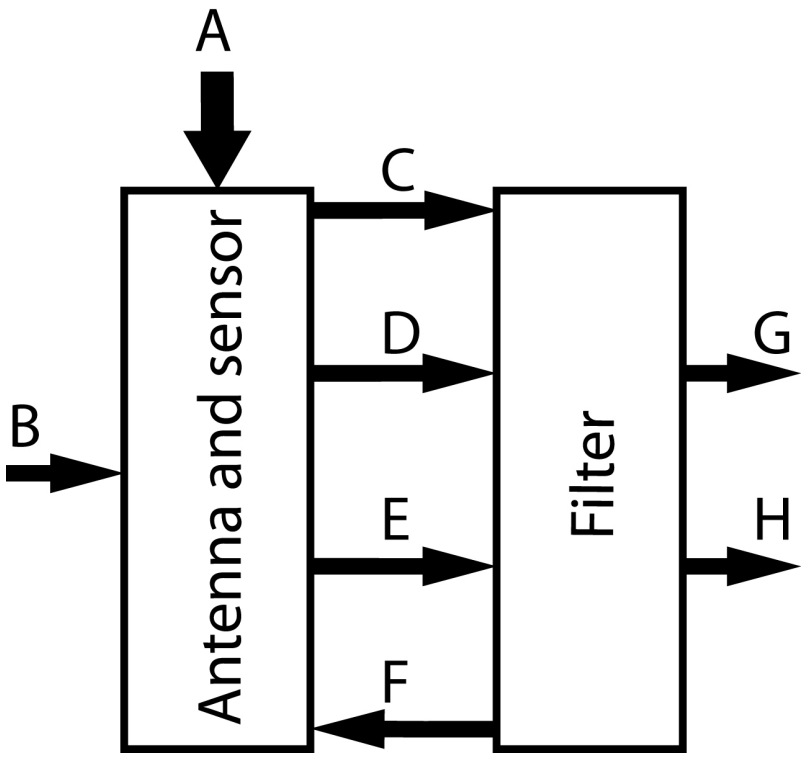

Figure 3.1: A general block diagram of the sensor, filter, and antenna system. Power flow in various forms is represented by the lettered arrows. (A) is the input high frequency signal in the form of a plane wave. (B),(C) and (G) are the DC bias, unaffected by the filtering. (D) and (H) are the direction of the intermediate frequency signal, also unaffected by the low-pass filter. (E) and (F) show some of the high frequency signal traveling to the filter, but reflecting back toward the bridge.

3.2 Choice of frequencies

Two sensor frequencies were chosen for detection. They are 60 GHz and 380 GHz for detectors based on silicon substrates (shifting to about 64 GHz and 400 GHz for MgO substrate). The choice of 60 GHz was to allow for the strong oxygen absorption [43] at this frequency to aid in determining if the HEB is functioning. The oxygen pressure can be varied in a transmission chamber and the signal from the HEB should attenuate if is detecting radiation at this frequency. The opposite is true for 380 GHz to 400 GHz. This is in the midst of a transmission frequency window in the atmosphere [4]. Analysis of the properties of HEBs at these higher frequencies was deemed possible, so

designing sensors inside a window increases the amount of radiation power reaching the devices.

3.3 Filter subsystems

Low-pass filters that serve a high-frequency cutoff of about 60 GHz, 380 GHz and 420 GHz are required to attempt to ensure that a maximum amount of high frequency signal power remains to excite the electron in the biased bridge. The low-frequency cutoff for these filters are dependent on the local oscillator used. No local oscillator was available in anticipation of testing, so basing the IF bandwidth on expected sensor response times, τ_{diff} or τ_{e-p},

3.3.1 Stepped impedance filter prototype

Since the signal measured from the chip will be either DC or of a frequency one or two orders of magnitude lower than the observed signal(s), a stepped impedance chain can be used as a low pass filter to keep the observed signals contained within the superconducting bridge.

In both the microstrip line and coplanar waveguide implementations, the filters are first designed using maximally flat filter prototypes. These lumped numbers are then converted to distributed elements using Richard's transformation [44]. In each case, a series of low and high impedances act as a low pass filter.

3.3.2 Microstrip line stepped impedance filter

Using prototype parameters for a maximally flat filter in the case of $n = 4$, from [44], a four section low pass filter was designed. The cut off frequency was designed at $\nu_c = 25$ GHz to allow for the slow frequency roll off inherent to stepped impedance filters. Figure 3.2 shows the physical layout of the microstrip filters.

Table 3-I shows the lengths used for the low pass filter. The impedances were $Z_l \approx 5\ \Omega$ and $Z_h \approx 125\ \Omega$. The filter was modeled in CST Microwave Studio and simulated at both the span about the antenna resonant frequency (where $S_{2,2}$ should be close to 0 dB) and from DC to 10 GHz. Figure 3.3 shows

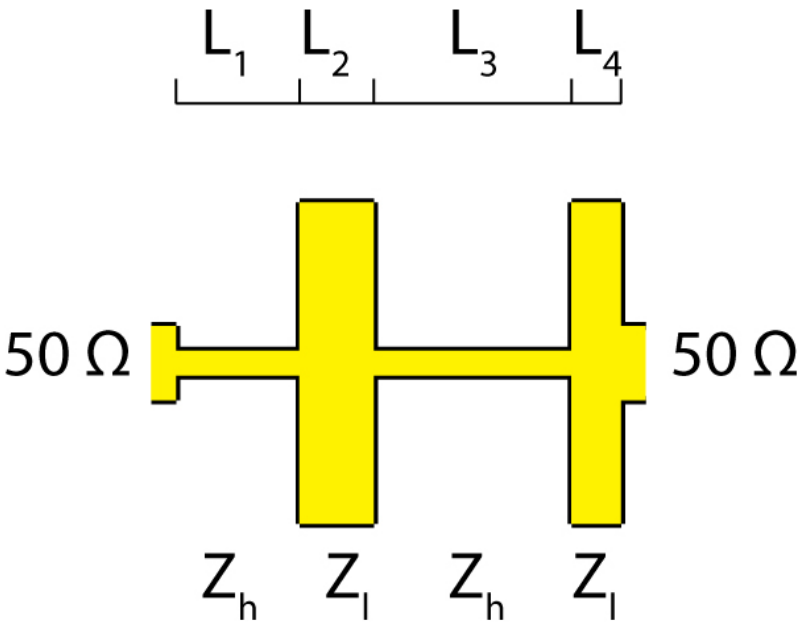

Figure 3.2: A four section stepped impedance low pass filter. Both ends are terminated to 50 Ω microstrip lines. Port 2 is designated to be the left side of the filter, and port 1 the right.

$S_{2,2}$ is 1 dB or less from 54 GHz to beyond 64 GHz, with minimal rippling. $S_{1,2}$ shows that the filter should attenuate signal power reaching port 1 from port 2 by more than 20 dB, from 57 GHz to about 64 GHz.

According to (2.63), assuming $\sigma = 4.4 \times 10^9$ S/m, the skin depth in gold will be 30 nm at 60 GHz and 12 nm at 400 GHz. The gold layer need only be a few skin depths deep as the majority of the current will flow in this layer regardless of thickness. 400 nm was chosen as the metal layer thickness. At this thickness, electrons are given several skin depths in which to conduct and, more importantly, wirebonds can be attached to metal layers to take signals off of the chips. It was found from testing that this is as thin a metal layer could be for bonding to occur predictably.

The dielectric constant and loss tangent of the substrate were taken as described in Chapter 2.

The bandwidth of a Nb on Si HEB mixer will be, at most, 1 GHz. The filter is expected to add slightly less than 1 dB of attenuation at low frequencies, likely due to the lossy materials. This translates to about 90 percent signal

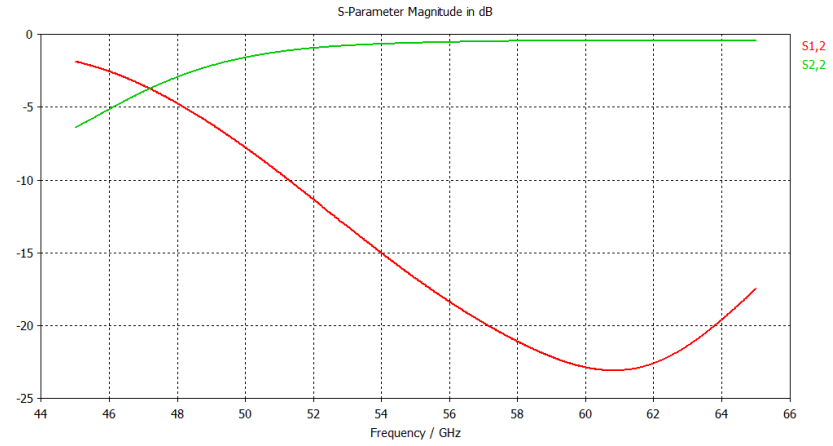

(a) About the antenna resonant frequency

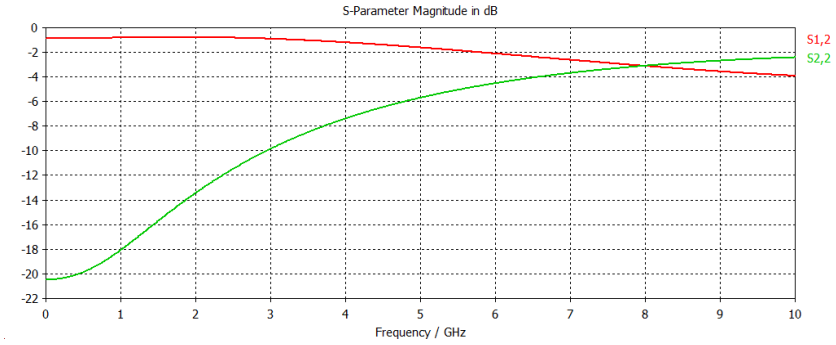

(b) At the measured signal frequencies

Figure 3.3: The simulated frequency response of the filter in terms of the S-parameters at the two ports.

Table 3-I: Microstrip filter lengths.

Section	Length (μm)
L_1	323
L_2	133
L_3	323
L_4	66

transmission at these frequencies.

3.3.3 Coplanar waveguide stepped impedance filter

The stepped impedance filter for the 380 GHz and 400 GHz twin slot antenna couple HEBs will use a similar approach as above. The difference is merely the use of coplanar waveguide sections to realize the impedances, instead of microstrip lines. This can be seen in Figure 3.4, where the gray areas represent the portions of the ground plane removed to make the waveguide gaps.

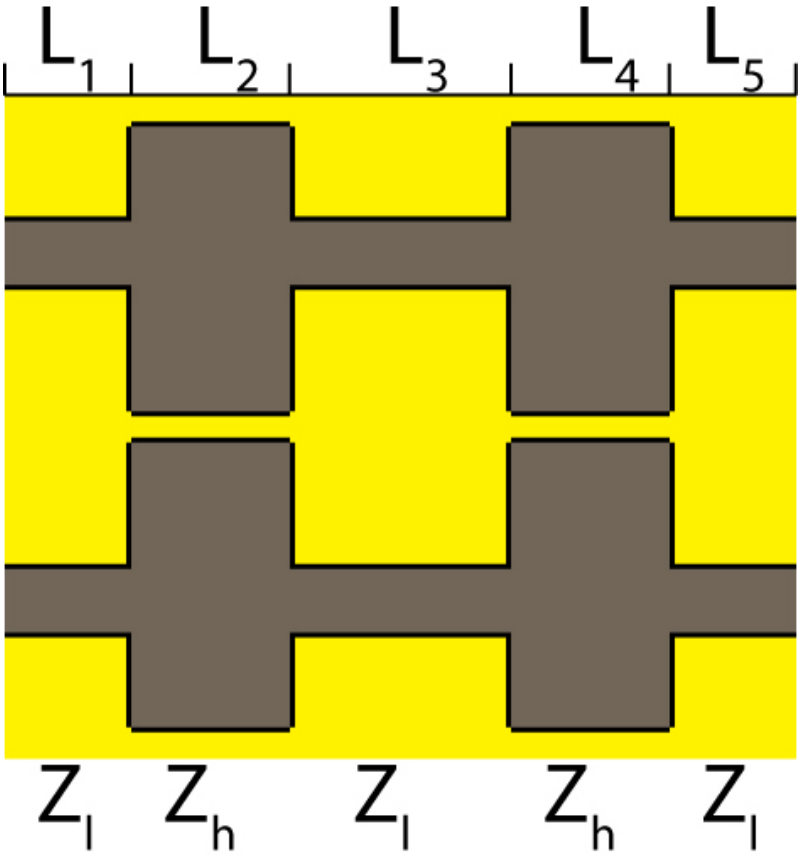

Figure 3.4: A stepped impedance low pass filter using a coplanar waveguide.

The filter lengths are seen in Table 3-II. This filter was modeled and simulated in CST Microwave Office over a frequency range of 300 GHz to 400 GHz, and an accuracy of -40 dB. It was assumed that the majority of the power will

Table 3-II: CPW filter lengths

Section	Length (μm)
L_1	27.5
L_2	62.6
L_3	88.7
L_4	62.6
L_5	27.5

transmit by one mode. Figure 3.5 shows an expected return loss of -2 dB at 380 GHz. From DC to 5 GHz, the filter has an attenuation below 1 dB. This is seen in Figure 3.6.

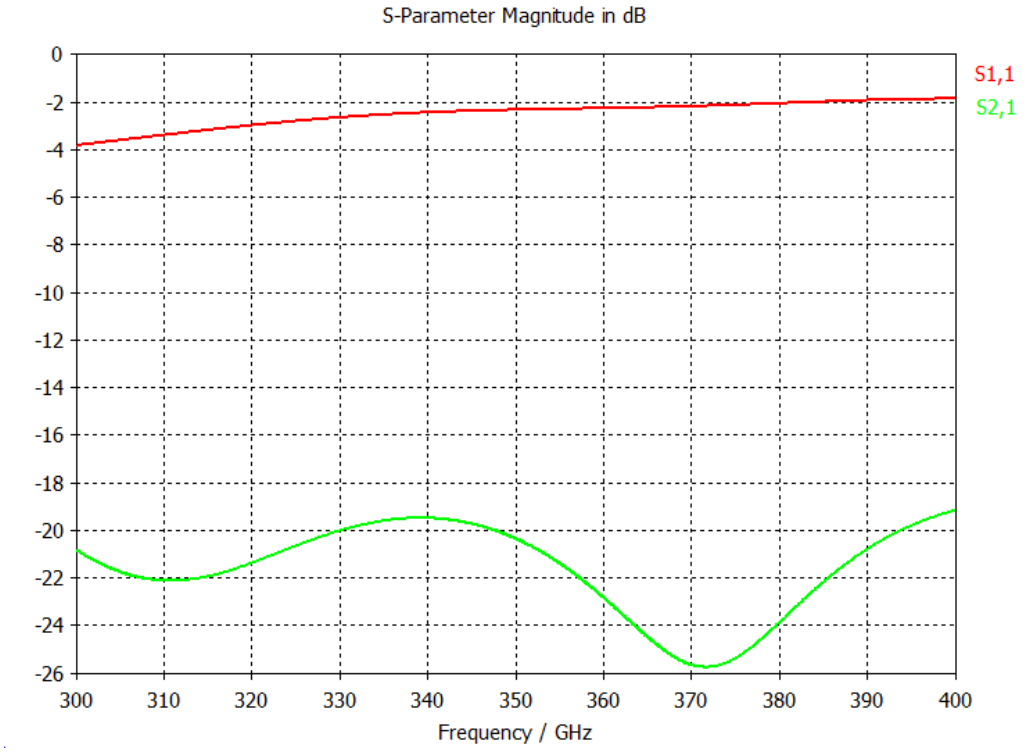

Figure 3.5: The $S_{1,1}$ and $S_{2,1}$ for the coplanar waveguide filter, from 300 GHz to 400 GHz.

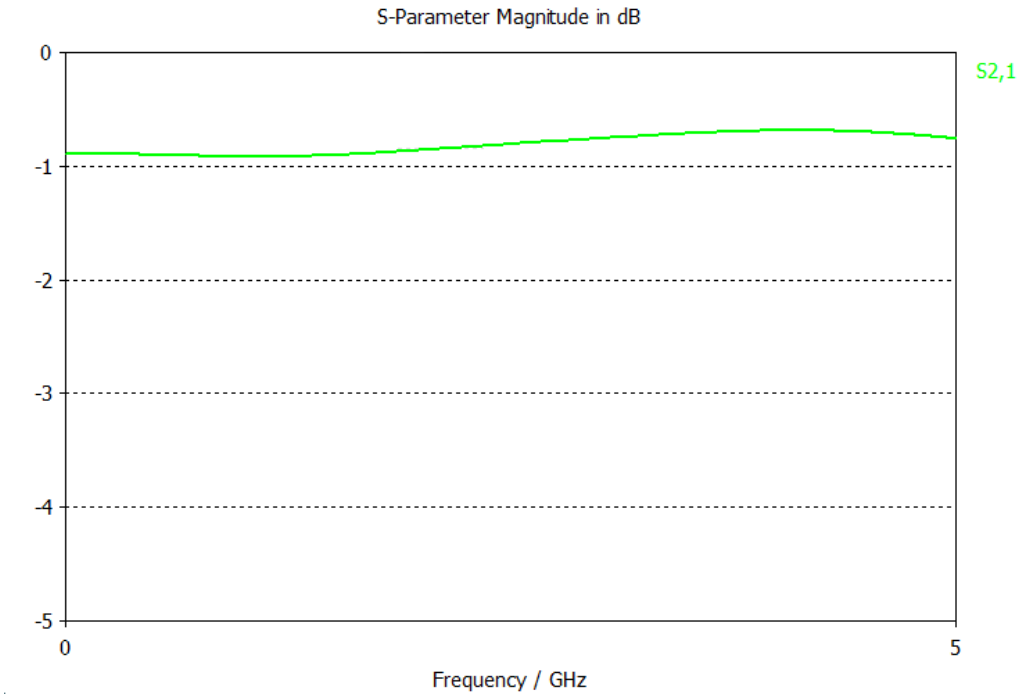

Figure 3.6: $S_{2,1}$ for the coplanar waveguide filter, from DC to 5 GHz.

3.4 Antenna subsystems

Planar antennas were chosen to couple the radiation to the bridge. For the design at 60 GHz, two microstrip antennas were used on either side of a microstrip line feed to the bridge. Slot antennas coupled to a coplanar waveguide were used for antennas with centre frequencies of 380 GHz and 400 GHz.

The substrate choice depends on the superconductoring film to be grown. Intrinsic and high-resistivity silicon were chosen for niobium films. Niobium adheres strongly to (100) silicon, and the price for high quality silicon wafers is typically lower than other high quality crystal substrates due to the size and extend of the silicon semiconductor industry. The loss tangent is also low at the operating temperatures (below 10 K), with $\tan\delta = 6 \times 10^{-6}$ and $\tan\delta = 2 \times 10^{-4}$ at 60 GHz and 400 GHz, respectively. These are assumed to be constant over the antenna bandwidth.

The antenna designs for antennas on silicon were translated to YBCO on

magnesium oxide[2]. Simulations are conducted replacing silicon for MgO, and the validity of the design is checked for the new material.

In both cases, the microstrip or coplanar waveguide low pass filters outlined above were placed in such a manner to trap as much THz or millimetre wave power in with the microbridge for as long as possible. The entire antenna and filter system was simulated in CST Microwave Studio in order to gauge antenna performance and farfield characteristics.

3.4.1 Rectangular microstrip antennas

The initial dimensions for the microstrip antennas were determined by a transmission line model [45] then simulated in CST Microwave Studio. The expectation, which held true, was that the transmission line model provides only a starting point, and the dimensions must be adjusted with parameter sweeps to increase the antenna gain and adjust the main beam direction. A rectangular microstrip antenna can be seen in Figure 3.7. The slots cut into the antenna are for impedance matching.

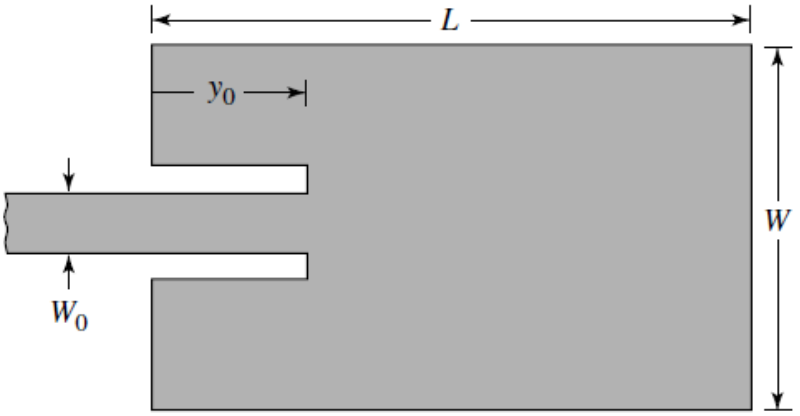

Figure 3.7: A rectangular microstrip antenna with dimensional parameters. The resonant length is L, the width is W, and the width of the microstrip feed line is W_0. Impedance matching slots are of length y_0. Reproduced from [45].

The antenna is linearly polarized along the length L.

[2]The use of YBCO was decided after a chrome mask was ordered.

Microstrip antenna transmission line model

The substrate height, h_s, is assumed to be much less than the width of the rectangular microstrip antenna. In order to minimize losses due to unwanted modes traveling outside the microstrip line, the height is chosen so that only TM_0[3] for the highest frequency is likely to propagate in the grounded dielectric slab. TM_0 will propagate at DC, so this is impossible to prevent for any grounded slab. The cutoff height h_c for the TE_1 mode should be greater than h_s. For the highest frequency in the substrate, ν_h, the substrate height cutoff is

$$h_c = \frac{nc}{2\nu_h\sqrt{\epsilon_r - 1}} \tag{3.1}$$

in terms of the TM_n modes, for $n = 0, 1, 2, 3...$ and the speed of light, c. Similarly, the cutoff height for the TE_n modes as is found from

$$h_c = \frac{(2n-1)c}{4\nu_h\sqrt{\epsilon_r - 1}} \tag{3.2}$$

for $n = 1, 2, 3, 4....$ For a frequency of about 65 GHz, $h_s = 135$ μm will minimize the number of TE and TM modes that can propagate freely in the grounded dielectric about the microstrip antenna and feed.

With the substrate height chosen, a good initial value for the width of a microstrip antenna for a given centre frequency, ν_c, is

$$W = \frac{1}{2\nu_c\sqrt{\epsilon_r}\sqrt{\mu_0\epsilon_0}}\sqrt{\frac{2}{\epsilon_r + 1}} \tag{3.3}$$

for a given ϵ_r. Due to the operation of the antenna in two media, the model calculates an effective dielectric constant,

$$\epsilon_{eff} = \frac{\epsilon_r + 1}{2} + \frac{\epsilon_r - 1}{2}\left[1 + 12\frac{h_s}{W}\right]. \tag{3.4}$$

The transmission line model includes a length correction, ΔL, for the difference between the electrical length (or rather the extension on one end) and

[3]The analysis is done in a one dimensional case. The order of propagation, for increasing dielectric slab height, is TM_0, TE_1, TM_1, TE_2, TM_2 and so on. Each will start propagating once the appropriate cutoff height is reached.

the physical length of the antenna, which is estimated by

$$\Delta L = 0.412 h_s \frac{(\epsilon_{eff} + 0.3)(\frac{W}{h_s} + 0.264)}{(\epsilon_{eff} - 0.258)(\frac{W}{h_s} + 0.8)} \tag{3.5}$$

which leads to the estimate of the physical length of the antenna,

$$L = \frac{1}{2\nu_c \sqrt{\mu_0 \epsilon_r \epsilon_0}} - 2\Delta L. \tag{3.6}$$

The impedance of the feed line should be matched as closely as possible to the antenna. By placing two slots on either side of the input feed line, as in Figure 3.7, the feed line can be matched to any resistance from R_{ant}, the maximum at $y_0 = 0$ to zero Ω. This variation is illustrated in Figure 3.8.

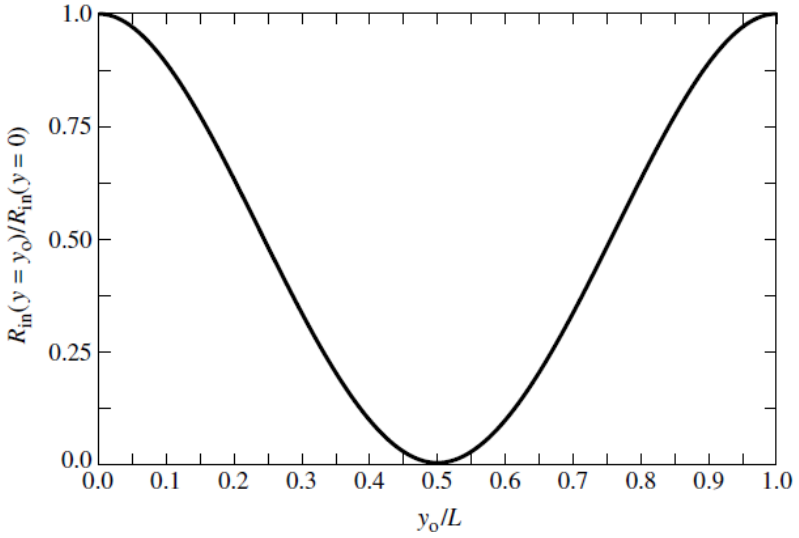

Figure 3.8: The variation of the input resistance seen by the feed line for slot length, y_0. Taken from [45]

The input resistance into the antenna, at a distance y from the edge, can be appoximated by

$$R_{ant} = R_{edge} \cos^2\left(\frac{\pi y}{L}\right) \tag{3.7}$$

which uses the physical length found in (3.6) and R_{edge} is the resistance at the

edge. This can be estimated from

$$R_{edge} = \eta_0 \mu_r \frac{4Lh_s}{\pi W \lambda_0} Q. \tag{3.8}$$

It is assumed that the relative permeability is $\mu_r = 1$. $\eta_0 \approx 377\ \Omega$ is the impedance of free space, and Q is the quality factor. Q is estimated, as in [46], from the bandwidth and simulated voltage standing wave ratio.

Dual microstrip antenna

Two microstrip antennas were placed one on either side of the superconducting bridge, as seen in Figure 3.9. The centre frequency of the two antennas are offset so one side receives the signal of interest and the other receives any local oscillator signal, both to mitigate interference between the received signal at the bridge, from each antenna, and to improve the receiving efficiency of the local oscillator and signal of interest.

The bandwidth of a mixer-based system depends on the antennas and HEB relaxation time. In the case of a Nb on Si phonon-cooled HEB, the bandwidth based on the electron-phonon relaxation time should be less than 1 GHz. 500 to 150 MHz are more realistic values, as stated in Chapter 2. In this case, only one microstrip antenna will be needed to achieve the required bandwidth. For YBCO, the bandwidth possible from a 100 nm thick phonon-cooled bridge is limited by the phonon escape time. This is reported as 5 GHz to 8 GHz, for τ = 125 ps to 200 ps [47]. This can be increased by lowering the device thickness, but at the risk of destroying superconductivity. If the bridge is made from YBCO, the bandwidth is taken as the difference in the centre peaks of the two antennas, 1.6 GHz for the design on Si and 1.3 GHz for the same antennas on MgO.

To further mitigate any effects of destructive interference between the two antennas, the length between the two antennas is an odd multiple of $0.5\lambda_c$. λ_c is the wavelength of the centre frequency of the 60 GHz microstrip antenna.

Four ports were used in the CST Microwave Studio simulations, using the transient solver at a -40 dB accuracy. Ports 1 and 3 signify radiation leaving the bridge to the left and right, in terms of Figure 3.9, respectively. Ports 2 and 4 were placed on the left and right most extremes of the chip, after the

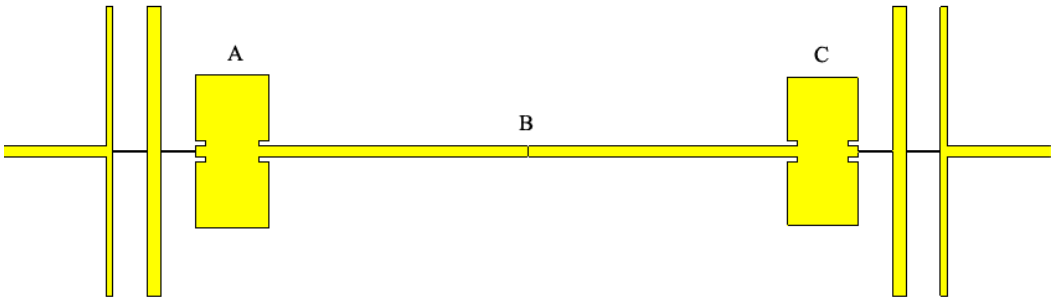

Figure 3.9: The dual microstrip HEB, including the stepped impedance filters on either side. A and C are the two antennas, and B signifies the bridge location.

filters. The S-parameters of a simulation can be seen in Figure 3.10. The two antenna centre frequencies, at 58.4 GHz and 60 GHz, can be clearly seen by $S_{1,1}$ and $S_{3,3}$. $S_{2,1}$ and $S_{4,3}$ are consistently below -20 dB, signifying that the filters are preventing the high frequency signals from leaving the region containing the superconducing bridge, as intended. The frequency range used in CST was 52 GHz to 63 GHz.

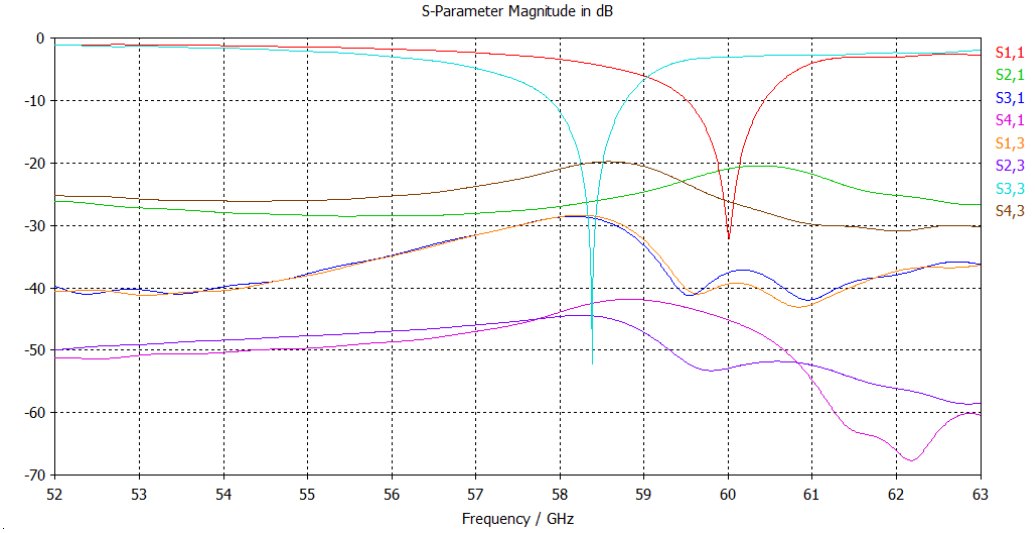

Figure 3.10: The S-parameters of a dual microstrip antenna simulation. $S_{1,1}$ and $S_{3,3}$ show the two microstrip antenna's resonant frequencies.

Farfield plots were created via simulation in CST Microwave Studio, one at the centre frequency of each antenna. At 60 GHz, the antenna shows a gain of 3.2 dB (or 2.1, in a linear scale) perpendicular to the substrate. This is shown in Figure 3.11, where the gain, G_{ant}, is found from the product of the directivity, D_{ant}, and the radiation efficiency, $\epsilon_{ant} = 0.52$. The addition of the losses to the antenna from reflections from the port location sees a minimal reduction in efficiency, with $\epsilon_{total} = 0.515$.

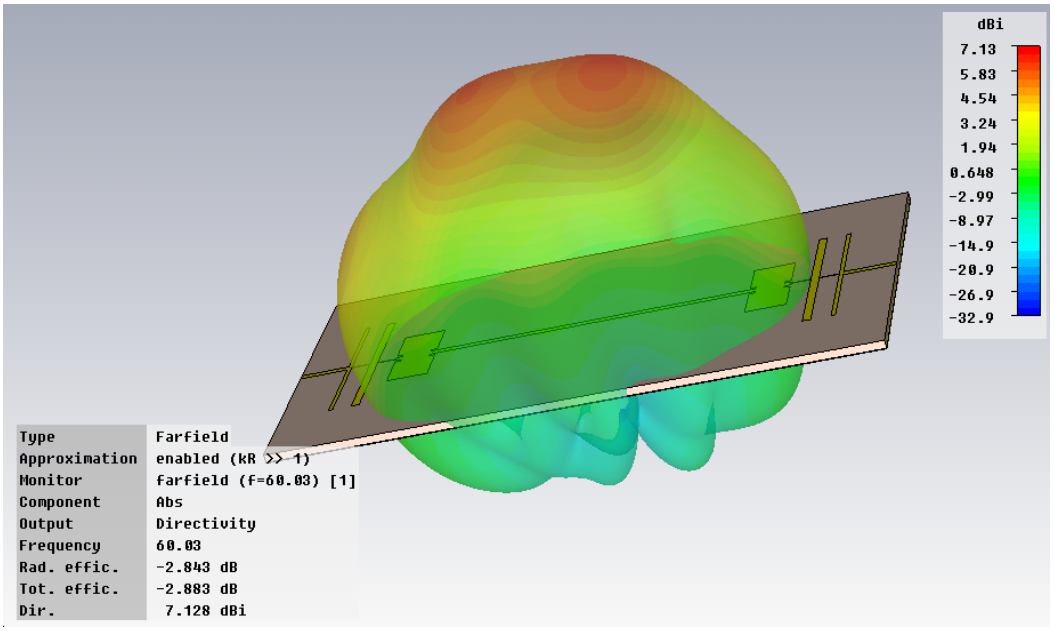

Figure 3.11: A farfield plot generated at a frequency of 60.03 GHz.

At 58.4 GHz (Figure 3.12), the gain of the antenna is comparible to the 60 GHz case. 3.4 dB (2.2 linear) is taken as the antenna gain at this frequency.

The same antenna dimensions are simulated again with a 250 μm MgO substrate. This is done to see if the photolithography mask made for Nb HEBs is compatible with YBCO HEBs. It is expected that the centre frequencies will shift, but, operation as a sensor is still possible. The return loss ($S_{1,1}$ and $S_{3,3}$) curves are shown in Figure 3.13. The centre frequencies have shifted from 58.4 GHz and 60 GHz to 61.1 GHz and 62.4 GHz.

The farfield patterns (Figure 3.14) show that the gain of the system has also changed. The gain is 1.9 dB and 1.3 dB at 61.1 GHz and 62.4 GHz,

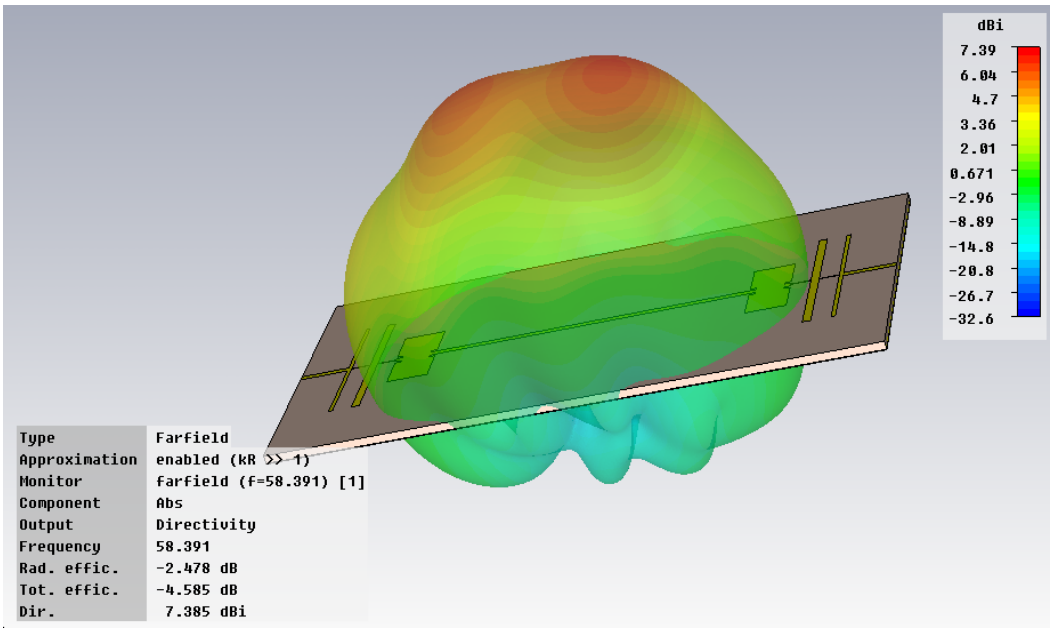

Figure 3.12: A farfield plot generated at a frequency of 58.39 GHz.

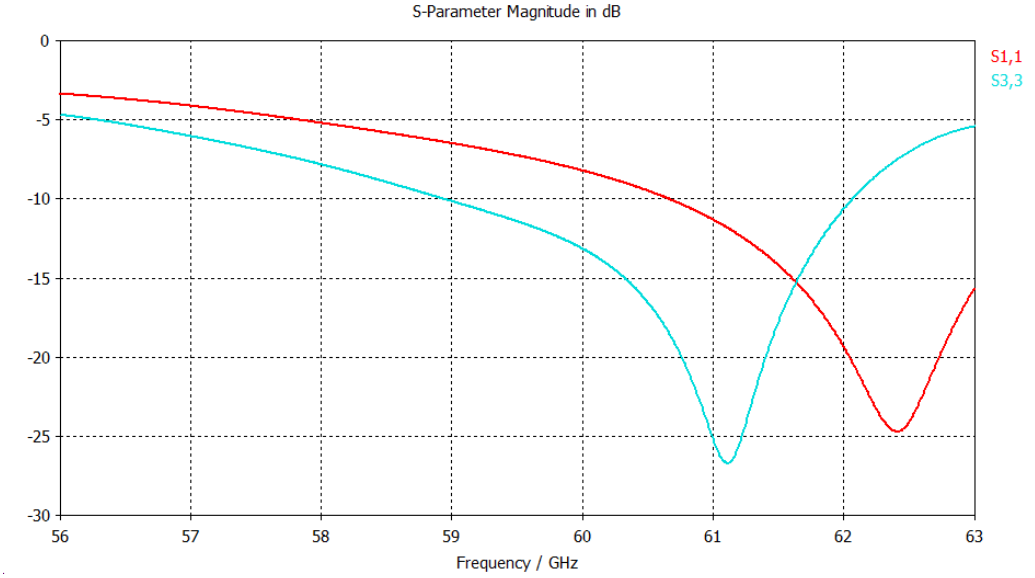

Figure 3.13: Simulated return loss for the microstrip antennas on magnesium oxide substrate.

respectively.

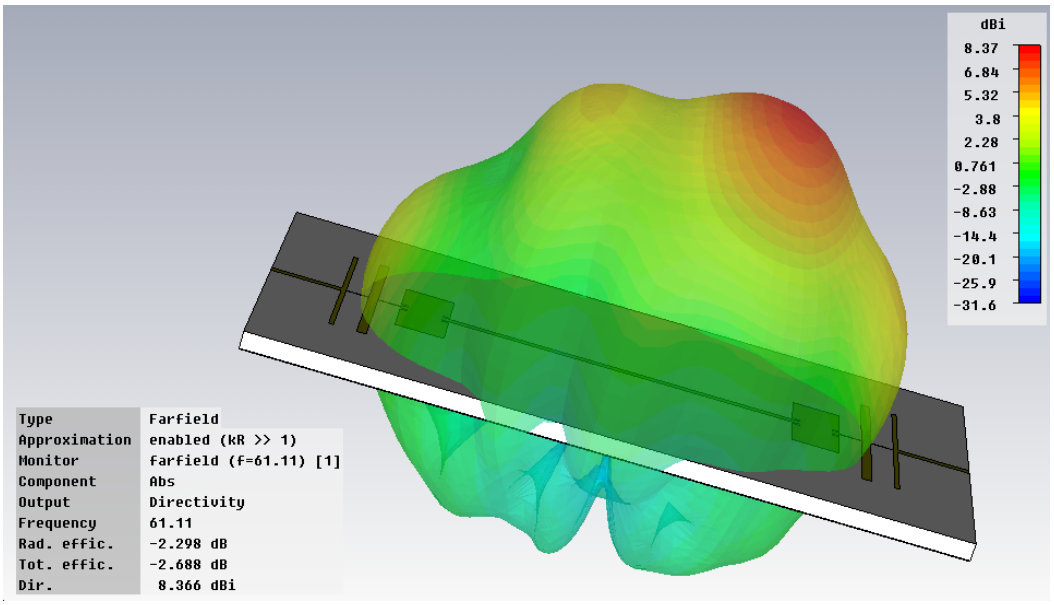

Figure 3.14: A farfield plot at 61.1 GHz of the dual microstrip antenna system on MgO.

The bandwidth estimation based on simulations of the antennas is taken as the frequencies when the voltage standing wave ratio is less than 2. For the microstrip antenna on silicon, each antenna has a bandwidth of approximately 1 GHz, seen in Figure 3.15. This translates to a fractional bandwidth of 0.017 of the centre frequencies, for both antennas.

The same antenna pair simulated on the 250 $/mu$m magnesium oxide substrate see a broadened bandwidth (Figure 3.15). The fractional bandwidth is 0.054 at 62.4 GHz, and 0.057 at 61.1 GHz, using the VSWR estimation.

Estimating the Q factors from the simulated bandwidths will yield the antenna input resistance from (3.8). The Q factors of the antennas on silicon are both estimated to be 41.6. The input resistances are calculated to be 253 Ω and 260 Ω for the 58.4 GHz antenna and the 60 GHz antenna, respectively. The Q factors of the antennas on MgO are 12.4 (61.1 GHz) and 13.1 (62.4 GHz), leading to input resistances of 141 Ω and 152 Ω, respectively.

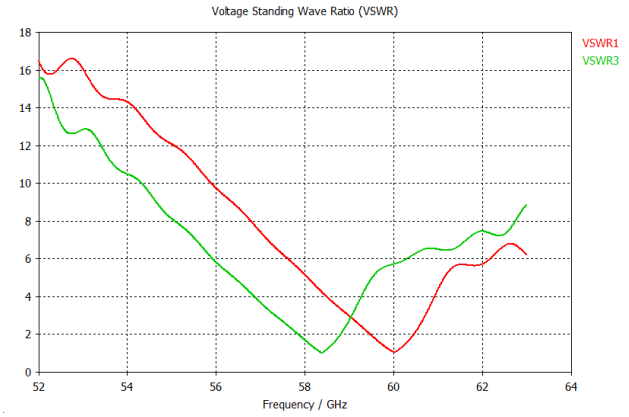

(a) Silicon substrate

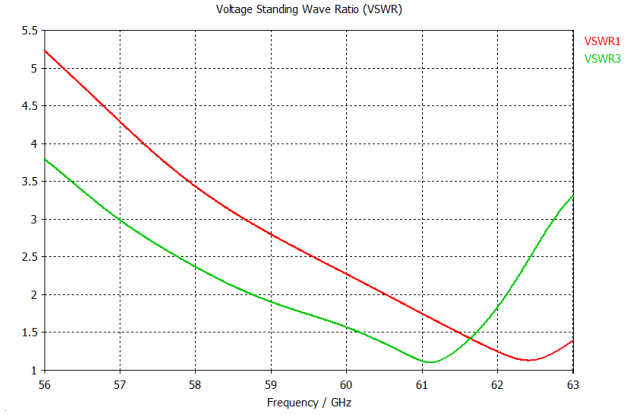

(b) Magnesium Oxide substrate

Figure 3.15: The voltage standing wave ratio calculated from the Microwave Studio simulations.

3.4.2 Slot antennas

The second antenna type uses a pair of identical slots cut into a ground plane on a dielectric. A coplanar waveguide connects the two slots, and houses the superconducting bridge.

Twin slot antennas

At higher frequencies, substrate thicknesses of microstrip antennas need to be lowered. This means crystal substrates become more fragile and more difficult with which to fabricate devices. While commercially available Si substrates are sold with thicknesses down to 10 μm, the cost and thin film manufacturing

difficulties precluded their use at Stellenbosch University. Microstrip lines in general are more restricted in their characteristic impedances when compared to a coplanar waveguide, which has two parameters that can control Z (based on deposition of metals).

Slot antennas can make use of thicker substrates (greater than a wavelength in the dielectric) and the superconducting bridge can be placed across a coplanar waveguide that couples the two structures together. Typical dimensions of a coplanar waveguide fed twin slot antenna are shown in Figure 3.16. The effective wavelength, λ_{eff}, is the wavelength of the centre frequency of the antenna. It can be found by averaging the (relative) permittivities of the vacuum and substrate on either side of the antenna, so $\epsilon_{eff} \approx (\epsilon_{vac} + \epsilon_{sub})/2$ for a finite substrate. The effective wavelength is then, $\lambda_{eff} = 1/(\epsilon_{eff}\epsilon_0\mu_0\nu_c)$ for centre frequency, ν_c.

The two slots should be placed $\lambda_{eff}/2$ apart and be $0.72\lambda_{eff}$ in length [48]. Substrate thickness should be a multiple of $\lambda_{sub}/4$, a quarter of the wavelength of the signal entirely in terms of the dielectric's permittivity, ϵ_{sub}. An odd multiple is preferable for maximal gain [48]. The combined width of the centre metal strip and two gaps should be less than 10 percent of the antenna length to maintain resonance [49]. The antenna is electrically polarized perpenducular to the slot length (across both slots).

If a slot is surrounded on both sides with a volume of equal permittivity, the radiation pattern on one side of the metallic ground plane would be the reflection of the radiation pattern on the other side of the plane. If, instead, one side is a material with a higher permittivity, the field lines would tend to pull into this material rather than the other side. In the case of silicon on one side and a vacuum on the other, the antenna should radiate down into the substrate.

A twin slot antenna on silicon with a desired resonant frequency of 380 GHz was constructed in CST Microwave Studio. The antenna had a length of 223 μm, a slot width of 25 μm, with a spacing between slots of 155 μm. The coplanar waveguide was designed to have an impedance of 50 Ω. These dimensions, like with the microstrip antenna case above, were altered by a parameter sweep seeking to maximize the s-parameters and directivity of the antenna. The silicon substrate is $1.75\lambda_{sub} = 400$ μm, which is 7 times the

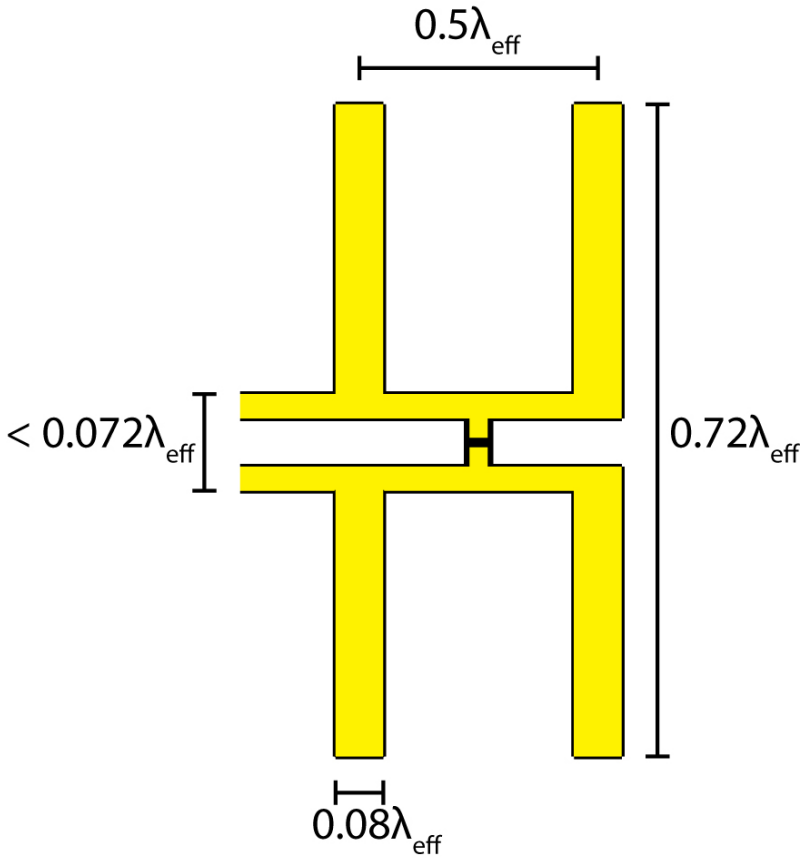

Figure 3.16: A twin slot antenna dimensions in terms of the effective wavelength, λ_{eff}, of the centre frequency of the antenna.

wavelength of the centre frequency, in silicon.

The twin slot antenna was simulated on silicon (400 μm thickness) and magnesium oxide (500 μm thickness). The return loss for each case is shown in Figure 3.17 and Figure 3.18. The silicon-based system shows a centre frequency of 378 GHz and a return loss of -37 dB. When simulated on magnesium oxide, the same antenna dimensions results in a higher centre frequency of 398 GHz. The return loss at this frequency is -38 dB.

A farfield plot at 378 GHz can be seen from two angles in Figures 3.19 and 3.20. As expected, the antenna radiates mainly into the substrate side of the device. The main lobe of the farfield is skewed toward the coplanar waveguide filter (Figure 3.19), while appearing to radiate perpendicularly along the waveguide propagation direction. Asymmetry in the ground plane may be

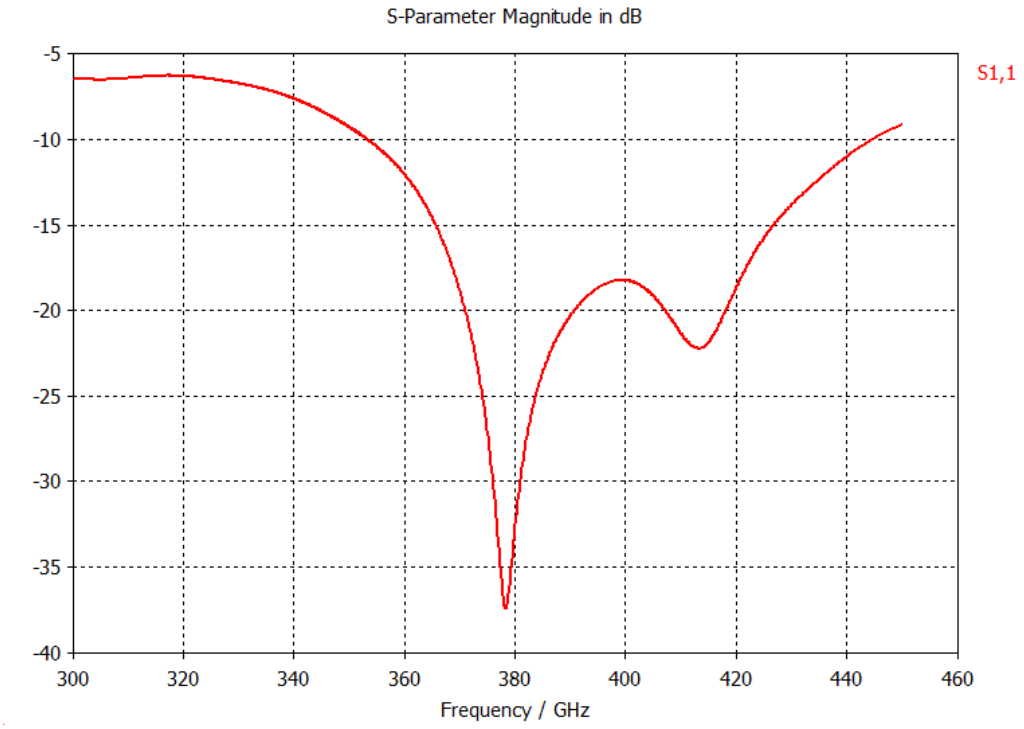

Figure 3.17: $S_{1,1}$ plot for the twin slot on a silicon substrate.

responsible for the beam skew.

The gain perpendicular to the underside of the substrate is approximately 2 (in a linear scale), with a simulated radiation efficiency of 0.98. The fractional bandwidth of the antenna is estimated to be 0.25 times the centre frequency.

The farfield performance of the antenna on MgO, at its resonant centre frequency of 398 GHz, is shown in Figures 3.21 and 3.22. The lobes are greatly altered from the case of thinner silicon substrate, but a gain of 2.3 is still achieved perpendicular to the underside of the substrate. This is despite a lower radiation efficiency, which is simulated to be 0.59 compared to the near unity of the 380 GHz case. The bandwidth is estimated to be lowered to 0.19 times the centre frequency.

The skewing of the radiation pattern into the substrate is more pronounced than with the silicon substrate. Changes in the impedances of the filter sections and the slots may account for the change, along with the continued asymmetry of the ground plane.

The simulations suggest that both the microstrip line antennas and the

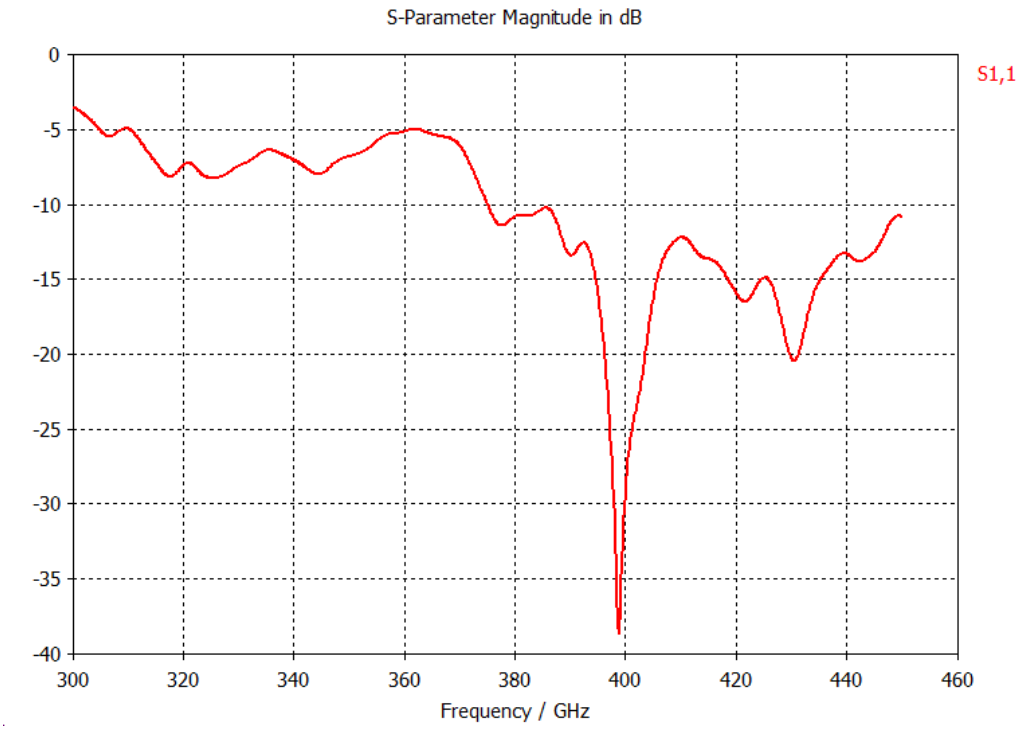

Figure 3.18: $S_{1,1}$ plot for the twin slot on a magnesium oxide substrate.

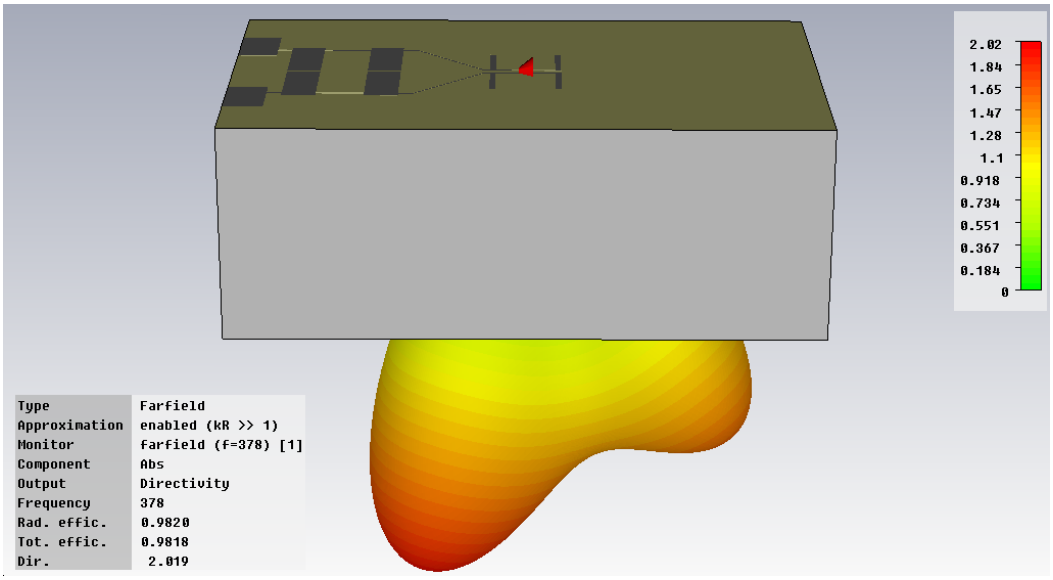

Figure 3.19: The farfield plot of a twin slot antenna at 378 GHz, viewed from perpendicular to the CPW axis. The scaling of the directivity is linear.

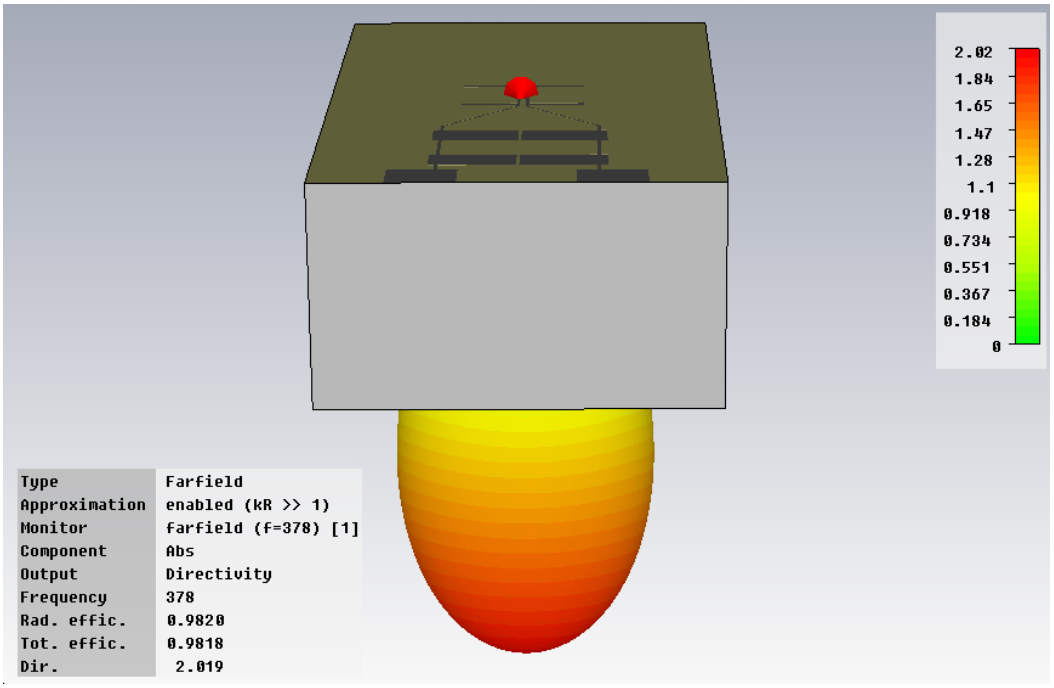

Figure 3.20: The farfield plot of a twin slot antenna at 378 GHz, viewed from along the CPW axis. The scaling of the directivity is linear.

twin slot antenna will work as THz or millimetre wave receivers. Additionally, using the same device dimensions, on two different substrates, while altering the gain of the antennas, should still allow operation. This facilitates the use of both niobium and YBCO as the superconducting element. For the microstrip antennas on MgO, the gain is directed similarly to the case of a silicon substrate. This is not the case with the slot antennas, in which the main beam is skewed more towards the coplanar waveguide, but still maintains an estimated linear gain of 2.3. A subsequent design might improve the beam direction by placing additional slots opposite the antenna to balance the effect of the coplanr waveguide, as seen in [48].

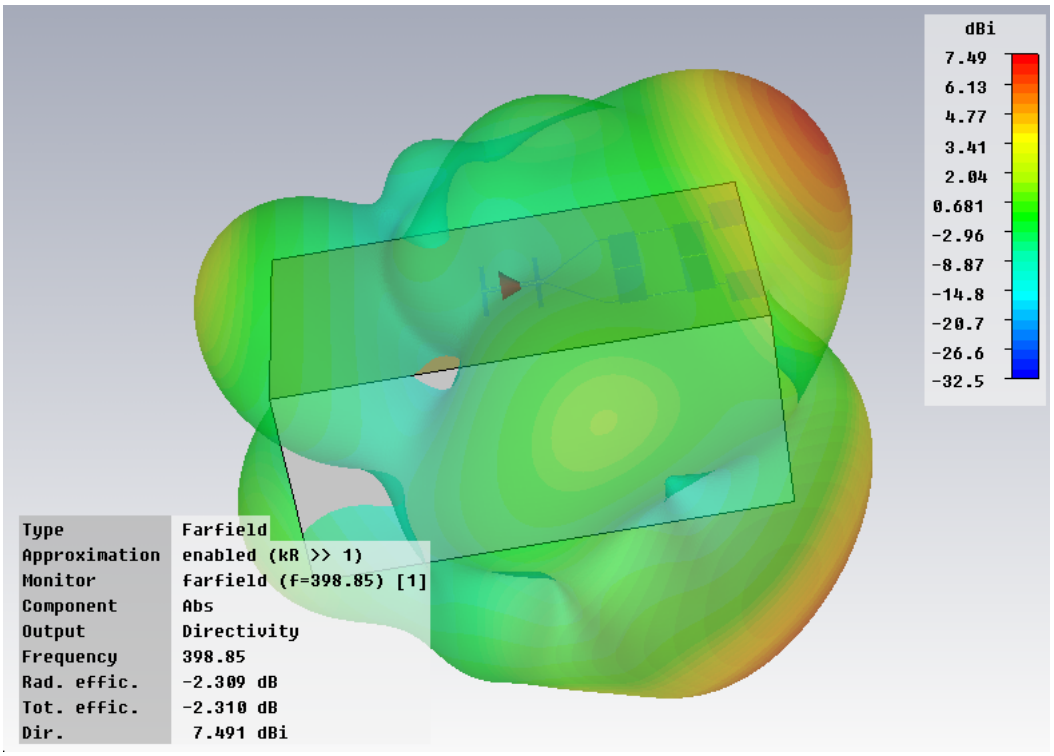

Figure 3.21: The farfield plot of the twin slot antenna at 398.85 GHz, looking perpendicular to the CPW axis. The plot is of the directivity, and is in dBi.

Table 3-III: Compilation of relevant antenna performance parameters.

Type	Device	Simulated ν_c (GHz)	Gain (dB)	Total efficiency
Microstrip/Si	1	60.03	3.2	0.52
Microstrip/Si	1	58.39	3.4	0.35
Microstrip/MgO	2	61.11	1.9	0.56
Microstrip/MgO	2	62.4	1.3	0.5
Slot/Si	3	378	3.0	0.98
Slot/MgO	4	398.85	3.6	0.59

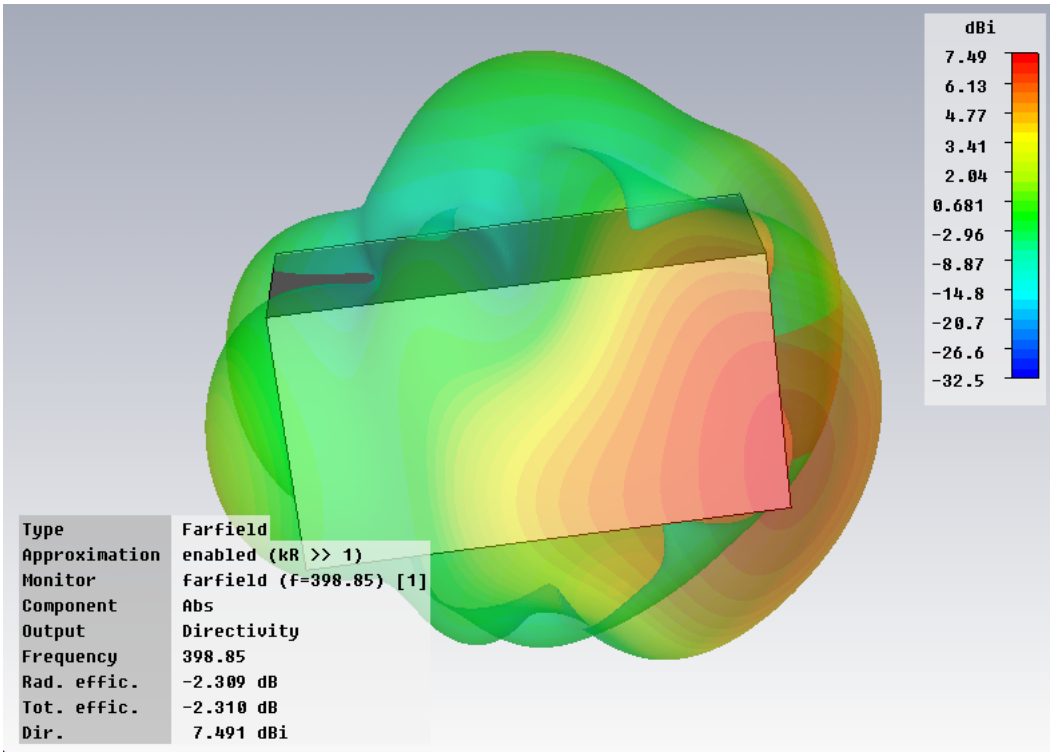

Figure 3.22: The farfield plot of the twin slot antenna at 398.85 GHz, looking at the underside of the substrate. The plot is of the directivity, and is in dBi.

3.4.3 Signal connection mismatch

The connection outside the chip will be, in the AC case, a 50 Ω line on a PCB which leads to a 50 Ω coaxial cable connection. The waveguide on the edge of the chip is designed to be 50 Ω for both the microstrip line and coplanar waveguide on silicon[4]. The photolithography mask manufacturer makes masks with a tolerance of 1 μm, so precise values of line widths is only possible to the manufacturers tolerance.

The actual impedances of the lines are 51.6 Ω for the microstrip line on Si and 49.9 Ω for the coplanar waveguide on Si. When the same microstrip line width is placed on a 250 μm thick MgO substrate, the impedance of the line changes to 72.0 Ω. This leads to a mismatch loss of 0.15 dB. The coplanar waveguide of the same dimensions over an MgO substrate will have an impedance of 54.6 Ω. This is a small mismatch that leads to a loss of −8.4

[4]These, and subsequent, values are calculated for 5 GHz. It is expected that the signal frequency measured off the chip will be no more than this value.

dB when connected with a 50 Ω line. These numbers indicated mismatch loss will be a small concern when switching substrates.

3.5 Compensating for small antenna area

THz and millimetre wave sources typically have low power outputs. Equation (2.72) shows that the received power at an antenna will include a factor of the wavelength, λ, squared. At these high frequencies, using a low power source will only mean a tiny amount of power can be received for detection. This can be remedied with the use of optical focusing. An off-axis parabolic mirror will take a plane wave (or parallel light) and focus it to a point, as seen in Figure 3.23.

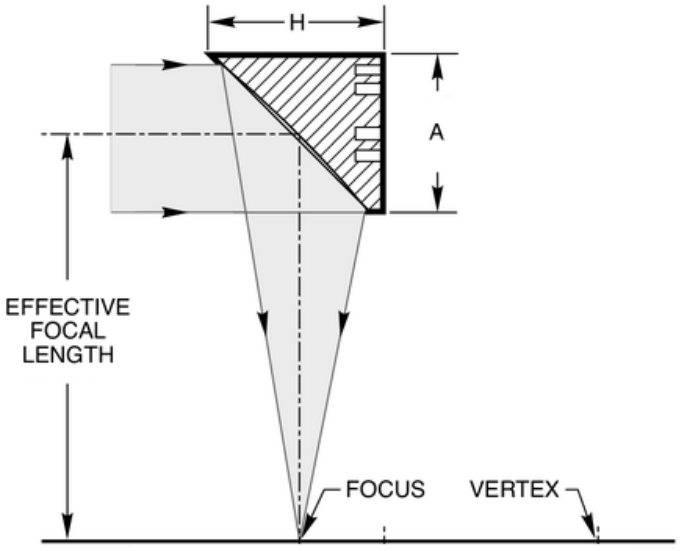

Figure 3.23: A 90°off-axis parabolic mirror diagram. The effective area focusing on the focal point is the apparent area of the mirror from the plane wave direction.

The power focused onto the antenna, if the HEB is placed at the mirror focal point, will be the area of the mirror seen by the plane wave. This increases

the effective area of antenna system, and thus increases the power received by the superconducting bridge.

3.6 Atmospheric attenuation

The atmosphere will attenuate millimetre wave and THz radiation, especially at the resonant frequencies of certain molecules. This is what allows these frequencies to be used to identify materials. It also means there can be difficulty transmitting information over long distances. Figure 3.24 shows the attenuation in the atmosphere, up to 400 GHz. Oxygen gas molecules will attentuate a 60 GHz electromagnetic planewave at a rate of about 15 dB/km. Between 350 GHz and 400 GHz, there is no resonance with the atmosphere, but there is still a general attenuation of 8 dB/km. At a distance of 2 m, the attentuation due to the atmosphere will be approximately 0.03 dB at 60 GHz and 0.016 dB at 400 GHz (at sea level).

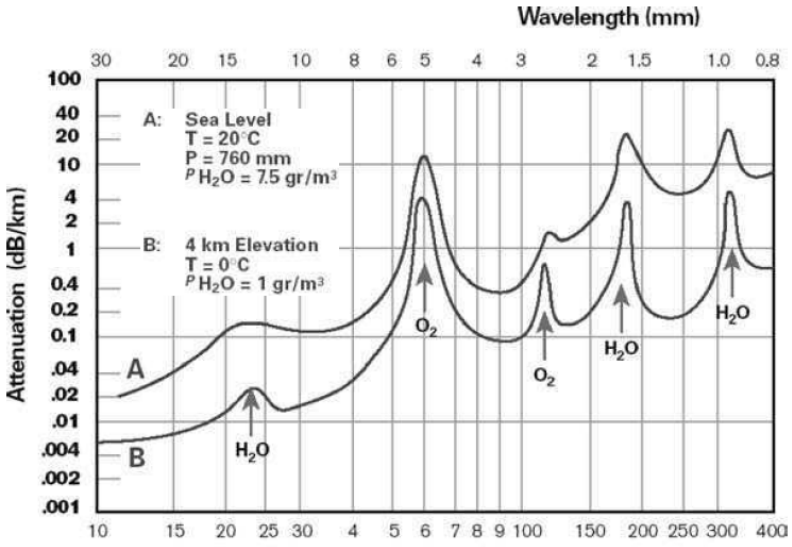

Figure 3.24: Attenuation of electromagnetic radiation in the atmosphere. The bottom scale (frequency) contains errors, so only the wavelength at the top should be referenced. Taken from [43].

Chapter 4

Superconducting bridge simulations

The performance of the microbridge is modelled as outlined in Chapter 2. The power received from the antennas is determined, and this power, along with any DC biasing, will increase the temperature of the electrons in the microbridge. These hot electrons can give rise to a voltage across the bridge. The change in voltage with changing input power is a measure of how sensitive the system is to simulus.

4.1 Input power

Using the gain of an antenna, where the input port is at the location of the microbridge, the anticipated input power from a radiation source can be determined. This power can be used with the heat balance equations in Chapter 2 to predict the electron temperature response to the stimulus.

Using (2.72) and a parabolic mirror to define the receiving antenna area, the power at the superconducting bridge, in terms of the surface power density P_{th} from a thermal source can be estimated. This is

$$P_B \approx A_{sys}\epsilon_{ant}A_{aperture}P_{th} \tag{4.1}$$

with the assumption that the signal is captured by a parabolic mirror just after the aperture and refocused onto the sensor after passing through an interfer-

ometer system as seen in Figure 2.9. From (2.68), with a resolution of 2 GHz, the radius is 1.8 cm. Edmund Optics supplies 90°off-axis parabolic mirrors with 25.4 mm, 50.8 mm, or 76.2 mm radius. The latter two are sufficient for an aperture with a diameter of 36 mm, as defined above. Placing a mirror just after the aperture can capture and collimate the thermal radiation and prevent further lowering of the surface power density. If the mirror refocusing the radiation into bridge has a smaller area than the aperture, P_B is corrected by the fraction of the two areas, $A_{mirror}/A_{aperture}$.

A perfect beam splitter would reduce the power to the sensor by one half. More specifically, it should reflect and transmit 50% of a plane wave that impinges on its surface. Combining two signals, one reflecting off the bean splitter and one transmitted through it, the resultant signal should have half the power of the original signal. For high-density polyethylene, the transmission-to-reflection ratio is 0.9 to 0.1, meaning $0.18P_{th}$ passing through the interferometer system[1]. For a 5 mm thick high resistivity Si wafer, the transmission-to-reflection ratio is 0.55 to 0.45, which would have $0.495P_{th}$ passing through the beam splitter.

Assuming 100 nW of power passing through an aperture of 1.8 cm that is 1 m from a thermal source, as calculated in Chapter 2, the amount of power received at the superconducting bridge for the twin slot antennas on Si will be $P_B = 100 \times 0.18 \times 0.98 \times 0.71 = 12.5$ nW. This is for the case of a high density polyethylene beam splitter. The factor 0.71 is for the smaller area (relative to the Jacquinot aperture) of a mirror at the cryocooler input. With mirror reflectance efficiency and atmospheric and window attenuation this value is lower, but higher than 10 nW. For the twin slot on MgO, the amount of power to the superconducting bridge will be 7.5 nW, when using a HDPE beam splitter. If the high resistivity silicon beam splitter is used, the power increases to 34 nW and 21 nW for the Si and MgO cases, respectively.

A thermal source, as predicted by Planck's equation, will not output enough power to be useful with antennas designed for frequencies about 60 GHz. If most of the radiation from a 10 cm long SiC rod is focused onto the sensor with reflective backing, the maximum power to the sensor will only be about 85 nW. This is on the order of the collimated power through the Jacquinot stop

[1]All mirrors are assumed to reflect 99% of the incident radiation.

from 350 GHz to 400 GHz. The small power from the thermal source, while it cannot be used for interferometry, is large enough to produce a measurable voltage response. This is described below. Also, for the twin slot antennas, an uncollimated thermal source can be brought closer to the sensor to increase the received power. This will, again, cause a measurable voltage change for a given input power.

Greater signal power can be generated from quantum cascade laser systems or backward wave oscillators (BWOs). In the case of the BWO, signal power can be up to 20 mW under 100 GHz, and 2 mW at 350 GHz to 500 GHz, in as little as 1 MHz to 10 MHz spectral line width. This power is power directed in a narrow beam, and not spread isotropically. The use of these devices can ensure a wider range of input powers are available. The cost of BWOs was too prohibitive for their use in this project. Quantum cascade lasers are not, as of the writing of this, commercially available.

4.2 Diffusion-cooled HEB

Some performance properties of diffusion-cooled HEB can be obtained from the temperature profile response from input power. Using (2.50) this temperature can be estimated for the input powers given above. The introduction of a DC current bias is also investigated. P_{diff} is estimated using Newton's law of cooling, (2.44). The parameter k is taken as the specific heat of electrons, c_e, divided by the time constant τ_{diff}. The specific heat can be estimated by $c_e = \gamma T_e$ for a device with electron temperature T_e. where the parameter γ is taken as as 1.85×10^{-4} Jcm^{-3}K^{-2} [9].

With the two ends of the one dimensional bridge fixed at the bath temperature of an estimated 3 K, the problem is a second order boundary value problem. This was solved numberically in Matlab using a variable step fourth-order Runge-Kutta method. The Second order differential equation was converted to two first order differential equations. Two initial values, $T_e(0)$ and $U(0) = dT_e(0)/dx$ are needed to initiate a solution. The first is known, and the second is found by way of an iterative shooting method. The algorithm is found in Appendix A.

4.2.1 RF with no biasing

In the case of a single high frequency signal constantly applied to the bridge, it is assumed that $1/\tau_{diff} << \nu_{RF}$ and the thermal distribution of the electrons does not oscillate with the signal. The electron temperature distribution is held unchanging in the absence of two or more frequencies mixing, assuming $\nu_{IF} < 1/\tau_{diff}$. Bridges of four lengths were investigated: 1 μm, 2 μm, 5 μm, 10 μm. In only the 1 μm case is it assumed that diffusion cooling may dominate over phonon cooling. This is determined from (2.43), where τ_{diff} is taken as 0.625 ns.

It is assumed that the ends of the bridge are held at 3 K[2] and that there is good thermal conductivity between the bridge and the cold finger so that the temperature of the bridge follows that of the cold finger. The temperature profile can be seen in Figure 4.1 with several input powers. The smallest power input, 7.5 nW produces a maximum temperature change of about 0.1 K at the centre of the bridge.

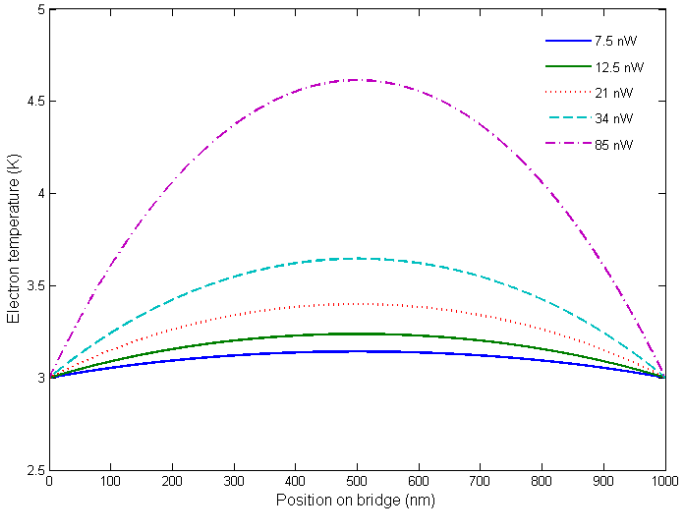

Figure 4.1: The simulated electron temperature profile across a 1 μm niobium bridge. Each curve represents a different input power.

[2]Near the lowest temperature possible on the cold finger, measured as $2.6K$, of the Cryomech cryocooler at Stellenbosch Univeristy.

4.2.2 RF with biasing

The superconducting transition temperature of a material and the critical current density (or current in the case of a specific area) are intimately linked. J_c increases as temperature, T, is lowered from T_c. If a current bias is passed through a device, the critical temperature is effectively lowered. Empirically, the relation can be expressed as

$$\frac{I}{I_c} = \left(1 - \frac{T_c(I)}{T_c(0)}\right)^{\gamma} \tag{4.2}$$

where γ is often about 0.5 [9]. In practice, the T_c versus I_c relation should be taken based on measurement, as with the resistivity curve at T_c. It is assumed for these calculations that the T_c of niobium thin films is 6 K when the cross sectional area is 5×1000 nm^2 or 10×1000 nm^2. This is a typical value for a thin film [22]. It is assumed constant with a changing current bias less than 100 μA, due to the relative small effect the I/I_c value[3] will have on T_c.

The resistivity of a superconductor can be modeled for $T < T_c$, and the contribution of DC biasing to the heating of the bridge can be estimated. If the temperatures of the electrons, T_e, are known along the bridge, the resistivity of a bridge follows

$$\rho(T_e) = \frac{\rho_N}{1 - e^{-\frac{T_e - T_c}{\Delta T}}} \tag{4.3}$$

at a single point, from the normal state resistivity, ρ_N, to zero. This model uses a transition width factor, ΔT, which determines how broad the curve is as it transitions to the superconducting state. Again, T_c is taken as constant. For increased accuracy, ρ should be taken as a function of both the electron temperature and the bias current.

With a bias of 300 μA, the temperature profile of the electrons in the bridge for RF input power around 12.5 nW is shown in Figure 4.2. When compared to Figure 4.1, a difference in the temperature profile for 12.5 nW can be seen. When the bridge is unbiased, the maximum electron temperature is predicted to be about 0.1 K above the bath temperature of 3 K. With the 300 μA of bias, the maximum electron temperature in the bridge increases to 0.44 K

[3]The critical current, I_c should be 650 μA to 700 μA for Nb of a 5×1000 nm^2 cross sectional area.

above the bath temperature. Two further 0.5 nW increases in power see the temperature increase to 0.48 K and 0.55 K above the bath temperature. The rate of temperature increase per unit power appears to increase, suggesting that more and more of the current is represented by normal electrons.

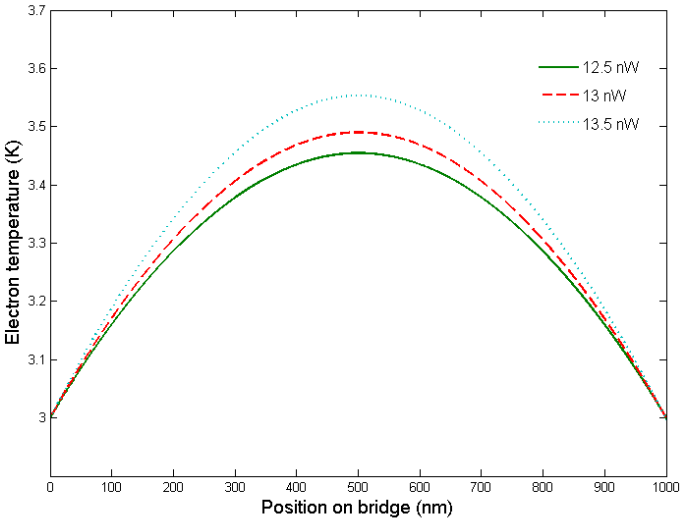

Figure 4.2: The simulated temperature distribution of the superconducting bridge with a bias current of 300 μA.

4.2.3 Voltage responsivity

Using (2.49) and (4.3), along with the electron temperature distribution found from solving (2.50), the voltage across the bridge for a given input power can be determined. dV/dP, an estimate of the DC voltage responsivity, can be found by varying the input power.

In the case above of the twin slot antenna delivering 12.5 nW of power to the superconducting bridge, using the resistivity curve with a transition width of 0.2 K, an estimated voltage across the bridge is 14 μV. This assumes the transition temperature is correct, and the appropriate transition curve of the resistivity value is also correct. These are easily obtainable from experiment, and the model adapted accordingly. A DC change of 14 μV should be easily measurable with instrumentation amplifiers.

Table 4-I: Simulated voltage responsivity with a current bias.

P_{RF} (nW)	Voltage (μV)	Resistance (Ω)
200	3.2	0.10
250	73.4	1.45
251	77.0	1.54
252	81.0	1.62
253	85.0	1.70
254	89.3	1.78
255	93.6	1.87
256	98.1	1.96
257	102.7	2.05
258	107.6	2.15
259	112.4	2.25
260	117.4	2.35
261	122.6	2.45
262	128.4	2.57

The simulated voltage and resistance across a diffusion-cooled bolometer of dimensions 1 μm by 1 μm by 5 nm, biased with 50 μA, is seen in Table 4-I. The total bridge resistance is estimated to be close to 15 Ω, and the values above show that the bridge length in the normal conducting region is small compared to the total length of the bridge.

4.3 Phonon-cooled HEB

The temperature of the electrons can be solved from (2.47) and (2.48). Simplifying assumptions where $T_B = T_p$ and $k_e = k_e(T_c/2)$ were applied to decouple the two equations, as in [17]. The equation for electron temperature then becomes

$$k_e \frac{d^2 T_e}{dx^2} + J^2 \rho(T_e) + P_{RF} - \frac{c_e}{\tau_{e-p}}(T_e - T_B) = 0 \tag{4.4}$$

again with $c_e = \gamma T_e$.

For niobium bridges longer than 1 μm, the cooling mechanism is assumed to be phonon-cooling, with $\tau_{e-p} = 1ns$. YBCO bridges on MgO are also assumed to be of the phonon-cooled type. It has been reported [47] that $\tau_{e-p} = 1.5$

ps for this material. However, YBCO requires a larger device volume than is possible with niobium due to the complex YBCO crystal structure and its size. While a Nb bridge can be made 5 nm thick, YBCO films thinner than 100 nm showed no superconductivity. This will mean that an YBCO HEB will require a larger high frequency power source.

4.3.1 RF with no biasing

The temperature profiles at various RF power inputs are simulated as above. The boundaries are held at 3 K for the niobium bridge, and at 77 K for an YBCO bridge in liquid nitrogen.

The thermal profile in a 2 μm long and 1 μm wide YBCO bridge was simulated for 100 nW, 1 μW and 10 μW input powers. The volume of this bridge is substantially larger than with Nb bridges, due to the 100 nm film thickness. The thermal response is seen in Figure 4.3. According to the simulation, the electron temperature will vary by only a few millikelvin when stimulated with 100 nW of input power. At 10 μW, this is predicted to increase to 0.5 K.

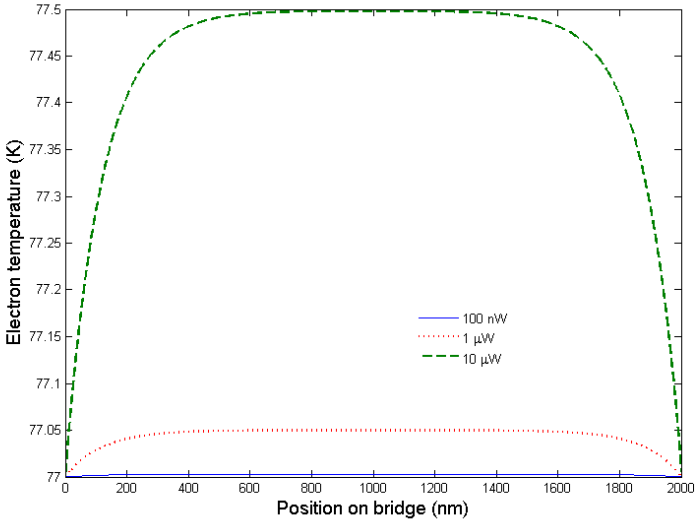

Figure 4.3: The simulated thermal profile along a YBCO superconducting bridge with no DC biasing.

4.3.2 RF with biasing

The effect of biasing is handled just as it is in the case of diffusion cooling. YBCO bridges are also simulated but the wide variation of sample resistivity and T_c make predictions troublesome. Simulations at the extremes of these parameters will give an expectation of the performance.

With a current bias of 50 μA, the temperature of electrons varying across a phonon-cooled Nb bridge with a length of 2 μm (width of 1 μm and thickness of 5 nm) is seen in Figure 4.4. The input RF power is greater than that expected from a thermal source, but is a typical value for local oscillator input powers used with these types of bolometer mixers.

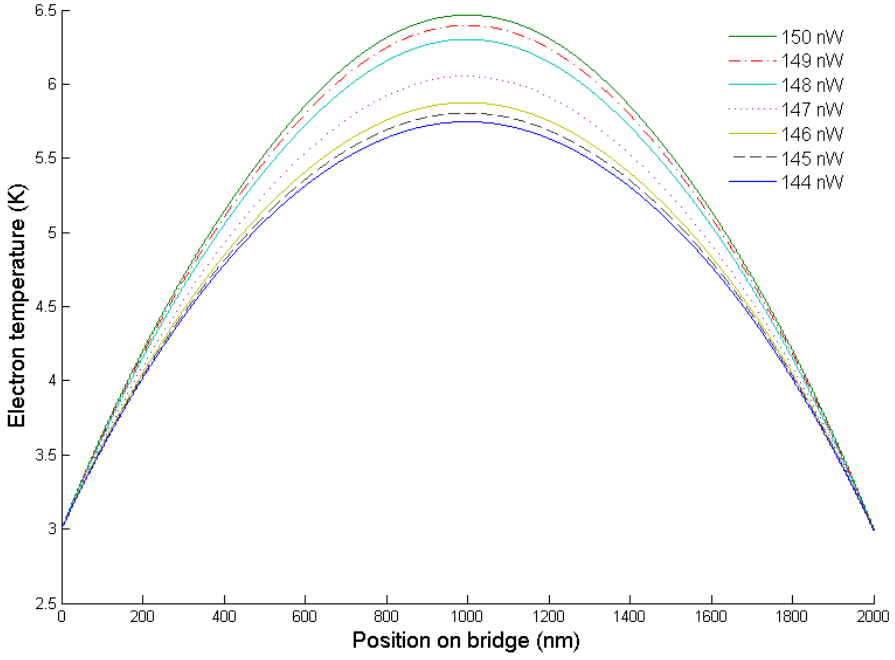

Figure 4.4: The simulated electron temperature across a current biased phonon-cooled Nb bridge varying with RF input power of 144 nW to 150 nW.

Under lower RF power but with a higher current bias of 300 μA the temperature profile becomes as seen in Figure 4.5. With only an RF power increase from 11 nW to 12 nW, the predicted peak temperature increases by about 0.1

K. The large current bias saturates the bridge closer to the transition to the normal state.

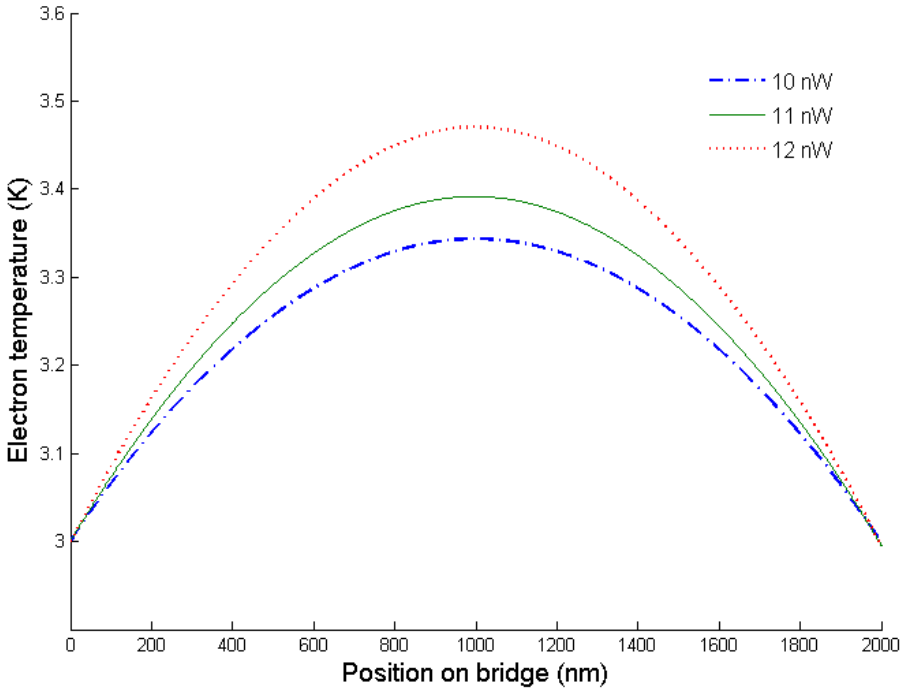

Figure 4.5: The simulated electron temperature across a current biased phonon-cooled Nb bridge varying with RF input power of 10 nW to 12 nW.

The simulation was also performed with a 1 μm long and 1 μm width YBCO bridge. The 100 nm thick bridge was biased with 138 μA of current and subjected to 10 μW to 10.4 μW of RF power, in steps of 100 nW. The temperature profile of the electrons across the bridge is seen in Figure 4.6. The large volume of the device prevents a large change in electron temperature, in constrast to the thinner niobium held at a much lower temperature.

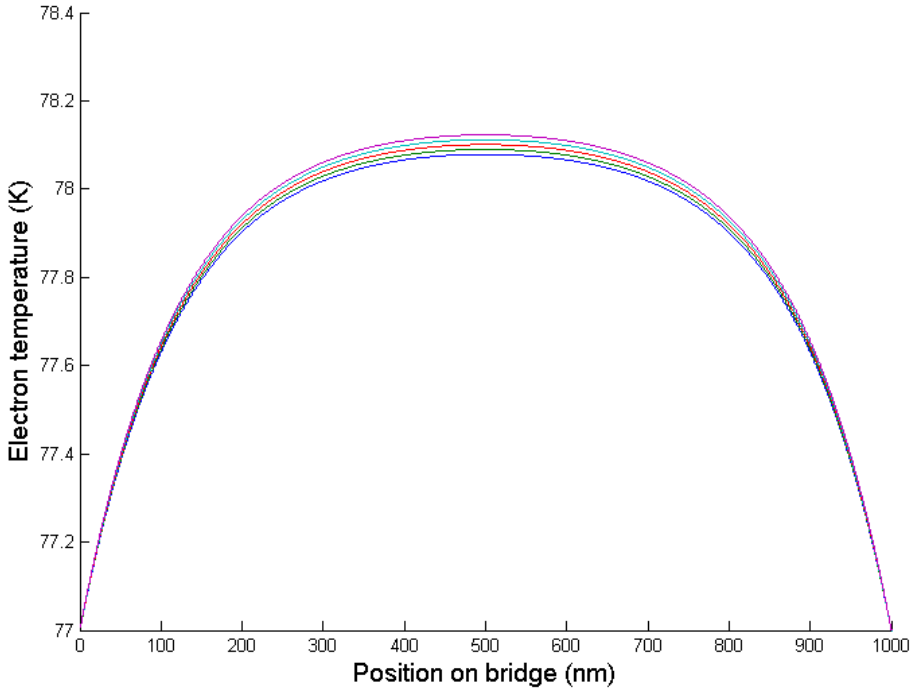

Figure 4.6: The simulated electron temperature profile across a current biased YBCO bridge. The RF input power was varied from 10 μW to 10.4 μW.

4.3.3 Voltage responsivity

As with the diffusion-cooled case, the voltage across the bridge can be estimated from the simulated electron temperature distribution along with (2.49) and (4.3). Outlined in Table 4-II is the voltage response of a Nb HEB biased with a current of 50 μA. The P_{RF} values are larger than those outlined from a SiC thermal source, which signifies that a larger bias current is required for similar voltage output at smaller P_{RF} values.

The simulated voltage levels are based on the assumption that the resistivity at T_e is known. Equation (4.3) can be adapted to fit the curve of most superconductors, provided there is a clean transition to zero resistivity. DC biasing, thermal power source levels, and local oscillator power levels can be adapted to suit the material properties of a specific film.

The same calculations were performed for a current biased YBCO bridge. Table 4-III shows the voltage response and bridge resistance of a 2 μm long

Table 4-II: Simulated voltage responsivity of a Nb HEB (with a current bias).

P_{RF} (nW)	Voltage (mV)	$\Delta V/\Delta P$ (μV/nW)
160	0.9102	
159	0.9046	5.6
158	0.8990	5.6
157	0.8930	6
156	0.8870	6
150	0.5240	60.5
149	0.4850	39
148	0.4294	55.6
147	0.2698	159.6
146	0.1653	104.5
145	0.1302	35.1
144	0.1054	24.8

bridge.

Table 4-III: Simulated voltage responsivity of an YBCO bridge with a current bias.

P_{RF} (μW)	Voltage (μV)	Resistance (Ω)
10	601.0	4.37
10.1	619.7	4.50
10.2	638.4	4.64
10.3	657.2	4.77
10.4	676.3	4.91

4.4 Conversion loss

The loss associated with signal mixing and IF generation is a useful predictor of HEB mixer performance. An estimate of the conversion loss, L_{mix} is taken from [50]. It uses the small changes in bridge resistance to changes to DC and RF input power. If the bridge is held at a bias resistance of R_{B0} then the

resistance due to changes in input power, Δ_{RF} and ΔP_{DC}, is

$$R_B = R_{B0} + \xi_{RF} \cdot \Delta P_{RF} + \xi_{DC} \cdot \Delta P_{DC} \tag{4.5}$$

with $\xi_{RF} \approx \Delta R/\Delta P_{RF}(1 - \xi_{DC} I^2)$ and $\xi_{DC} \approx \Delta R/\Delta P_{DC}$ representing the change in resistance due to a change in RF and DC power.

The conversion loss is also affected by the electrothermal feedback of the system. This is estimated from

$$\chi = \frac{1}{1 - \xi_{DC} I^2 \frac{R_L - R_B}{R_L R_B}} \tag{4.6}$$

for a load resistance of R_L. Finally, the conversion loss is found from

$$L_{mix} = \frac{R_{B0} \left(R_L + R_{B0}\right)^2}{2 R_L P_{RF} P_{DC} \chi^2 \xi_{RF}^2}. \tag{4.7}$$

Using the values for the voltage responsivity given above in Table 4-II, the conversion loss is estimated to be about 10.0 dB for a bias current of 50 μA. This estimate comes from the parameters $R_{B0} = 7.0\ \Omega$, $R_B = 9.9\ \Omega$, $\xi_{RF} = 181.9 \times 10^6\ \Omega/W$, $\chi = 2.7$, across a load resistance of 50 Ω. This estimate of the conversion loss is close to other simulated estimates for phonon-cooled HEBs, such as in [51].

A diffusion-cooled HEB mixer, with the voltages and resistance values shown in Table 4-I, biased with 50 μA of current is estimated to have a conversion gain of 11.9 dB.

The estimated mixing conversion loss based on this response is 44.8 dB. This is found from the parameter values $\xi_{DC} = 2.00 \times 10^6\ \Omega/W$, $\xi_{RF} = 1.29 \times 10^6\ \Omega/W$ and $\chi = 1.03$. This value of conversion gain for an YBCO bridge is within experimentally determined values. 77 dB loss was reported by [52], at 0.3 mW of LO absorbed RF power. 35 dB loss was reported by [47], with about 1 μW of LO input power to a film of 100 nm thickness. The obvious area for improvement is the thickness of the YBCO film. The conversion loss can be decreased with thinner YBCO film, provided the film retains superconductive properties.

4.5 Effect of cryocooler temperature fluxuations

If the bolometer is not held at a fixed temperature, clearly the drifting will affect the device performance. A cryocooler that has a drift of 10 mK (likely oscillating at the frequency of the cooling cycle of the cryocooler) and a transition width from normal conduction to superconduction of 0.5 K will see a periodic change in voltage across the bridge. The device must be biased in such a way for this temperature variation to not saturate[4] the bridge when RF power is applied.

This temperature fluxuation can be modeled by changing the bath temperature between a minimum and a maximum. If the device functions at both extremes, the biasing and input power are acceptable for use in the cryocooler environment. Figure 4.7 shows the change in electron temperature profile for a phonon-cooled bridge with a change in boundary temperature. The input RF power and DC bias are fixed at 140 nW and 50 μA, and the boundary bath temperature varied by 0.15 K. The signal voltage changes from 23.7 μV at 2.85 K to 59.2 μV at 3 K.

While the nonlinearity of the variation in resistance of a superconductor, with respect to temperature and input current, makes separation of the effect of cryocooler temperature fluxuation from the desired signal output a nontrivial matter, compensating for this effect is possible. If the total power input of P_{RF} and P_{DC} do not saturate the device at either extreme of the boundary temperature, the bolometer remains sensitive to power changes in the desired signal. Modeling the expected influence the boundary temperature will have on the measured data and attempting to correct for the effect may be possible, provided the input RF power is known with time.

The change in voltage difference, V_{corr}, between the high boundary temperature and low boundary temperature, V_{high} and V_{low}, if linearized and assumed

[4]For the bridge to be saturated is for it to have transitioned completely into the normal state at a power input magnitude less than the RF input power. A bolometer in the normal state will have a greatly reduced sensitivity.

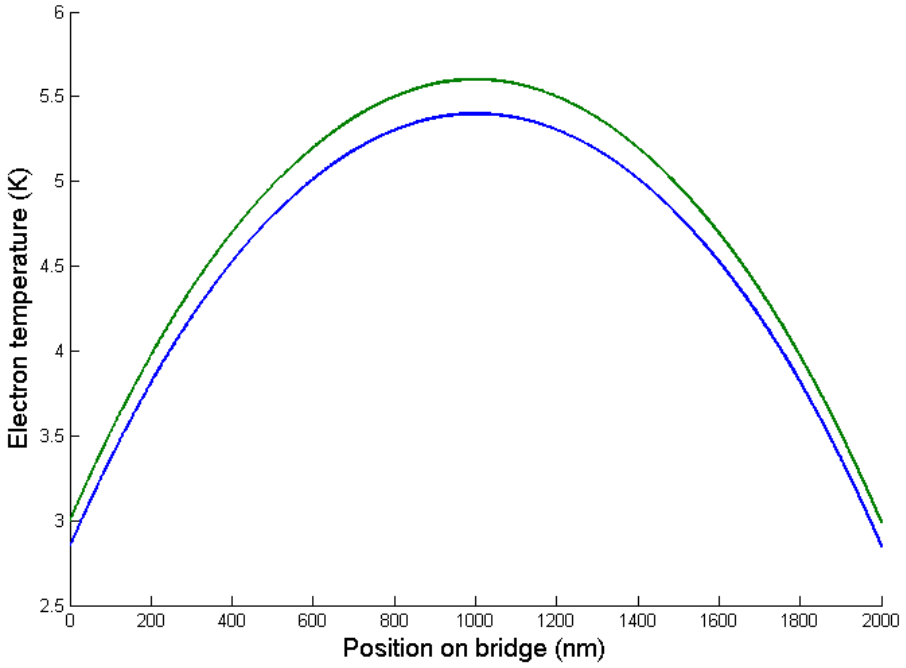

Figure 4.7: A comparison on the effect of boundary termperature on the electron temperature profile in an HEB.

sinudoidal, can be estimated at a specific RF power as

$$\begin{aligned} V_{corr}(P_{RF},t) \;\approx\; & \frac{dV_{low}}{dP_{RF}}(P_{RF})\Delta P_{RF} \\ & + \left(\frac{dV_{high}}{dP_{RF}}(P_{RF})\Delta P_{RF} - \frac{dV_{low}}{dP_{RF}}(P_{RF})\Delta P_{RF}\right) \\ & \times \left(\frac{1}{2} + \frac{1}{2}\cos(2\pi\nu_p t + \varphi)\right) \end{aligned} \tag{4.8}$$

with the cryocooler pump frequency, f_p and phase, φ. When mixing a signal that varies in an unknown manner with the local oscillator, determining, or using self-interference in a interferometer with an unknown spectral distribution, P_{RF} may remain unknown. This will lead non-unique solutions to what may be the true corrected voltage value.

A simpler method is to only measure (or to only analyze measurements) in a time span in which the temperature variation of the boundary is small

enough to produce a negligible change in the signal voltage. The frequency of the cryocooler temperature change has a time constant that is much greater than the time constants that govern bolometer reactions, meaning, without hysterisis, the variation of cryocooler temperature will have a negligible effect on utilized measurements.

This approach may increase data collection time, especially in the case of Fourier transform spectroscopy. The reason for which is explored in the next chapter. If possible, use of a cryocooler with large cold finger temperature variations should be avoided.

Chapter 5

System design

Depending on the operation of the HEB, a different device system is needed. This section outlines the parts needed for operation. There are some common components used in both an HEB interferometer and an HEB mixer. These are presented first, and the overall sytem utilizing these parts is presented afterwards, depending on system type.

5.1 Common components

Both the interferometer and the mixer systems operate in a quasi-optical manner. The devices operate on two different scales, first on scales much larger than the RF wavelength (denoted by the antenna centre frequency, ν_c), then on scales on the order of the RF wavelength. In the first case, optical analysis is dominant. Lenses and mirrors are used to guide and focus the desired radiaion to the antenna. Once the radiated power reaches the antenna, the structures are on a scale closer in size to c/ν_c or v_m/ν_c (where v_m is the speed of light in the substrate), so RF design techniques are applicable.

In both the mixer and interferometer modes of operation, 90° off-axis parabolic mirrors are used to collimate and focus the radiation. Edward Optics aluminium first-surface mirrors with focal length of 15.24 cm placed to collimate the signal towards the beam splitter and focus the signal onto the HEB. A mirror can be seen in Figure 5.1.

The window of the cryocooler was made from high-density polyethylene (HDPE). This material has a transmittance of a near constant 90% for signal

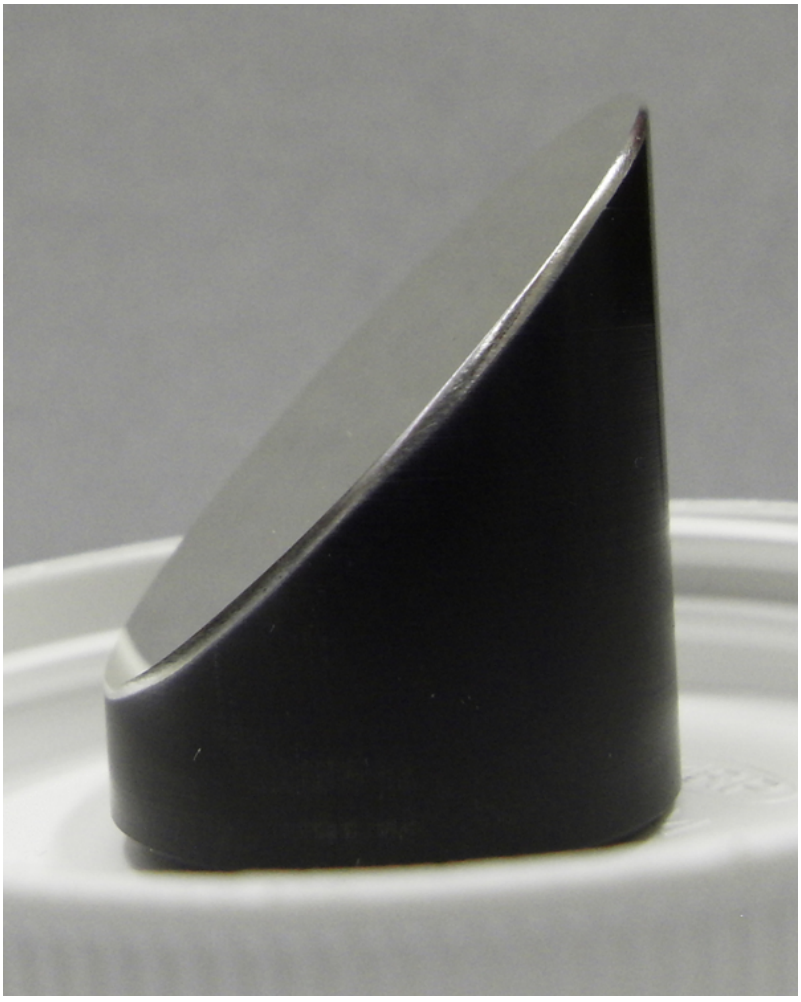

Figure 5.1: A 90°off-axis parabolic mirror.

wavelengths longer than 300 μm and this value is nearly constant with temperature [53]. The outer shell of the cryocooler housing has aluminium discs which are vacuum sealed with o-rings. One of these discs was replaced with a 5 mm thick disc of HDPE machined to the same radial dimensions. This gives a window of about 20 mm in diameter into the bottom of the cryocooler.

Magnetic shielding for the system, to cover the cryocooler cold finger and protect the superconductor from stray magnetic fields, was also created allowing a window into the test area. As both sides of the shield is contained in the cryocooler vacuum, no windowing material is required. The material of the shield has a large relative permeability μ_r that pulls in magnetic field lines,

leaving the centre of the cylinder, containing the cold finger and test chip, with a lower magnetic field intensity. With this in place, it was assumed that magnetic fields were a negligible influence on superconductor performance. Measurements were taken of the geomagnetic field, in terms of one vector normal to the Earth's surface and one parallel to the Earth's surface, around the cryocooler. The measurements show that the vectors are approximately -23 μT normal and 11 μT parallel to the Earth's surface. With the addition of magnetic shielding around the cold finger, the magnetic field inside is reduced to -1.6 μT normal to the Earth and 50 nT to 100 nT parallel.

Trapped magnetic flux can destroy the operation of Josephson junctions, which are devices that inherently use trapped magnetic flux to store information. Since superconductor-based HEBs do not use flux in their operation, only the possibility of suppressed superconductivity due to the presence of a static magnetic field is considered. According to [54], the critical current density in a 29 nm Nb thin film is maintained higher than 10^9 A/m^2 for magnetic fields as high as 0.6 T, in a 4.2 K liquid helium environment. These measurements were done on magnetic fields perpendicular to the chip, which provides the maximum suppression of superconducvtivity.

The test chip holder was also designed to allow firm contact to the cryocooler cold finger while leaving open space between the window into the cryocooler and the device surface. All prototype holders were machined from brass. Two brass plates clamp to the cold finger and are tightened with brass screws. A third brass block slides in and is supported by the two plate clamps. Onto this third brass plate is the test PCB and test chip. To increase thermal conductivity between the cold finger and the plates, Dow Corning silicon-based thermal paste is applied to connecting interfaces. The system with a mounted test sample is shown in Figure 5.2.

In order to lessen the amount of higher energy infrared radiation from entering the cryocooler chamber and potentially heating the bridge and causing noise, a low pass filter based upon a special porous silicon substrate material was used. The LPF-128-019 filter, from Lakeshore inc., is 128 μm thick. The filter can be seen in Figure 5.3

The filter performance is extrapolated from the data specifications that are provided by Lakeshore. The transmission data, measured to a maximum

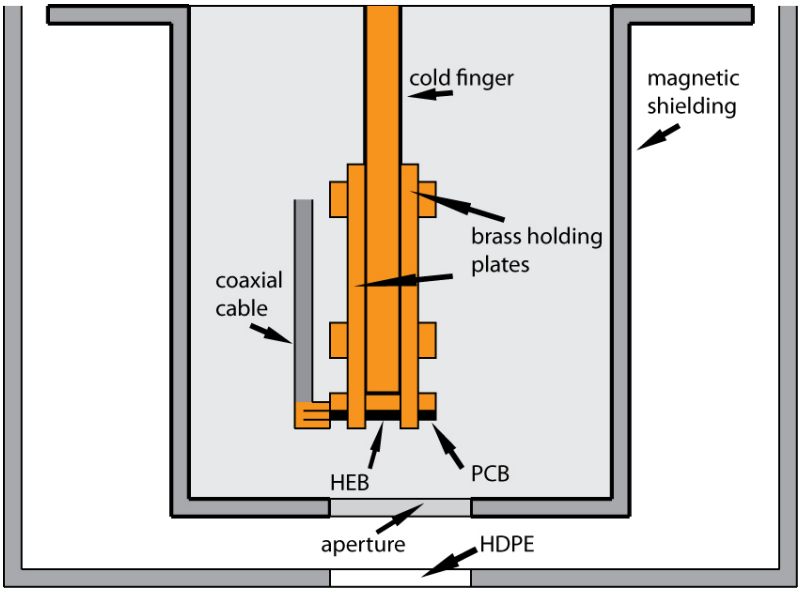

Figure 5.2: A cross sectional schematic of the cryocooler test area. The test chip is mounted on a PCB which is mounted onto a brass plate. This plate is held against the cold finger by two larger brass plates. The radiation enters the test chamber through the HDPE window and aperture in the magnetic shielding.

Figure 5.3: The infrared low pass optical filter in its plastic holder.

wavelength of 200 μm, is seen in Figure 5.4 is used to estmated the transmission loss at 380-400 GHz and 60 GHz.

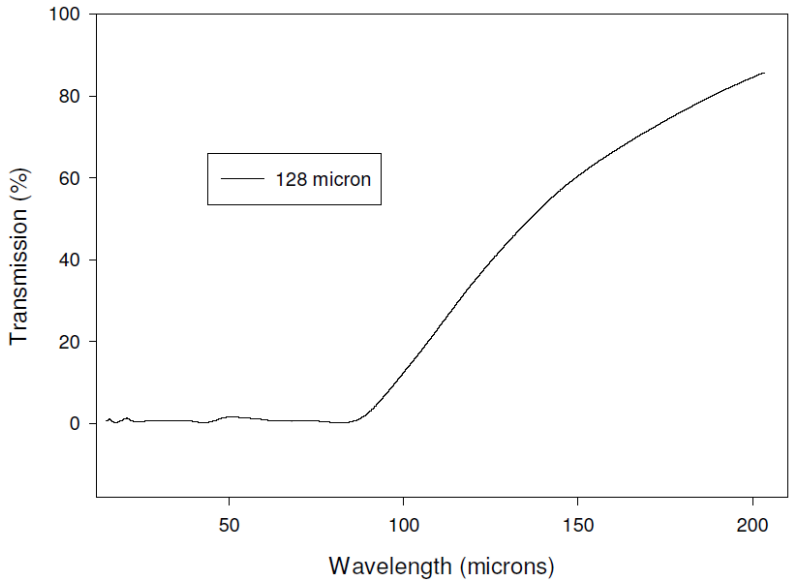

Figure 5.4: The transmission of the infrared filter versus the wavelength of the transmitted signal.

The bridge bias current source was provided by an LF351 J-FET operational amplifier with transistor and voltage regulator. The current source is tuned with a variable resistor. The resistor values chosen provide a DC current ranging from 30 μA to 1.4 mA. The circuit for the current source can be seen in Figure 5.5. The resistance R_1 was 560 Ω, and the potentiometer, R_V, varied from 0 Ω to 400 Ω.

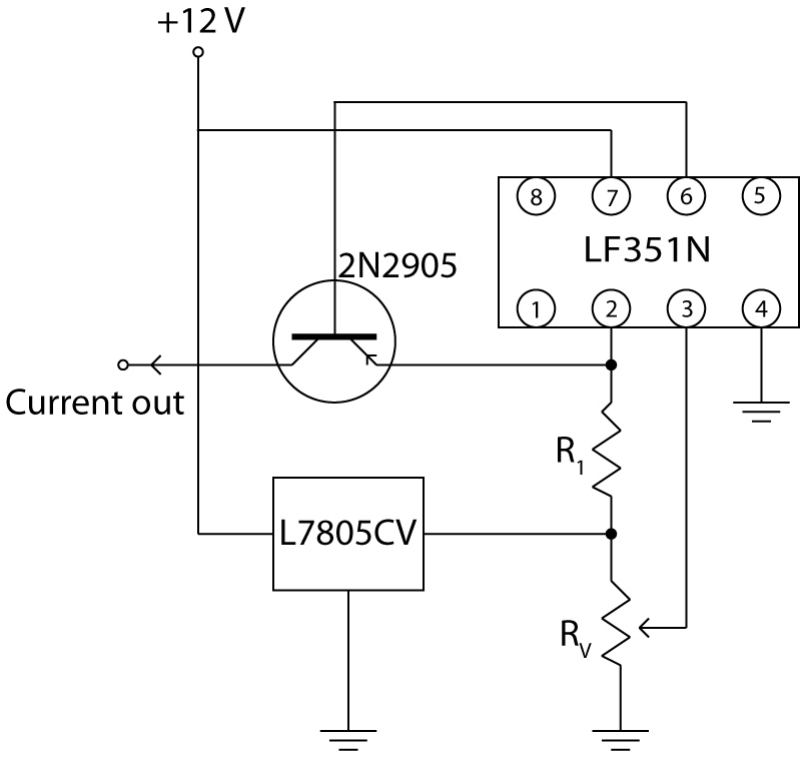

Figure 5.5: A current source circuit using an LF351 J-FET.

5.2 SMA to PCB connection

The IF connection off of the chip and PCB to the coaxial cable and the subsequent signal chain depends on the transition between the waveguide on the PCB and the SMA connector. If this connection is lossy at high GHz frequencies, another method must be found to allow the signal to pass from the HEB. A simulation of this system, in terms of a microstrip line and SMA connector, was performed in CST Microwave Studio. The simulation used 254 μm thick FR-4[1] and gold as the conductors. The lossy FR-4 had $\tan\delta = 0.025$, and assumed a constant fit from 0 GHz to 8 GHz. The model used in the simulation can be seen in Figure 5.6.

The results show that the transmission of frequencies is quite high over this spectrum. Up to 4 GHz, $S_{2,1}$ (from the PCB to the SMA connector) is

[1]In this project, the PCB substrate of choice was Rogers 3203 substrate. The thickness of the substrate is the same as the FR-4 simulated in this section. The $\tan\delta$ of RO3203 is 0.0016 according to the datasheet.

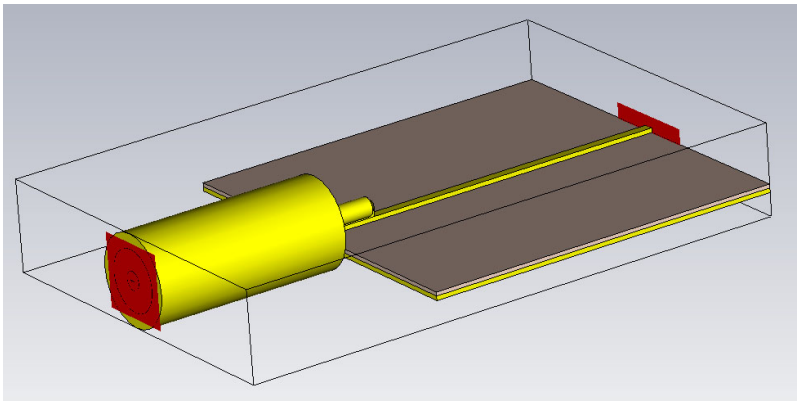

Figure 5.6: The model of the SMA connector and microstrip line.

above −0.2 dB (see Figure 5.7). The loss is predicted to still be under 0.5 dB at 8 GHz. Up to 4 GHz, $S_{1,1}$ remains about −19 dB then steadily climbs and remains below −12 dB at 8 GHz (see Figure 5.8).

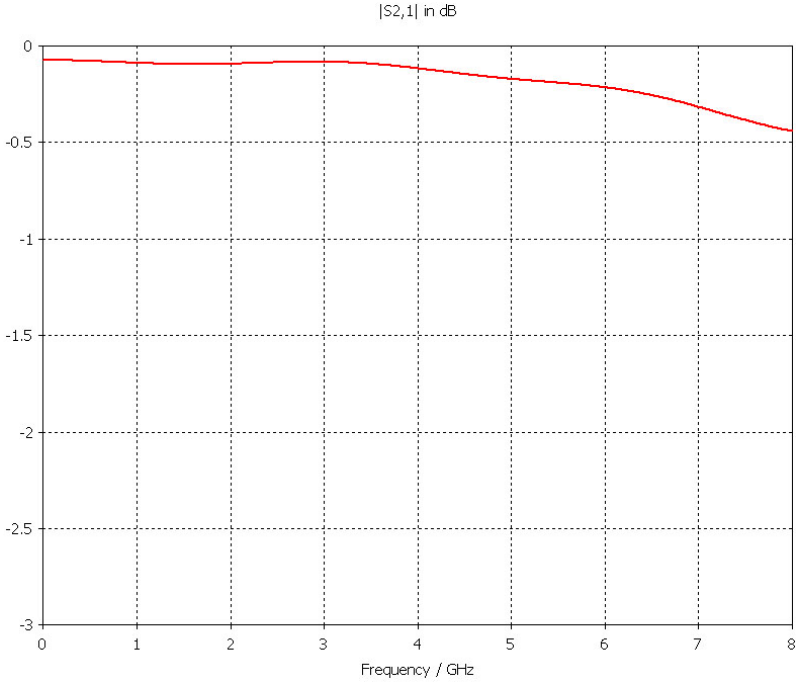

Figure 5.7: The simulated $S_{2,1}$ for a signal propagating along an FR4 PCB to an SMA connector.

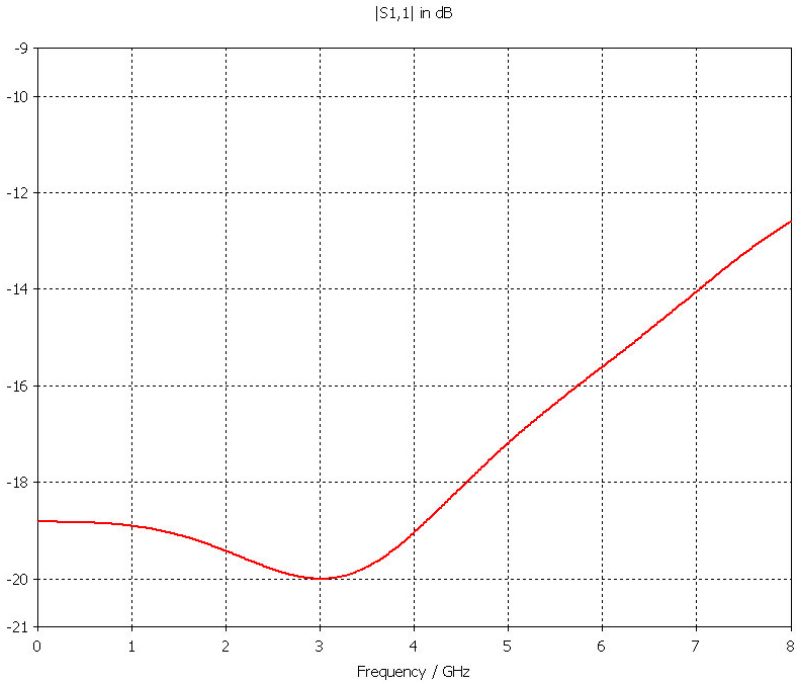

Figure 5.8: The simulated $S_{1,1}$ for a signal propagating along an FR4 PCB to an SMA connector.

5.3 HEB interferometer

To operate as an Fourier transform interferometer, the system needs an arrangement of mirrors as seen in Figure 2.9. The movable mirror can be attached to a motor controlled linear stage or a manually movable platform. The stepper motor or platform must move at intervals no more than that defined by (2.65). Even at 500 GHz, this interval is no more than approximately 300 μm, which is easily attained by commercial linear stages. Newmark Systems' NLS8 Series linear stages have a maximum positional resolution of 0.08 μm and a maximum span of 500 mm. The devices can travel at a maximum velocity of 40 mm/s. The accuracy and positional span is more than enough for the resolution of approximately 0.3 mm and retardation of 30 cm.

The signal can be measured in either at DC or at a frequency dependent on the velocity of the stepper motor. If using a platform that moves at velocity, v, the frequency that data must be collected is based on the largest wavenumber

being measured, $\tilde{\nu}_{max}$. This frequency is

$$\nu_{max} = 2v\tilde{\nu}_{max}. \tag{5.1}$$

With a velocity of 40 mm/s, the voltage must be sampled at a rate of at least 133.5 Hz.

The signal voltage will be, depending on input power and biasing, on the order of low μV to just under 1 mV, as simulated in Chapter 4. If the measurements are made at DC, and not while one mirror is moving, only a DC amplifier is needed. If the system utilizes a continuous scan with a movable platform, an amplifier capable of handing the data collection frequency must be used.

As seen in Chapter 4, the voltage that is formed across a bridge can vary from 0 to almost 1 mV under usual biasing conditions. Using a sensitive low-noise differential intrumentation amplifier is proposed when the bridge is used as an interferometer.

The basic system layout is seen in Figure 2.9.

The beam splitter used in the interferometer design was one that splits the signal beam (transmittance and reflectance) as evenly as possible. This was achieved with a high-resistivity silicon wafer, with a resistivity of greater than 20 kΩcm. The transmittance through the silicon is about 55% [53] for wavelengths longer than about 25 μm. In this same regime, the reflectance is about 45% [53]. This near even split allows the single thermal source power to destructively interfere with itself as completely as possible, depending on retardation length.

The thermal source is housed in a metallic structure with a reflective backing. The SiC rod is held between two copper connections, and these are electrically isolated from the housing at both ends with ceramics. The thermal source and housing are shown in Figure 5.9. The rod is powered with a Hewlett Packard 62745 DC power supply. 30 V and 15 A were fed through a rod to heat to a maximum of 1200 K.

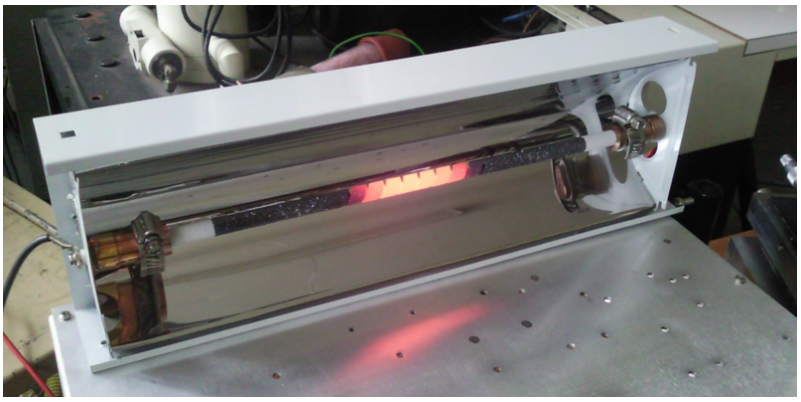

Figure 5.9: The SiC rod in its housing. The rod is seen heated to approximately 1000 K.

5.3.1 Interferometer signal chain

The fourier transform spectrometer is intended to measure the DC voltage change across a superconducting bridge. This differential signal is fed into an INA128P from Burr-Brown. This instrumentation amplifier offers a gain determined by an external resistance, R_G. The gain is then, $G_v = 1 - 50000/R_G$. The gain ranged from a gain of 0 dB for an infinite R_G, to a maximum of 40 dB for $R_G \approx 5\ \Omega$. An R_G of 50 was used for a voltage gain of about 30 dB.

The expected voltage levels would approach 1 V and vary by at least 100 mV, depending on retardation length. This voltage can easily be measured by any portable voltmeter

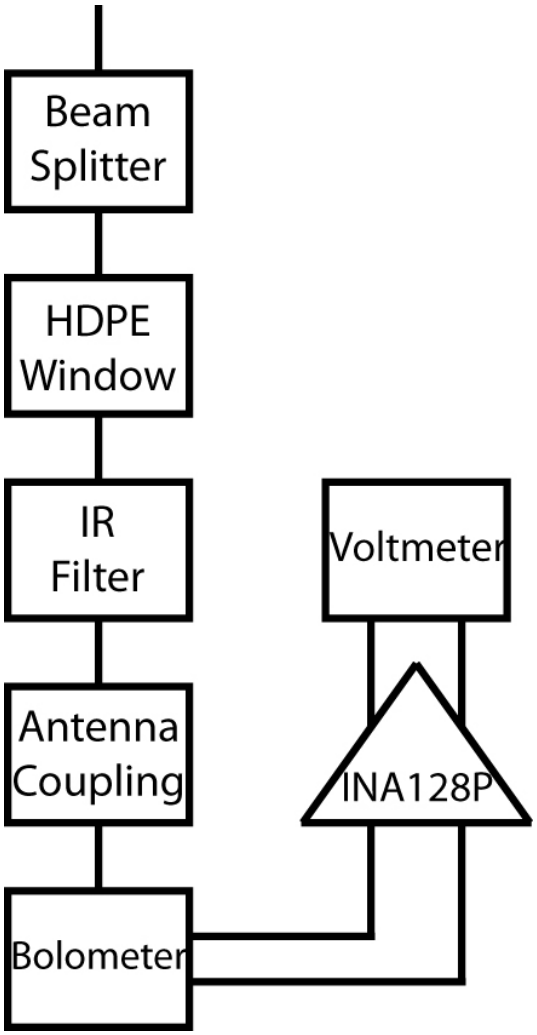

Figure 5.10: The signal chain for the interferometer system. The signal is a DC voltage measured across the bolometer stage.

5.4 HEB mixer

Operation as a mixer requires a local oscillator with as small a spectral line width as possible. The largest difference from the interferometer is the measured signal varies at the IF frequency. This ranges from an expected 150 MHz for phonon-cooled Nb mixers, to 5 or more GHz for YBCO phonon-cooled mixers[2].

Signal amplifiers need to span the IF bandwidth, have low noise levels and operate at cryogenic temperatures. For this purpose, high electron mobility transistor based low noise amplifiers were chosen for the first stage of amplification. The first amplifier in the chain is of prime importance, as a high gain and low noise amplifier in this position will have its contribution to the noise be dominant. Operation at 4 K and below is important, as the amplifier should be close to the HEB mixer due to RF propagation losses at the IF frequency.

From the experimentation in [1], HMC460, from Hittite Microwave Corp., continues operating at 4 K from DC to at least 6 GHz. The gain over the expected 150 MHz mixer bandwidth is about an average of 18 dB. The noise figure over this bandwidth is about 2 dB. At 300 K, the gain of the amplifier over this bandwidth decreases to about 17 dB. The gain of the amplifier from DC to 6 GHz is seen in Figure 5.11.

HDPE was chosen as the system beam splitter when the device is used as a mixer. The transmittance to reflectance ratio for HDPE for wavelengths longer than 300 μm is 9 to 1 [53]. Since local oscillator power can often be large and controlled compared to the measured signal of interest, allowing the local oscillator to reflect into the system allows more of the signal of interest to enter the system. For the signal of interest, the loss through this beam splitter will be about 0.5 dB.

A schematic of the optical system is seen in Figure 5.12. The signal to be mixed with the local oscillator is transmitted through the beam splitter.

[2]The theoretical maximum for YBCO mixers is over 100 GHz [47].

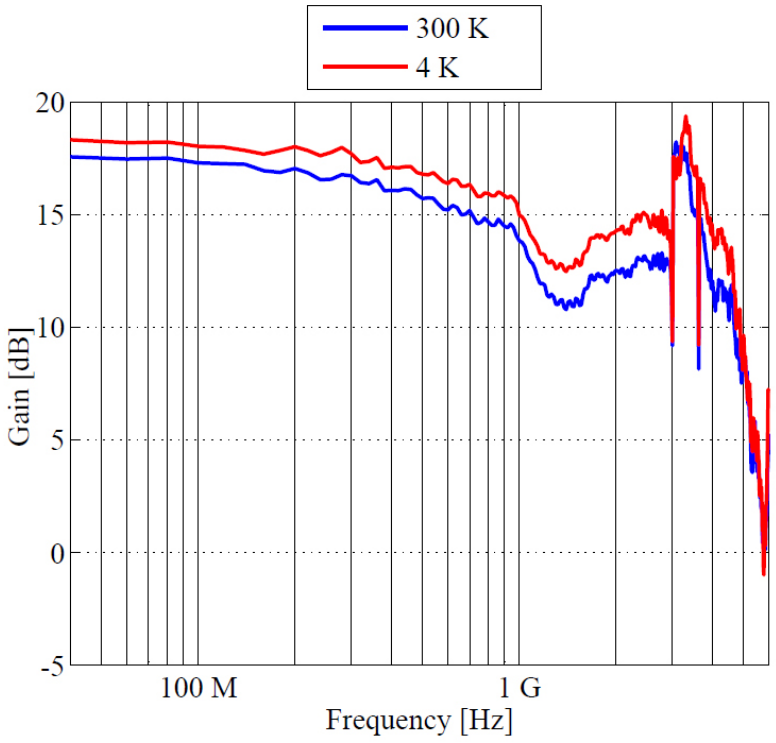

Figure 5.11: The gain bandwidth of the HMC460 measured at 300 K and 4 K. [1]

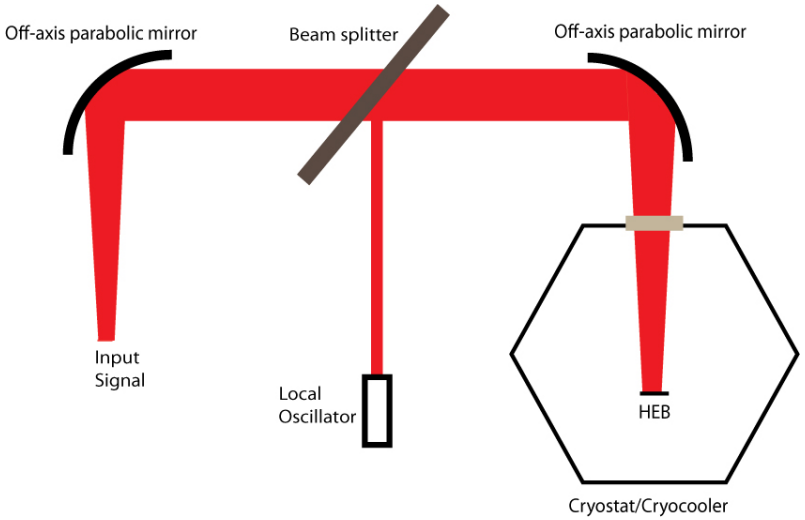

Figure 5.12: A schematic of a mixer system. The two signals, the one of interest, and the local oscillator, are combined at the beam splitter and directed into the cryogenic system.

5.4.1 Mixer signal chain

Each step in the system will either represent a gain or a loss in the signal strength. In particular, the signal mixing in the HEB will represent a large loss of 10 dB to 20 dB (using Nb), depending on the biasing conditions and local oscillator power.

Because of its low conversion gain and high local oscillator power requirements[3], the YBCO bridges were planned to be used in Fourier transform interferometer mode to test if any reponse can be observed for the low thermal powers from the SiC rod. There may be a problem with the model used to describe the heating of the electrons in the bridge. The anisotropic nature of YBCO is not incorporated into the model and may have a large effect on the temperature distribution and bridge resistivity.

The signal chain of the mixer system is seen in Figure 5.13. The system uses three HMC460 amplifiers, one at the bridge temperature and two at room temperature, for amplification. The gain just before the power meter is, for niobium based devices, between 25.3 and 35.7 dB, depending on the choice of beam splitter and antenna substrate. Further amplification can be added if required, though, for testing, the use of a Rohde & Schwarz FSH6[4] spectrum analyzer was planned. With a 140 nW (−38.5 dBm) input local oscillator power, the signal power at the spectrum analyzer reaches a predicted maximum of about 0.89 mW (−0.5 dBm) for a diffusion-cooled bridge and 1.4 mW (1.5 dBm) for a phonon-cooled niobium bridge. It is expected that such an IF signal power can be easily measured with this device.

The DC biasing and RF signals conduct through the bridge on the same metallic connection. A bias tee is placed just after the mixing stage in Figure 5.13, allowing DC current biasing and for the RF signal to propagate down the IF signal chain.

[3]YBCO mixer devices have been estimated to work at low nanowatt-level local oscillator powers [47], but the film thickness requirements to realise such a device are unobtainable with the current fabrication process at Stellenbosch University. YBCO films cease exhibiting superconductivity when much under 100 nm.

[4]The Rohde & Schwarz FSH6 is designed to analyze signals of frequencies between 100 kHz and 6 GHz.

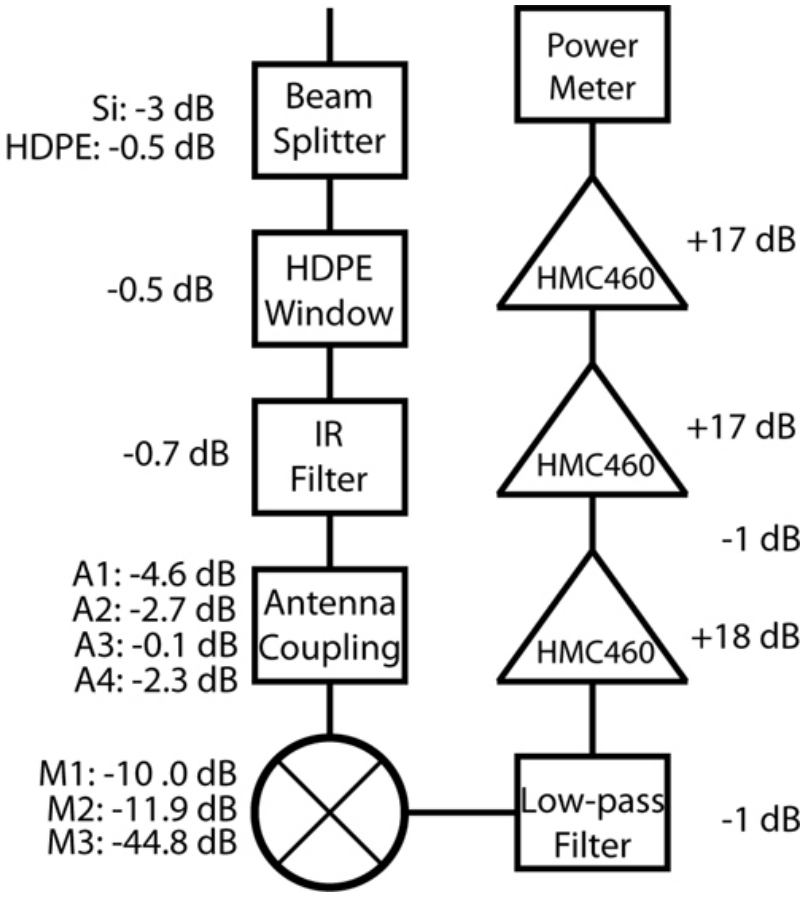

Figure 5.13: The signal chain, including instrument or line gain. After the bridge mixer stage, the signal is propagating at the IF frequency. A1: Si microstrip antenna. A2: MgO microstrip antenna. A3: Si twin slow antenna. A4: MgO twin slot antenna. M1: Phonon Nb bridge. M2: Diffusion Nb bridge. M3: Phonon YBCO bridge.

5.5 System noise

The noise temperature of a component is the temperature at which the thermal noise from a noisy resistor would generate the equivalent noise power, P_n, as measured from the device. This would be $T_n = P_n/(k_B B)$, with the Boltzmann constant, k_B and noise bandwith, B, if the device is operated in the limit where $h\nu << k_B T_n$. For high frequencies and low temperatures, a better estimate is

given by the Callen & Welton law,

$$P_n = k_B T_n B \left(\frac{\frac{h\nu}{k_B T_n}}{e^{\frac{h\nu}{k_B T_n}} - 1} \right) + \frac{h\nu B}{2} \tag{5.2}$$

which is the Planck law with a correction term [16].

For lossy passive optical components, the noise temperature is related to its physical temperature, $T_{physical}$, by its linear loss factor [16]. For a component with loss factor L, the noise temperature will be

$$T_n = (L-1)T_{physical}. \tag{5.3}$$

A chain of x of these components will produce a noise temperature, at the end of the chain, of

$$T_n = T_1 + \frac{T_2}{G_1} + \frac{T_3}{G_1 G_2} + \frac{T_4}{G_1 G_2 G_3} + \cdots + \frac{T_x}{G_1 G_2 G_3 \cdots G_{x-1}} \tag{5.4}$$

The IF portion of the mixer will have noise that is heavily influenced by the amplifier chain.

The receiver noise temperature and power are not simple values to measure. For a component, the power measured out of the device can be said to be $P_{out} = GP_{in} + P_{noise} = G(P_{in} + P_{eq})$. To measure the receiver noise temperature directly from one measurement, it would be required for the device to be attached to a matched load at 0 K. This is impossible, so the Y-factor method using two known input noise powers is used instead [18]. If one input is measured at room temperature (assumed to be 293 K), and another is measured at, say, 77 K. The output powers would be

$$P_{out,293} = GP_{in,293} + GP_{eq} \tag{5.5}$$

and

$$P_{out,77} = GP_{in,77} + GP_{eq}. \tag{5.6}$$

Defining the factor $Y = P_{out,293}/P_{out,77}$, the equivalent noise power of the receiver is found from

$$P_{eq} = \frac{P_{in,293} - YP_{in,77}}{Y-1} \tag{5.7}$$

Additionally, the conversion gain of the mixer, simulated in Chapter 4, can be calculated experimentally from $G_{mixer} = G_{sys} - G_{IF} - G_{optics}$. G_{IF} is the gain of the IF portion of the system, the right part of Figure 5.13. G_{optics} is the optical portion of the system, which is the left portion of Figure 5.13 before the mixer. The total gain of the system, G_{sys}, can be determined experimentally from [16]

$$G_{sys} = \frac{P_{IF,293} - P_{IF,77}}{k_B B(293 - 77)}. \tag{5.8}$$

This assumes two measured IF power outputs. One from a input signal at 293 K and another at 77 K. If other temperatures are used, the equation is easily adjusted.

5.6 Additional components

To improve system performance beyond what is outlined above, a few additional components are advisable for future implementation of HEB devices at Stellenbosch University.

The first, and perhaps the largest improvement would be gained from directing radiation incoming to the antenna and bridge by using a lense made of the substrate material. This is would improve performance of twin slot devices, or any other device that radiates into the substrate. The off-axis parabolic mirrors are assumed to focus onto the substrate and antenna. Tuning this focus may prove troublesome and an additional lense located at the substrate-air interface would increase the focus tolerance of the off-axis lense. Elliptical, hemispherical, or hyper-hemispherical lenses are typically used for this purpose [16] [9]. Such lenses are crafted with dimensions suitable to focus radiation at the antenna resonant frequency at a point located at or just beyond the substrate thickness.

An optical chopper wheel placed at the aperture of the thermal source can reduce noise gained from the optical equipment in the interferometer system. The portion of the measured voltage modulated at this chopping frequency will have originated from radiation from the chopped thermal source. Any measurement that is not modulated at this frequency is assumed to be noise added after the chopping (in addition to the bias power, which is also ignored).

Chapter 6

Manufacturing procedures

The process used to deposit the films and pattern them into the appropriate devices is outlined in this section. The designed structures were transferred to a chrome photolithography mask which was used to define the material layers in photolithographic processes.

The antennas and filters were drawn in an integrated circuit layout program. This single-layer file was given to a photolithography mask manufacturer, Martin Photomask. The minimum feature size of their process was 1 μm. The design layout is seen in Figure 6.1. Chips as small as 5 μm by 5 μm were repeated redundantly with varying bridge lengths. Chip alignment structures for the multilayer devices were also placed on the mask. The final mask area was 5 square inches, with 4 square inches of usable area.

Several of the structures on the mask were single antennas, filters, and waveguides. The larger devices were lower frequency sensor systems, but their area proved difficult for device manufacturing process, and so were eventually discarded as avenues of study.

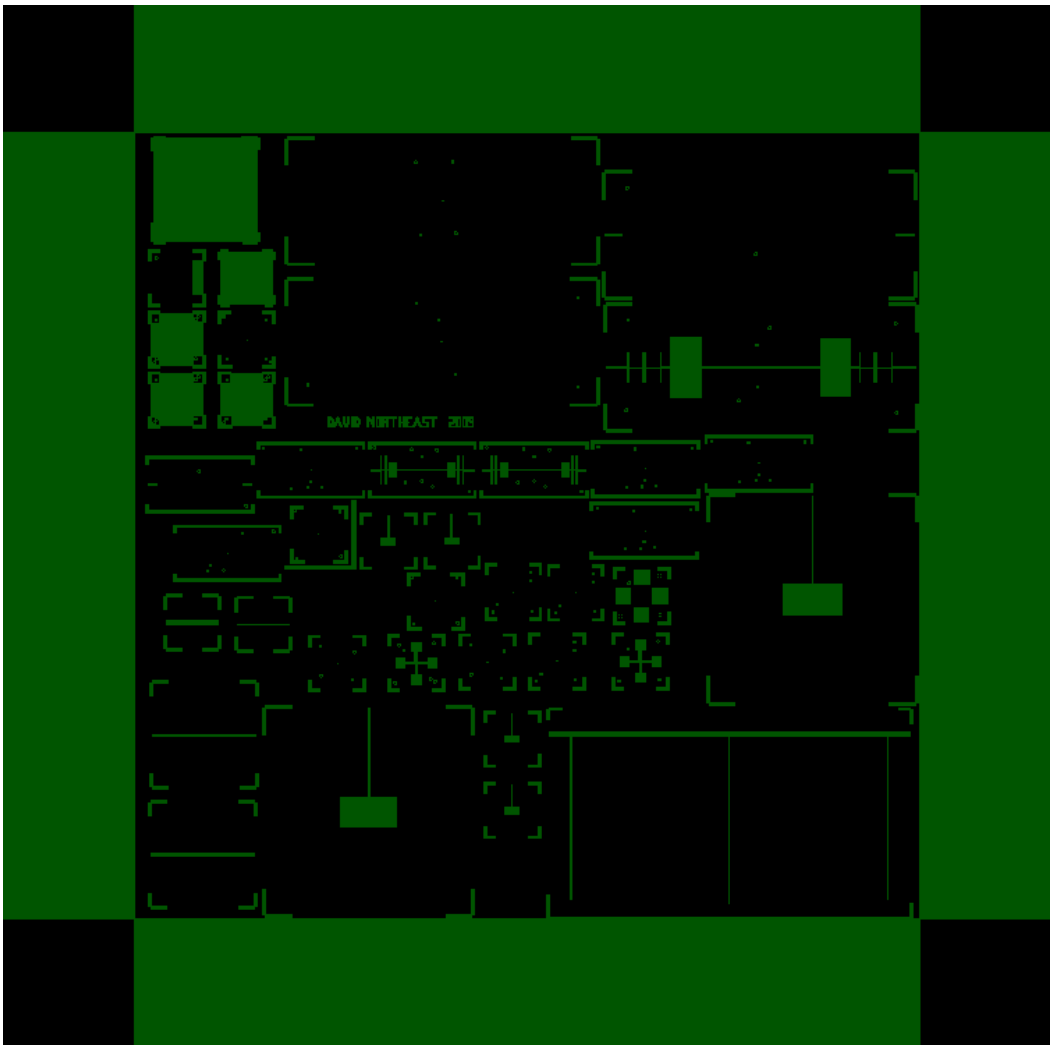

Figure 6.1: The layout of the chrome mask. The green areas represent sections with chrome remaining. The black sections are clear mask sections.

6.1 Substrate preparation

The substrates used for the devices depends on the superconductor used. Silicon with a (100) crystal orientation is used with niobium since the substrate is relatively inexpensive and various thicknesses can be bought commercially. For YBCO, the most convenient substrate was found to be magnesium oxide. $YB_2C_3O_{7-\delta}$ crystals grow on MgO substrates with (100) orientation so the c-axis is oriented perpendicular to the crystal face. Conduction is confined in the ab-plane [55], which is lightly anisotripic with low δ values [56]. The lattice mismatch for YBCO (9 %) is large with MgO compared to other substrates, such as ZrO_2 (1.3 %) [55], but the commercial availability and price make MgO the substrate of choice for YBCO fabrication in this thesis.

6.1.1 Silicon

Two different substrate thicknesses were used: 135 μm intrinsic silicon for the microstrip line devices and 400 μm high-resistivity p-doped silicon for the twin slot and coplanar devices. Five 2 inch in diameter instrinsic (high purity) silicon wafers were bought from Siltronix (of France). Five 4 inch in diameter high-resistivity p-doped wafers were bought from Seiger consulting (of Germany).

Samples are prepared with a Karl Süss dicing machine. They are diced to the desired dimensions with an estimated accuracy of 50 μm. The microstrip antennas and filters are fabricated on silicon chip with 5 mm by 10 mm dimensions, while the twin slot antennas were fabricated on 5 mm by 5mm silicon chips.

6.1.2 Magnesium oxide

Magnesium oxide crystals were also used with two thicknesses. The microstrip-based devices were fabricated on 250 μm crystals, while the twin slot devices on 500 μm thick crystals. All were purchased from MTI Corporation. The chip dimensions were the same for the twin slot case (5 mm by 5 mm) but changed to 10 mm by 10 mm for the microstrip devices due to commercial crystal size availablility.

The crystals were not diced as all attempts to do so caused significant cracking along unintended paths.

6.1.3 Photoresist

Two types of photoresist were chosen depending on whether the process is positive or negative. A positive photoresist (Rohm and Haas 1818) was used with argon ion milling to develop extremely thin layers. A negative photoresist (ma-N 1420 Micro Resist Technologies) was used to define thick metallic structures with a lift off process.

The mask aligner used is made by Karl Süss, modified to use an LED camera for visual positioning of the mask and sample.

6.2 Thin-film deposition techniques

Two main types of thin film deposition techniques were used to deposit the material layers. Both are physical vapour deposition methods. For the pure metal layers, a thermal evaporation technique is used to deposit the materials.

Thermal evaporation using a simple heated tungsten boat is possible for gold, silver, and titanium, but is not possible with niobium. The niobium was deposited with electron beam evaporation due to the much higher temperatures needed for evaporation.

The YBCO layers are deposited by sputtering in an inverted cylindrical magnetron.

6.2.1 Thermal evaporation

Thermal evaporation is simply a process where electrical current is passed through a metallic boat or similar container. This container, and any materials held by the container, are heated. The geometry of the container greatly influences its resistance and subsequent temperature that can be reached. The thermal evaporator in the clean room at the Electrical and Electronic department at Stellenbosch University is equipped with a current source that can supply approximately $350 - 400$ A. This is a sufficient current to evaporate

materials such as titanium and chromium when pressures on the order of 10^{-6} mbar is established in the bell jar.

6.2.2 Electron beam evaporation

Since the thermal evaporation equipment used at Stellenbosch University uses a current source that cannot supply enough electrical power through the tungsten boats to reach a temperature to evaporate niobium under a vacuum, electron beam (e-beam) evaporation is used for this purpose. A beam of electrons is focused onto a niobium sample and the small area where the particles hit will be heated. This process can be used to create high quality thin films of materials with extremely high melting points, such and tantalum, tungsten, and niobium. The films produced with this method can, with proper substrate choice and preparation, produce high quality smooth films with large crystal grains.

The e-beam evaporation unit at iThemba labs is capable of depositing several different layers of materials at once.

6.2.3 Cold sputtering

A cold sputtering deposition unit is used to fabricate gold coated mirrors. Argon ions are formed and maintained over a gold-plated target. The ions dislodge gold atoms and these atoms form a film over silicon wafers placed underneath the target. A thickness of a few nanometres is all that is required if one were to make a half-silvered mirror. 500 nm or more is deposited to ensure reflection at 400 GHz based on a skin depth of 125 nm.

The mirrors can be seen in Figure 6.2, resting in wafer holders. Because the mirrors were never placed under any stress or strain, nor vibrated greatly, simply having gold deposited directly onto the substrate sufficed for mirror preparation.

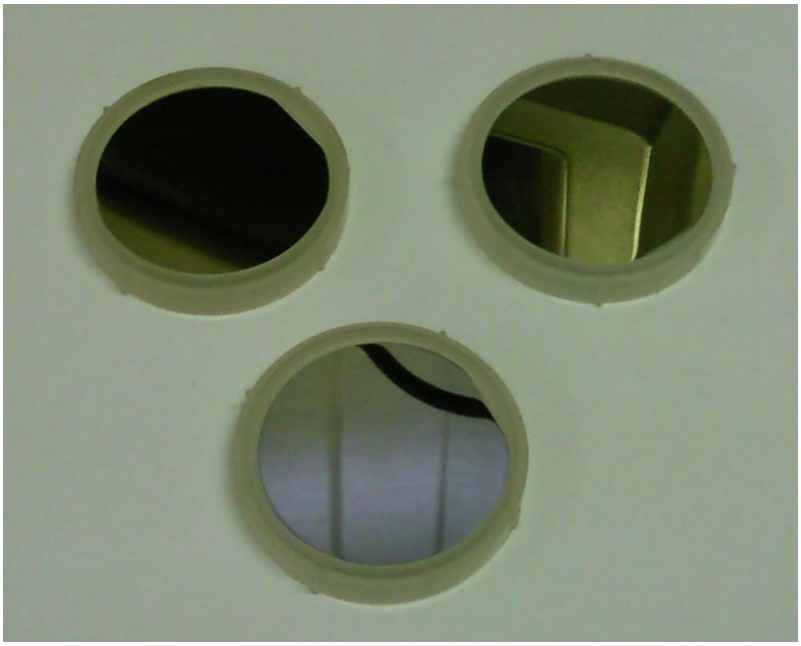

Figure 6.2: Gold mirrors fabricated by cold sputtering. Silicon wafers were used as a substrate for the gold.

6.3 Niobium thin film deposition

The films were deposited at iThemba labs. Silicon wafers were diced, but not broken into pieces. The samples were then placed into the e-beam evaporator and 5 nm to 10 nm of niobium was deposited (depending on sample run). Initial film was checked with electron diffraction spectroscopy (EDS) at Stellenbosch University's Geological sciences department (Table 6-I). The expected film thickness was 5 nm.

Table 6-I: The elemental percent weight of the prepared niobium samples.

Sample	Oxygen	Silicon	Niobium
1	4.302356	85.16728	10.53036
2	4.246296	85.20116	10.55255
3	4.339324	85.23415	10.42653

As expected, silicon provides the largest percent weight of a sample (so

far as the electrons can penetrate). The presence of oxygen can be explained oxidation of a small thickness of the substrate surface, but oxidation of niobium was not ruled out. Subsequent films deposited at iThemba were coated with 5 nm of gold as a protective layer, before the vacuum of the e-beam evaporator was lifted.

6.4 YBCO film preparation

The films of YBCO were prepared by sputtering with an inverted cylindrical magnetron. A prepared target of yttrium, barium, and copper is abrased with a mixture of argon ion and oxygen gas. A cleaned MgO sample is kept at 740°C in this environment while the film is deposited to an expected 100 nm. After deposition, the temperature is then lowered to 700°C, where the argon gas is switched off and the oxygen gas intake is slowly increased to maximum when 700°C is reached. The film is then held in this oxygen environment while slowly cooling to 450°C over 2 to 3 hours. The oxygen source is then switched off and the substrate and film then cooled to room temperature.

The magnetron sputtering and argon ion milling system is seen in Figure 6.3. The device base has three separate heads that attach depending on operational use. The cylindrical metal top seen in the figure is the argon ion head.

After deposition, the YBCO films are stored in tight containers containing several silica gel dessicant packages before being coated with the subsequent normal metal layer.

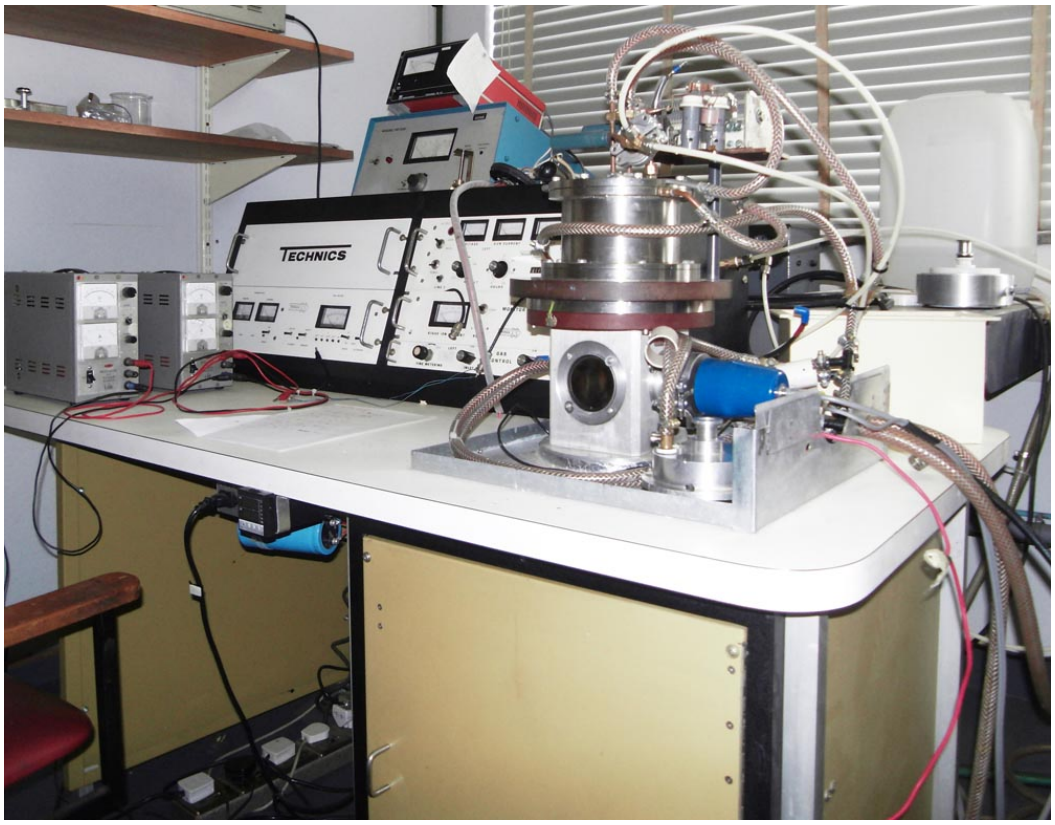

Figure 6.3: The ICM sputtering and argon ion milling system. The device in the picture was set up to run as an argon ion mill.

6.5 Bridge definition

The photoresist is spun on the substrate at 3000 RPM for 30 seconds. The chip is then baked for 1 minute at 120°C. The superconducting bridge is defined with positive photoresist and the chrome mask by being exposed to a UV source for 30 seconds. The device is then immersed in a developer for 30 to 45 seconds to remove the unwanted photoresist area.

The photoresist remaining on the bridge is inspected to ensure a proper bridge structure. Figure 6.4 shows how a proper bridge structure should look when defined with negative photoresist.

After the photoresist is applied and is defining the bridge structure, the sample is placed into the argon ion mill. The exposed areas of the bridge are removed at an estimated milling rate of 2 nm/min. This means an estimated milling time of 2.5 to 5 minutes for Nb, depending on whether the film is 5

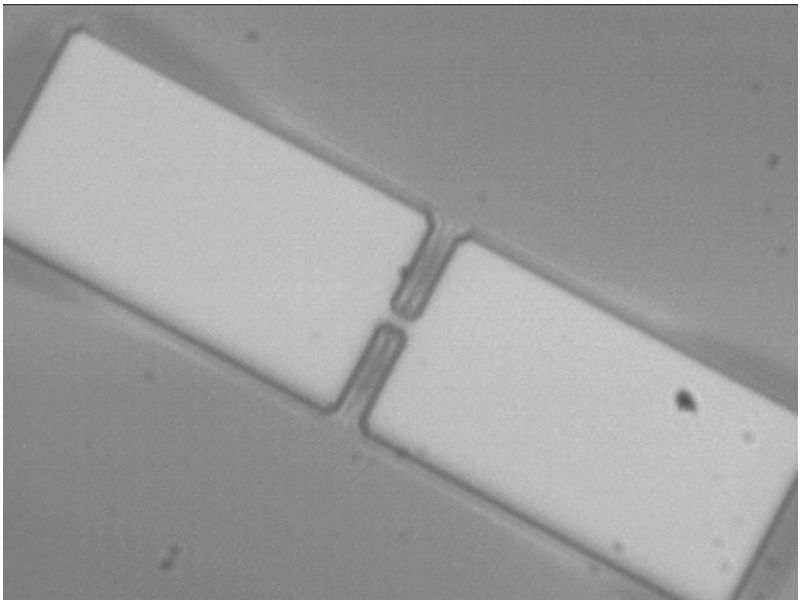

Figure 6.4: A negative photoresist definition of a 5 μm by 1.5 μm bridge.

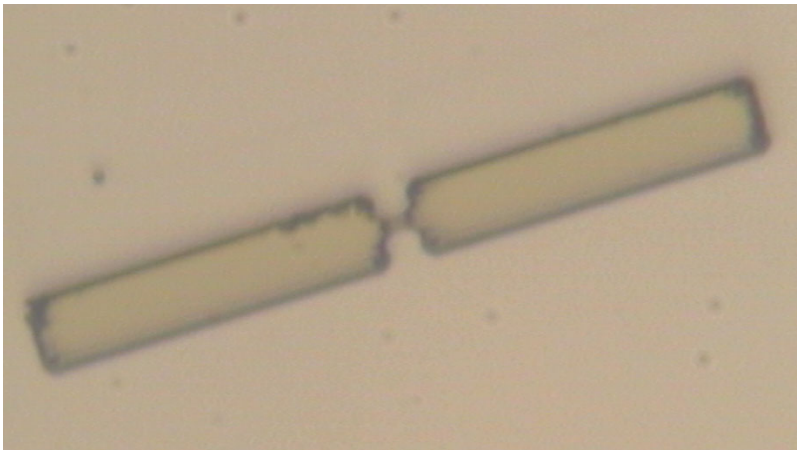

Figure 6.5: A 2 μm by 1 μm Nb bridge defined by argon ion milling.

or 10 nm thick. The film was milled for 7 to 10 minutes to ensure complete removal. The YBCO film was milled for about 50 minutes, pausing once every 5 minutes to allow the photoresist to cool. After 50 minutes of milling, the sample is inspected to see if any YBCO remains where it was intended to be removed. Further 1 minute milling sessions are used if necessary, pausing to inspect after each.

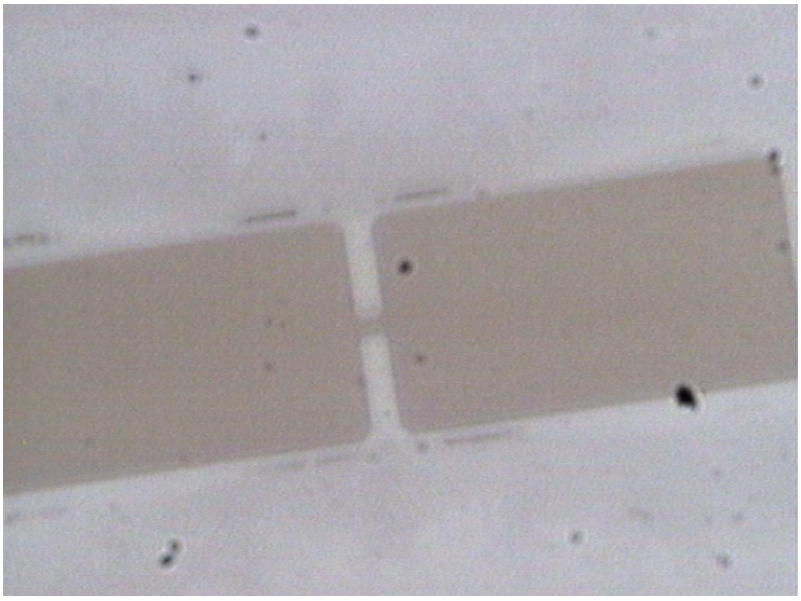

Figure 6.6: A 2 μm by 1 μm Nb bridge defined by argon ion milling.

Two niobium bridges defined in this manner are seen in Figures 6.5 and 6.6.

YBCO bridges are seen in Figures 6.7 and 6.8. The first is intended for 60 GHz systems, while the second in the 400 GHz twin slot device. Of note is the varied size of the contact pads, which is scaled to better fit with the scale of the waveguide lines with which the bridges are to couple.

The YBCO bridges were analysed with an atomic force microscope (AFM). This allowed for analysis of surface roughness as well as a determination of layer thickness. The scanning area was roughly 44 μm^2 and the measurements were made on a vibration isolation table.

A bridge intended to be coupled with microstrip waveguides is seen in Figure 6.9. The image shows a well-defined bridge and smooth surface profile.

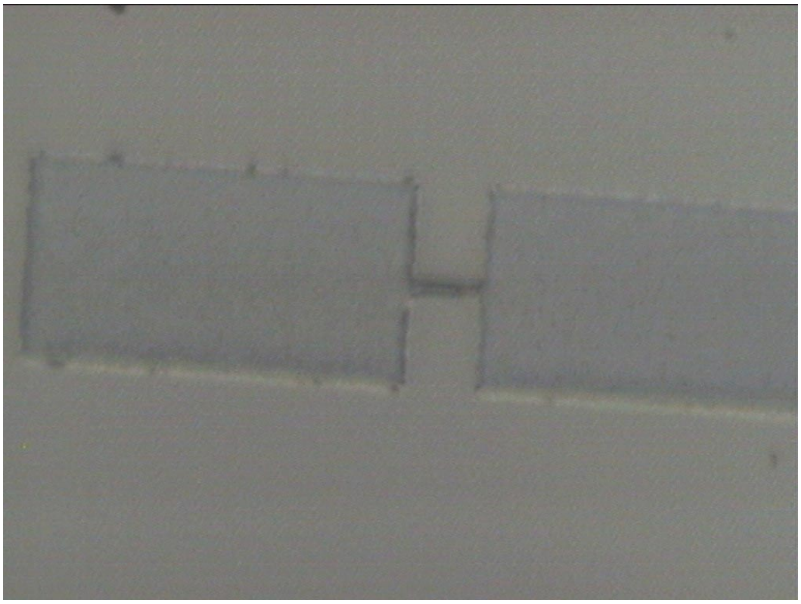

Figure 6.7: A 2 μm by 10 μm bridge made from YBCO.

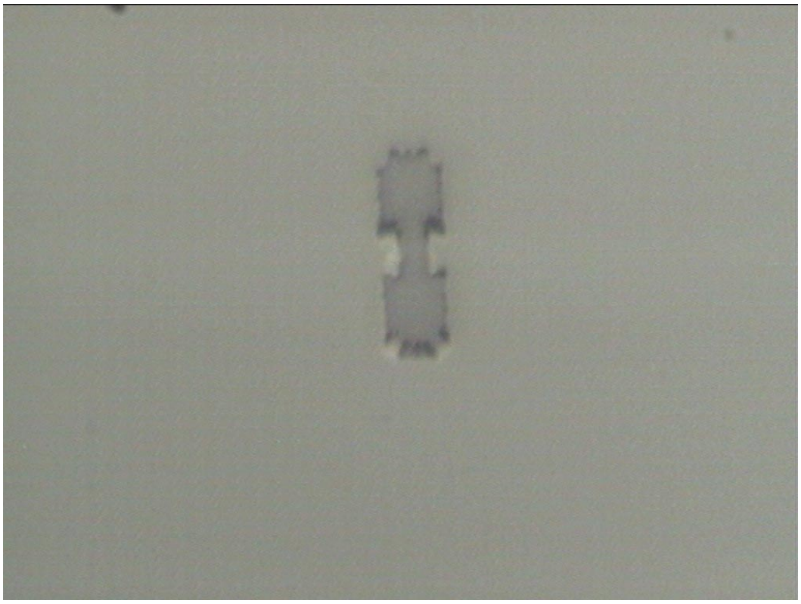

Figure 6.8: A 1 μm by 2 μm YBCO bridge for use in a 400 GHz system.

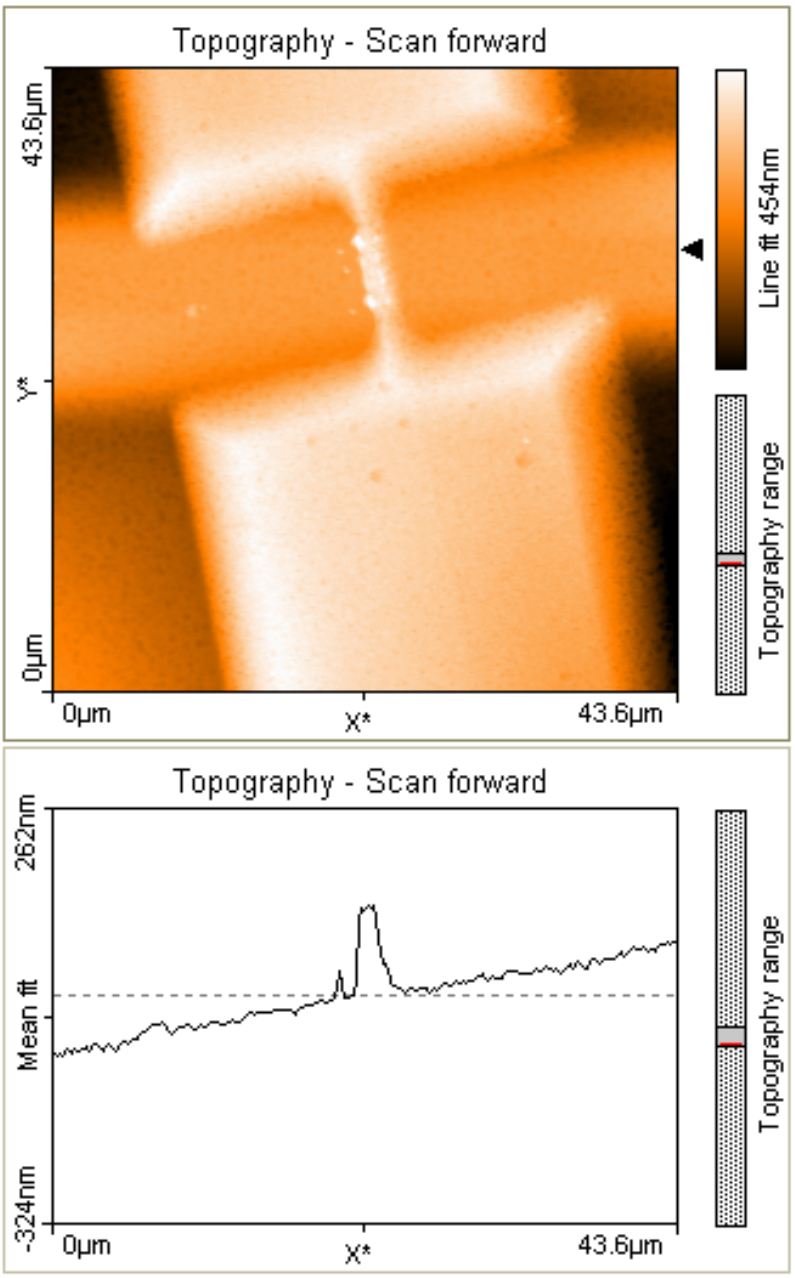

Figure 6.9: A 10 μm long YBCO bridge with YBCO contact pads. The bottom image shows the cross sectional profile according to a slice made where the black arrow is located in the top image.

The thickness, according to the AFM measurements indicate a film thickness of 127 nm at the centre of the bridge. All bridges were milled for longer than it takes to mill 100 nm of YBCO, so is is believed that some of this height is due to some of the MgO substrate being milled.

Bridges intended for coupling with coplanar waveguides can be seen in Figures 6.10 and 6.10. The magnetron sputtering deposition does not produce films as smooth as does the thermal evaporation method. This is apparent when inspecting the cross sectional profile of the remaining YBCO.

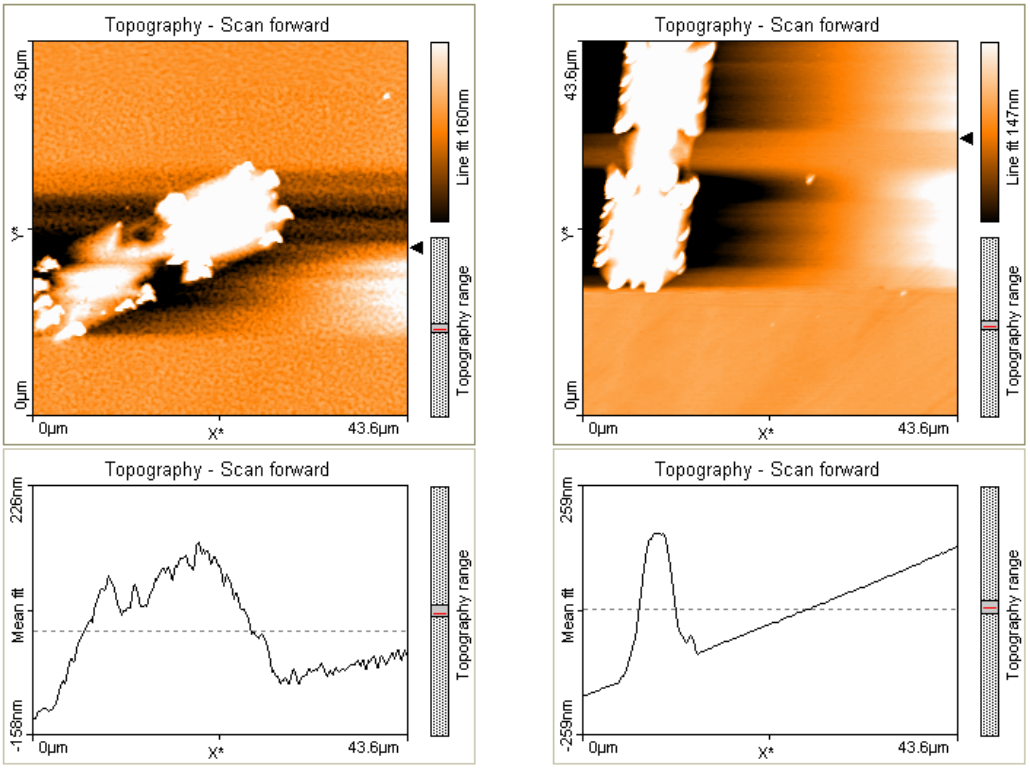

(a) Profile across YBCO contact pad.

(b) Cross sectional profile across bridge.

Figure 6.10: Two YBCO bridges intended for coupling with 400 GHz twin slot antennas. The bottom images show the cross sectional profile according to a slice made where the black arrow is located in the top images.

6.6 Normal metal layers

The antenna, filters and waveguide structures were made with either gold of silver on the respective substrates. These highly conductive metals adhere poorly to the silicon or magnesium oxide crystals, so better adhesion was sought by way of an intermediate metal layer[1]. Titanium, chromium, or niobium all suit this role. Niobium was not chosen since this would potentially lead to unforeseen problems below the metal's T_c. Chromium and titanium will not become superconducting under any of the operational conditions. Since titanium has a lower melting point, it was chosen for easier deposition.

The chips with the superconducting bridges were cleaned again and negative photoresist applied. The ma-N 1420 was spun on at 3000 RPM for 30 seconds. It was baked at 120°C for 2 minutes. The chip was exposed under the chrome mask to UV light for 100 to 130 seconds then developed for 50 to 70 seconds to develop an undercut structure in the resist. The chips were then exposed to UV light without a mask for 5 minutes, then baked again at 120°C, to harden the resist for the physical vapour deposition.

The chips were placed in a 5 chip sample holder and placed in a thermal evaporation unit. Two boats were placed under the samples. One contained powdered titanium and the other contained gold or silver. Both titanium and the noble metal layer must be deposited without ever exposing the titanium to oxygen. The titanium would quickly oxidize and form an insulating layer to which gold or silver adheres poorly.

5 to 15 nm of titanium was deposited first onto the resist-covered substrate. Then 380 to 480 nm of noble metal was deposited on top of this, depending on the intended operating frequency. If 60 GHz is the intended operating frequency, according to (2.63), the skin depth will be 30 nm at 10 K, and will be 12 nm at 400 GHz. This represents 13 to 33 times the skin depth of the material at this temperature (1.5 to 3 times at room temperature), depending on operating frequency. Because this layer was also used as the wire bonding layer, this thickness was required to allow the gold bonds to stick to the chip surface.

[1]Another method is to heat the substrate/metal interface to its eutetic point, where the two will diffuse together, forming tight bonds. It is unknown if this would work with gold and MgO as this method was not investigated.

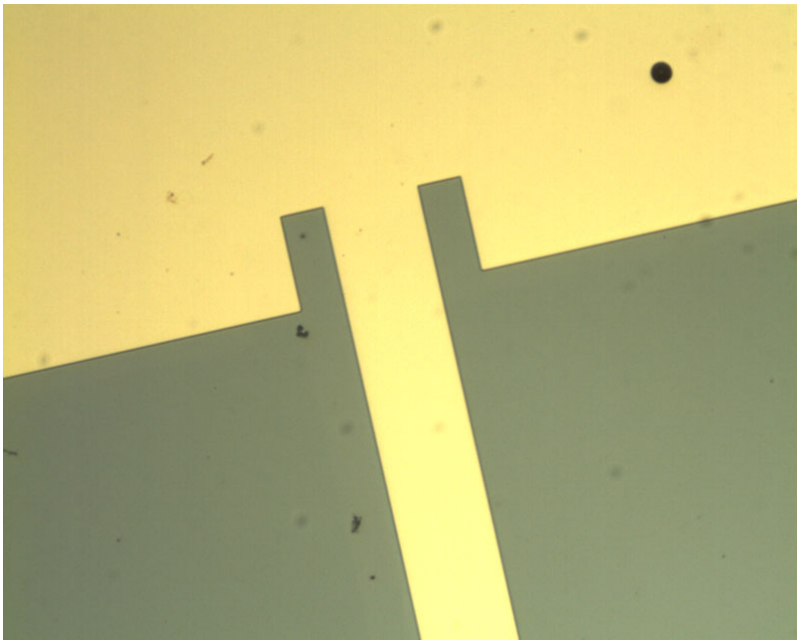

Figure 6.11: A microscope image of a microstrip antenna. The antenna and the impedance matching notches connecting with the microstrip line feed to the bridge are seen.

After metal deposition, the samples are allowed to cool to room temperature while under vaccuum (especially the silver). They are then taken and immersed in acetone. If the photoresist has properly formed undercut structures, the unwanted metal surfaces will lift off completely, with only mild by-hand shaking necessary to dislodge them. With very fine structures or when undercut photoresist is not properly formed, a few short (5 seconds maximum) burst in an ultrasonic bath will dislodge unwanted sections. With a proper titanium underlayer, the gold will adhere completely to the substrate, even under long periods of ultrasonic bath exposure. Insufficient titanium underlayering will lead to gold structures tearing or lifting off of the substrate surface.

It was found that complete metal lift off is possible in 5-15 minutes of manual mechanical movements, with only short amounts of ultrasonic use as a last resort.

The gold structures were formed straight unjagged with the lift off process. Figure 6.11 shows a microstrip antenna with impedance matching notches. The structure edges are properly formed with no tearing. One persistent

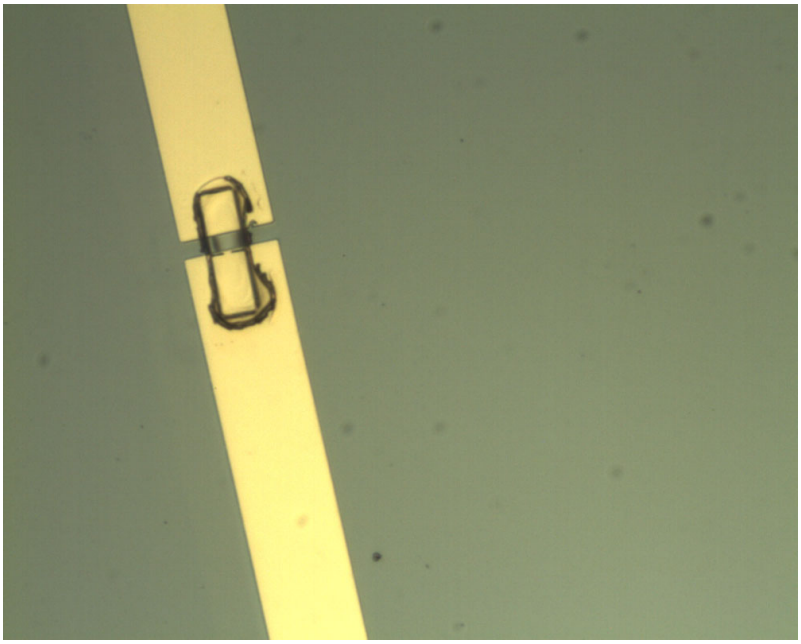

Figure 6.12: A niobium bridge connecting the two gold microstrip lines. The bridge is misaligned which is a consistent problem with the mask aligment system.

problem was misalignment of the bridge to the normal metal layer, as seen in Figure 6.12. Even with mask alignment structures, the optical setup of the mask aligner made it difficult to discern mask/chip alignment better than an estimated ± 5 μm.

Lift off is successful for metal structures down to 5 μm dimensions, as seen in Figures 6.13(a), 6.13(b) and 6.13(c).

The metal layers were also analyzed with AFM scans. Figure 6.14 shows the excellent smoothness of the deposited metal layers. If the photoresist does not have a sufficient undercut profile, the metal layers may form "ear" structures as seen in Figure 6.14. Both images show that the height of the metal layers are near to 400 nm thick, as intended.

An AFM scan of the bridge layered with gold is seen in Figure 6.15. The gold is smooth, and the CPW gaps are well defined. The bridge in this case was formed by over-milling the substrate, hence the high profile.

Since the cleanroom at Stellenbosch University contains a large amount of dust and other particulates, it takes many iterations of photolithography

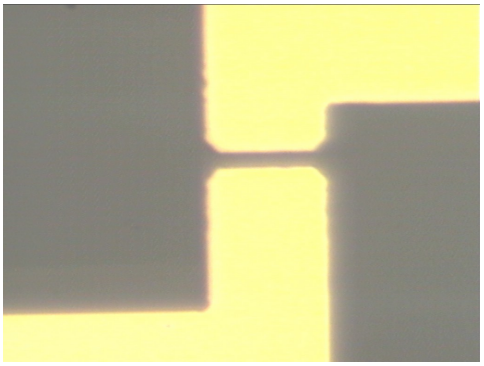

(a) Short CPW filter section.

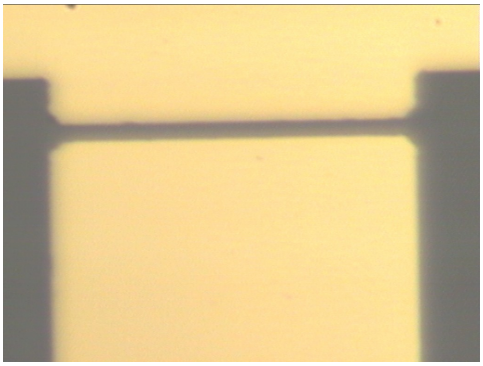

(b) Another CPW filter section..

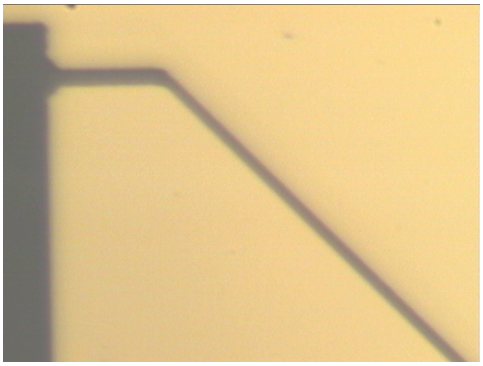

(c) Thin gap.

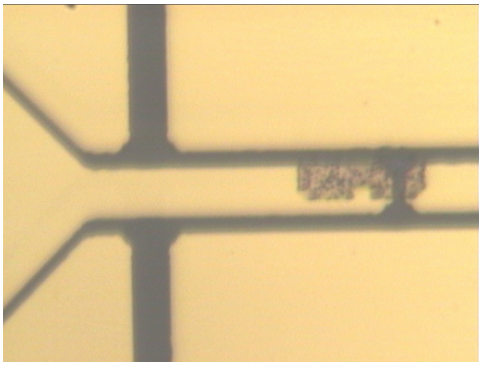

(d) Bridge, antenna and CPW.

Figure 6.13: Four photos showing proper lift off of a 400 GHz antenna and CPW filter on MgO. The problem of bridge misalignment is evident in the last figure.

and deposition of metals to form large, well-formed structures, such as those seen in 6.16. Additionally, the difficulty in aligning multilayer devices makes fabrication of HEBs a difficult task in these facilities.

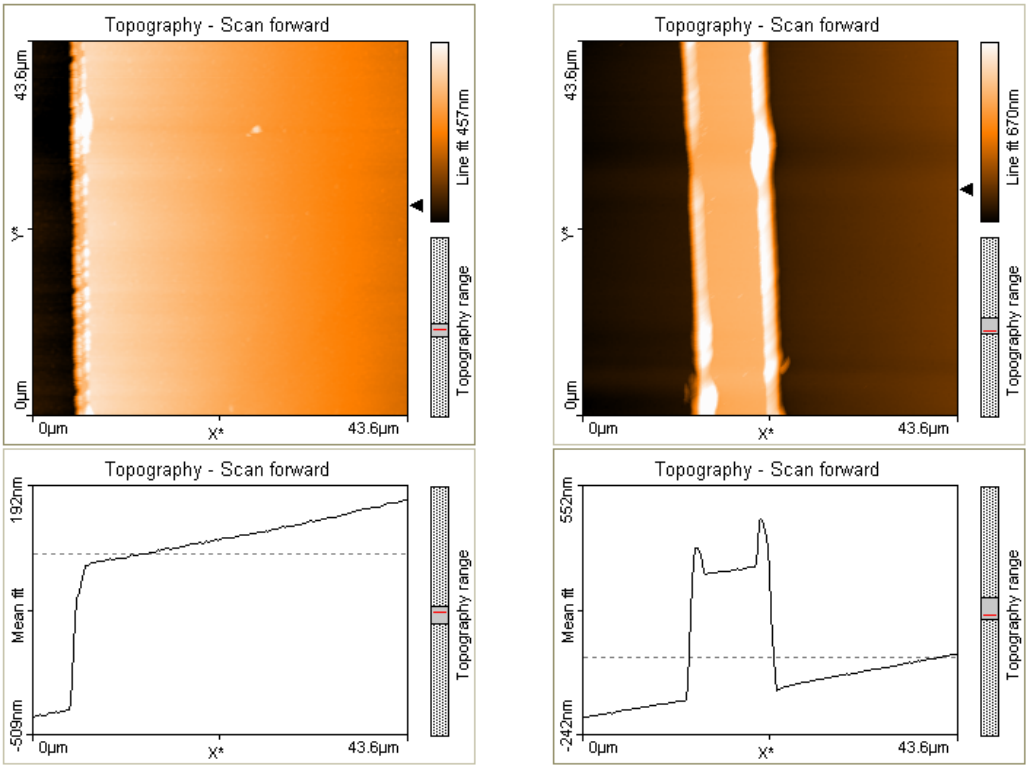

(a) A gold plateau.

(b) A thin gold filter section.

Figure 6.14: Two AFM scans of a gold CPW filter. The first shows a smooth metal plateau structure. The second shows metallic "ears" that can form when the metal is deposited on an insufficiently undercut photoresist layer.

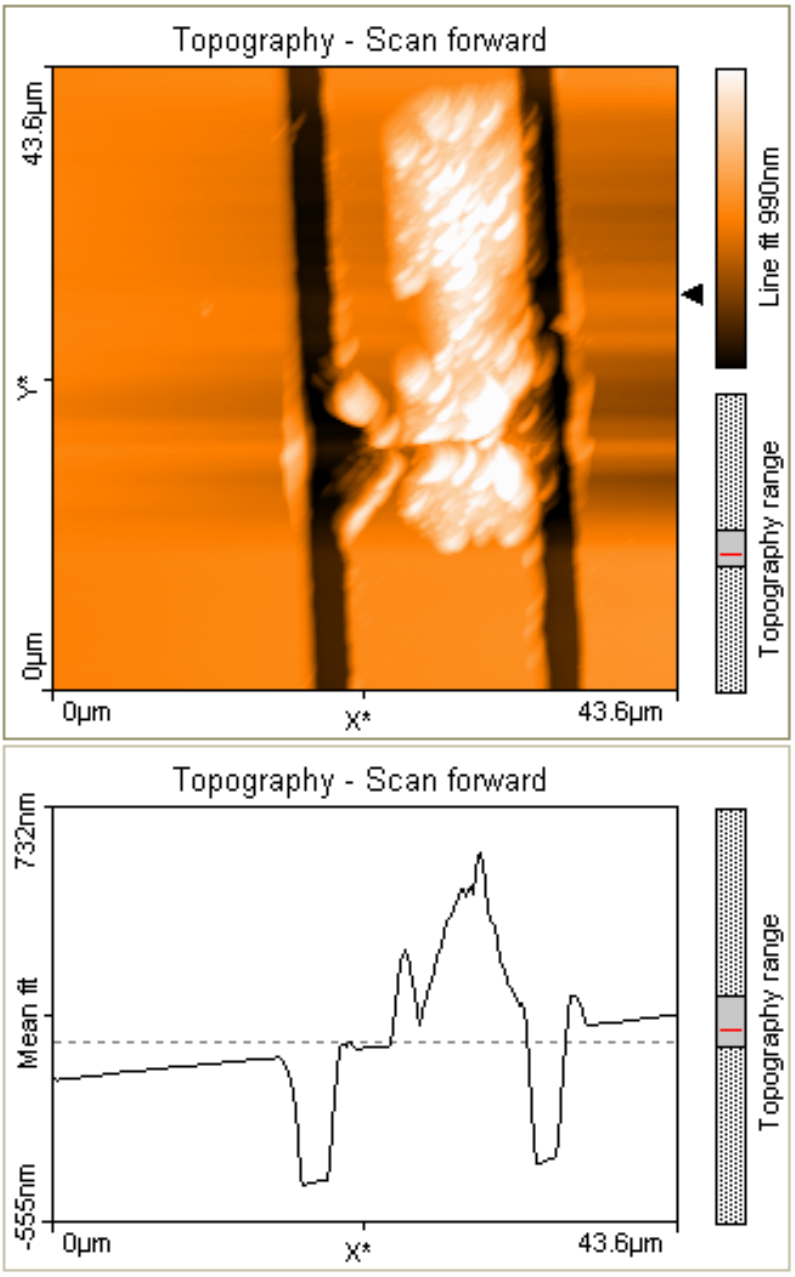

Figure 6.15: An YBCO bridge connecting the centre line of a coplanar waveguide.

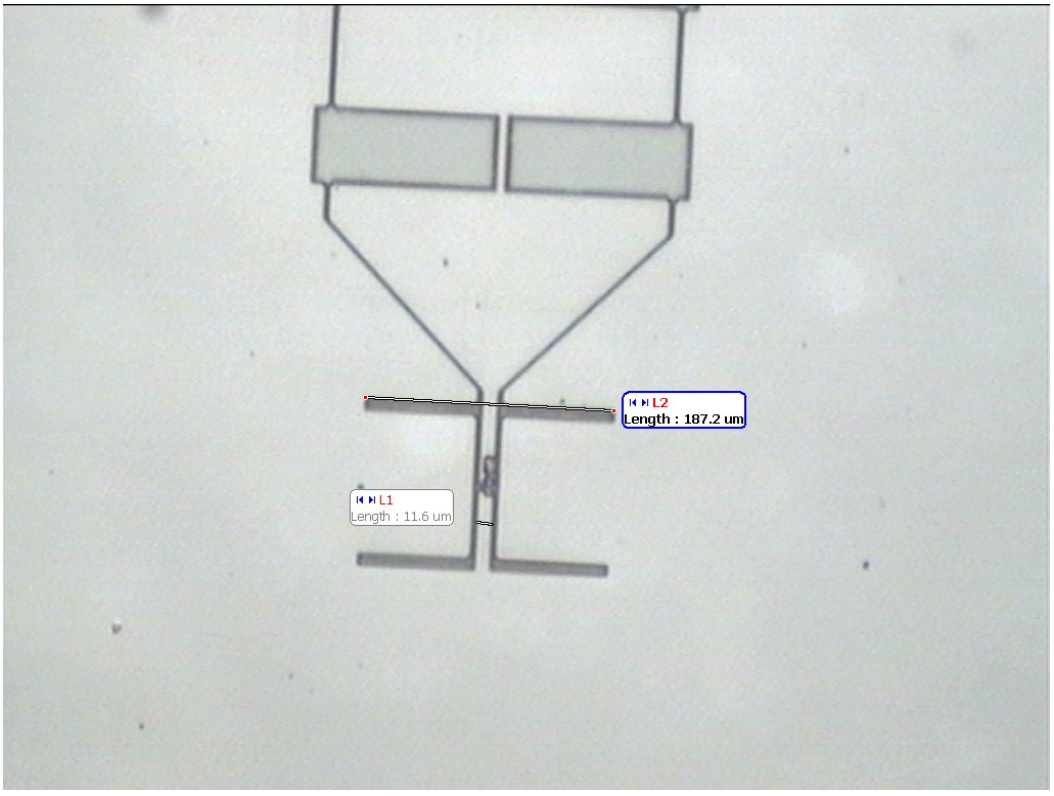

Figure 6.16: A twin slot antenna with a superconducting bridge. Length markers indicate structure lengths.

6.7 Alignment improvement

To use the same equipment as was used in the manufacture of devices presented in this thesis would likely lead one to the same alignment troubles as seen in this chapter. Even with structures intended to aid the alignment of the bridge to the normal metal layer, the bridges would often be completely covered with metal or completely disconnected from the waveguides. The size of the bridge structures need not be altered to allow for improved alignment. If the contact pads of the superconductor are enlarged, and the gap between normal metal waveguides widened[2] (see Figure 6.12 for an example), the small superconducting bridge has a greater chance of being uncovered by the normal metal.

It may become necessary to analyze the waveguide properties of the superconductors at RF frequencies if the length of the bridge and contact pads becomes much larger. It is currently assumed that the waveguides are normal gold conductors right up to the superconducting bridge.

[2]What is meant is clear in the case of microstrip waveguides. For a coplanar waveguide, what is meant is not the gap between the centre conductor and two ground plane sections. The gap between centre conducting sections, with the superconductor bridging the two, is the indicated span.

Chapter 7

Testing and experimental results

An outline of the experimental procedures and the results of the performed tests are presented in this chapter. The test printed circuit boards (PCBs) and the mounting of tests chips onto the brass holders is described first. Then the results of DC superconductivity tests in a cryocooler are described, including voltage and current as the films are cooled down to about 3 K. Similar tests are performed on bridge structures both at DC (without RF stimulation) and under thermal radiation input power.

7.1 Test PCBs

The chips were connected to printed circuit boards that were mounted on brass supports. The boards were manufactured using 10 mil thick Rogers 3203 substrate. This was chosen due to its low loss up to 10 GHz. The PCBs carry biasing and measured signals via microstrip line and grounded coplanar waveguide lines.

SMA connectors are soldered onto the edges where coaxial cables both ground the system and carry the signal through a bias tee to the amplifier chain. If only the DC voltage across the bridge or film is of interest, the SMA centre pin is tapped to supply the current bias and for voltage measurements.

If the circuit is that of the dual microstrip antenna, two SMA connections are needed on either side. One is grounded, and the other carries the IF signal, if present. This means that the bias current is fed and grounded through the centre pin of the coaxial cables. If the twin slot antennas and coplanar

waveguides are tested, only one coaxial cable is needed. The centre pin carries the bias current and any present IF signal, while the ground is provided by the cable shell.

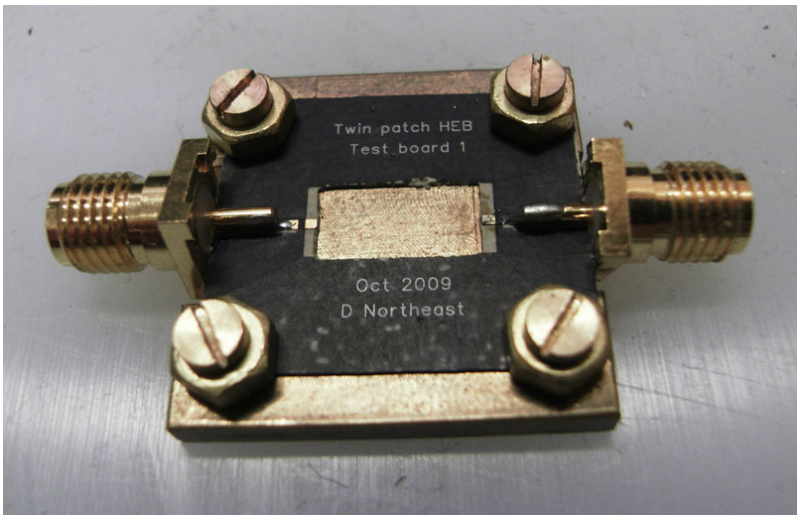

Figure 7.1: An HEB holder with microstrip lines taking the signal to SMA connectors. The PCB is mounded on a brass plate and fastened with brass screws.

The PCBs had the remaining copper metal layer coated with gold to improve wirebonding between the chip and the PCB.

Another PCB was used for DC testing and is seen in Figure 7.3. 48 separate copper tracks were used to wirebond to 5 mm by 5 mm test chips. In the figure, a 5 silver contact pads can be seen with wirebonds connecting them to separate output lines. Each line of 5 contact pads provides an opportunity to perform a four-point resistance test on each side of the film.

The chips are attached to the brass plates with a binary silver epoxy. The bonds are both electrically and thermally conductive, and the chip is securely fastened to allow for wirebonding.

The testing PCBs and their brass plates were affixed to the cryocooler cold finger (Figure 7.4). The circular object located on the surface of the cold finger is the temperature sensor used to estimate the film temperature. Any film or device under test is located underneath this temperature sensor. It was always attempted to prevent the wiring (seen in the background of the photo) from

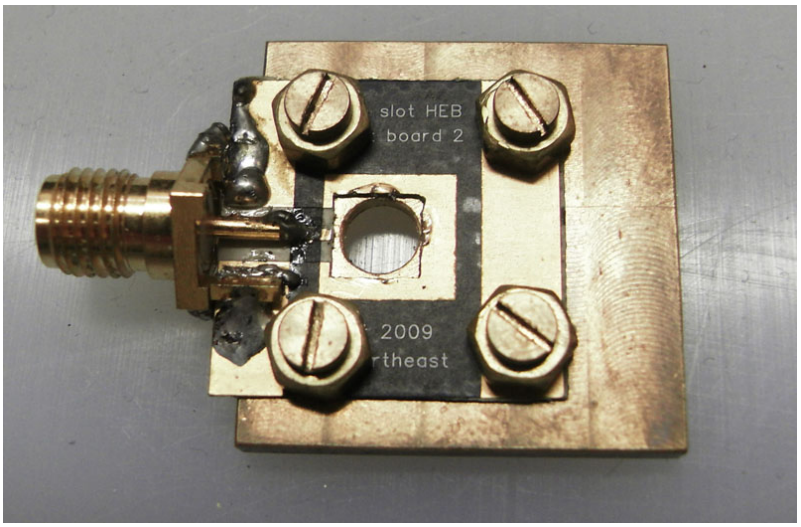

Figure 7.2: A variant with a coplanar waveguide taking the signal to a single SMA connector. The PCB is mounted on a brass place with a hole over which the chip is to be mounded.

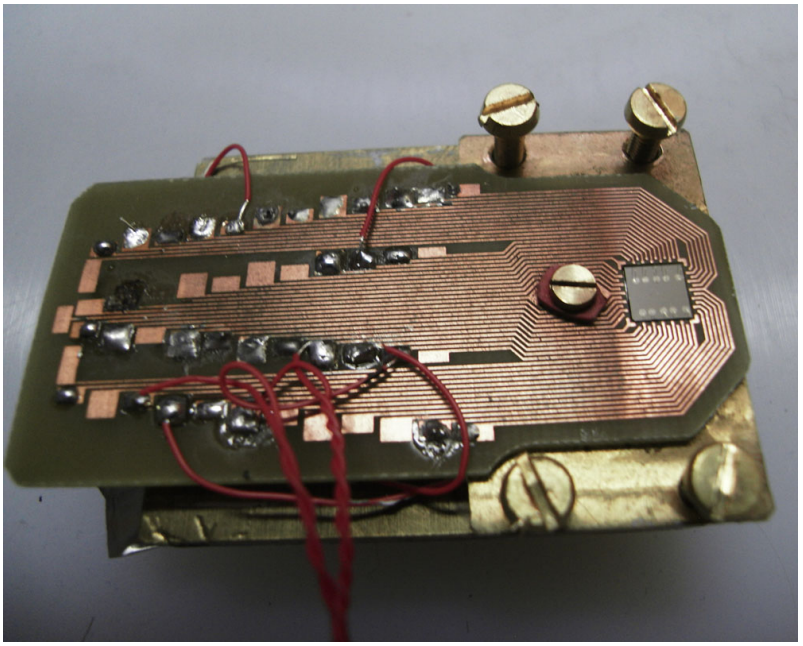

Figure 7.3: A PCB used for DC testing. A chip with a YBCO film is seen in the chip slot. Wirebonds connect the film to various copper tracks on the PCB. The board was made for RSFQ circuits with 48 inputs and outputs.

touching the shielding walls as a test was underway. The black chip is an MgO substate with YBCO thin film.

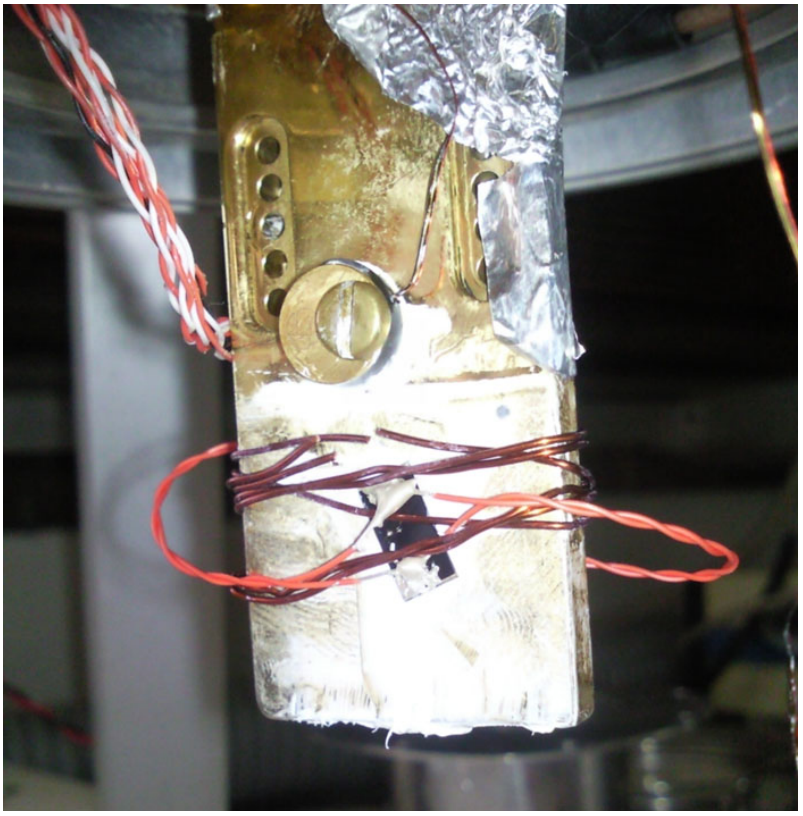

Figure 7.4: The cryocooler cold finger used in all low-temperature film tests.

7.2 DC testing without radiation

Testing of both sheets and milled bridges of Nb and YBCO films were performed with a DC current stimulation. These tests were performed to establish an estimate of the critical temperature, T_c, and critical currents, I_c, of the devices. In the case of DC testing, four-point measurements were used for sheets of films as well as for bridges.

7.2.1 Niobium thin film measurements

The niobium thin films were tested for superconductivity using a four-point probe method, seen in Figure 7.5. The resistance through a section of film can be determined from the voltage drop associated with a current flowing through the film. The films intended for use as HEBs were 5 nm to 10 nm thick, and additional films of 50 nm were also tested. No niobium thin films deposited at iThemba labs showed superconductivity, even down to 2.7 K. Figure 7.6 shows the near approximately linear change in resistance measured as the cryocooler temperature decreases. The data was recorded by hand, and the long sampling period as well as the lag between the recording of temperature, voltage, and current values were the likely reason for the deviations from a smooth curve.

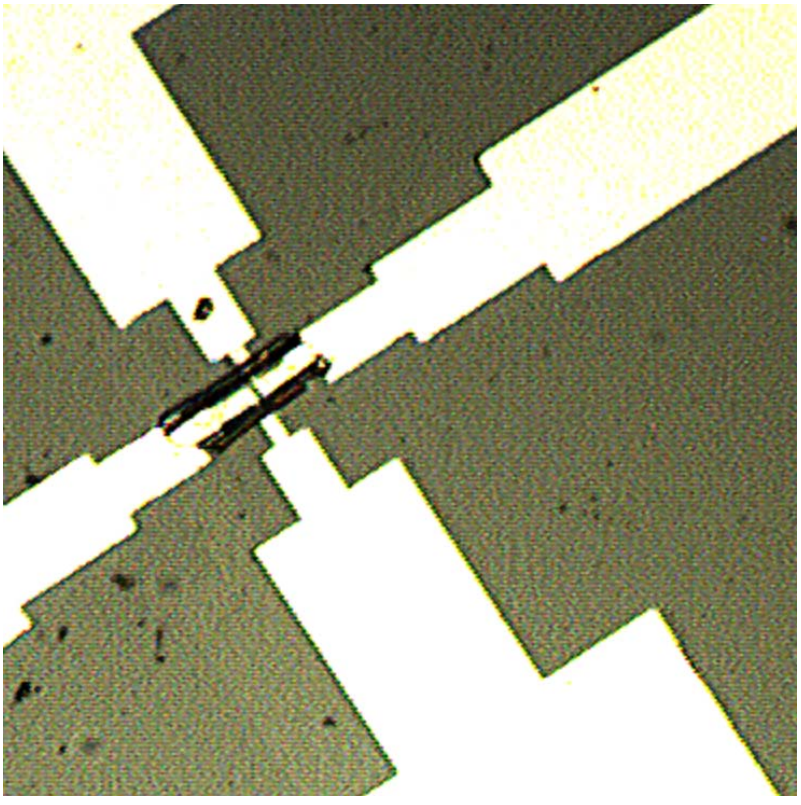

Figure 7.5: A four-point structure to measure the DC properties of niobium superconductive bridges. The normal metal contacts were made of either gold or silver. The latter is seen in this image.

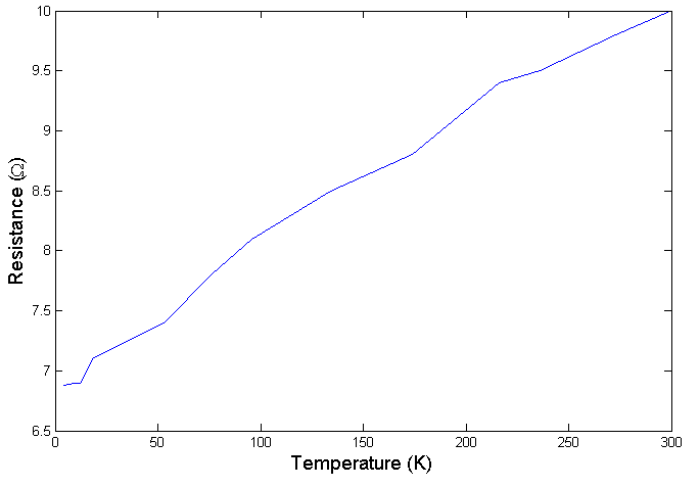

Figure 7.6: The resistance measured across a niobium film as its temperature is decreased from room temperature to below 4 K.

The voltage was measured from a voltmeter while an ammeter monitored the current flowing through the film.

Possible explanations for the absence of a measured superconductive transition include oxidation, which subsequently was inhibited with a gold protective layer deposited on the Nb without breaking vacuum. A consequence of using gold to prevent oxidation of Nb is the suppession of superconductivity. According to [57], Nb only oxidizes in air at 350°C, so the expectation should have been that no significant oxidation occured on the films.

The noise power generated in the cryocooler was also suspected of preventing the film from transitioning to the superconducting state. This was not properly investigated by the author of this thesis as an ongoing dissertation of a collegue was researching the topic.

Magnetic fields could also have prevented superconductivity, or suppressed it such that T_c would occur below a temperature reachable by the cryocooler system. No superconductivity was observed even when magnetic shielding was covering the test samples.

The quality of the deposited films could also be a factor in their failure. The electron diffraction spectrometry measurement seen in Table 6-I indicates high levels of niobium are present on the surface of the substrate. The three elements indicated in the film are merely the three largest elements determined

to be present on or near the surface of the film and substrate and does not rule out any potential contaminant.

High film stress is known to cause a degradation in the superconductive properties of niobium [58]. Since e-beam evaporation is the deposition of a hot metallic vapour onto a substrate, mechanical stress is formed when this film cools and thermally constracts. The film produced at iThemba labs may have been too mechanically stressed to enter the superconductive phase. One solution for this is to deposit the films via magnetron sputtering, which does not depend on the deposited material being in a hot liquid state. Annealing a film deposited by e-beam evaporation may also relieve some of the film stress, but annealing to 750°C did not yield any change in the low temperature properties of the films.

7.2.2 YBCO thin film measurements

The YBCO films were tested for superconductivity via a four-point resistance test, as was the case for the niobium film. The measurements were taken by hand, reading the temperature displayed by the temperature probe closest to the films and quickly recording the voltage as measured by the voltmeter. The plotted resistance curves of three YBCO films can be seen in Figure 7.7.

To lessen the impact the current flowing through a film will have on its T_c, the currents were kept below 100 μA so long as a measureable voltage was formed across the film. The films showed room temperature resistances typically greater than 50 Ω so such small currents generated small mV voltages just before T_c.

T_cs typically fell between 80 K to 88 K, but insufficient observations were made as to the influence of film thickness and YBCO crystal growth conditions. Consequently, the source of both the variation of film resistance and the measured T_c, from sample to sample, was not discovered. If the YBCO film growth process is standardized, an empirical relation may enable resistivities to be tailored to desired values.

Once the cryocooler reached its lowest temperature, the current through the films were varied and the voltage measured between two inner bonding pads. The expectation was for there to be no voltage until the critical current for the film, I_c, is exceeded. Once the current is greater than I_c, the voltage

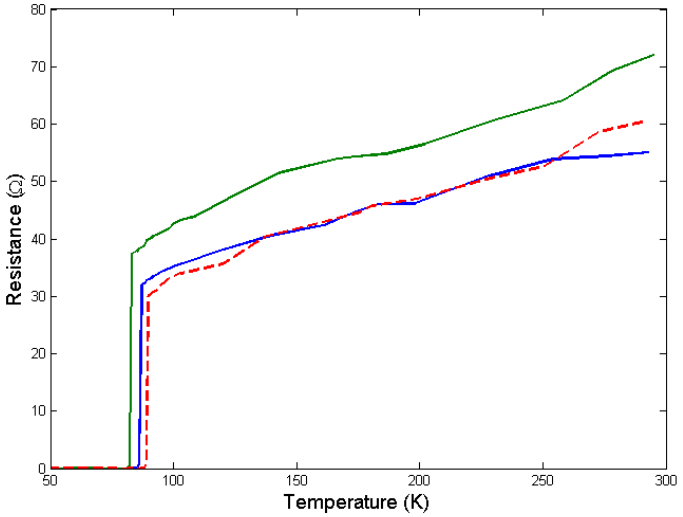

Figure 7.7: The resistance of three YBCO films as their temperature is lowered from room temperature to below their T_cs. The starting resistances of YBCO films varied greatly, as did the T_cs.

should jump, indicating the transition to the normal state. Further increases in current should produce a linear increase in the measured voltage. Figure 7.8 shows that this does indeed occur with YBCO film. The film in the figure shows what appears to be two periods of normal resistive increase with increasing current. If the YBCO beneath the contact pads is suppressed due to the contact with a normal metal, this region would have a lower I_c than the resist of the film. I_c for this particular film appears to be about 25 mA, but only 15 mA in the suppressed regions.

The two-step normal to superconductivity transition, assumed to be due to superconductivity being suppressed under the contact pads, was not observed in the T_c measurements. The likely reason for this is a lower measurement resolution for the R-T curves. The measurements were made in a dynamic system, with the temperature continuously decreasing. Since the measurements were recorded by hand, any double transition may appear to be a single transition. This would especially be the case for small currents, where the speed of the temperature decrease and the lower dynamic change of the measured voltage retard the double transition.

YBCO bridges were fabricated and DC tests were conducted on both four-

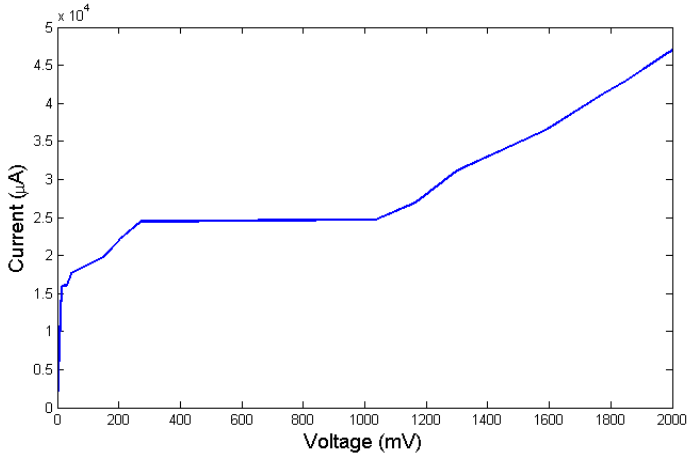

Figure 7.8: The DC *I-V* curve for a YBCO thin film. The result is typical of four-point measurements for films grown to a minimum of 90 nm.

point structures (as in Figure 7.5) and on the bridges connected to the waveguides and antenna structures. It was found that the argon milling of the YBCO film produced bridges that did not transition to a superconducting state, even down to around 3 K. It is thought that the heating caused by the argon milling process may damage the remaining YBCO crystal.

Water is also needed to stop the resist developer and define the normal metal layers for the lift off process. Water damages YBCO [55] and the brief exposure of water with the film may have been enough to completely inhibit superconductivity. The use of another, non-reactive liquid to stop the development of the photoresist may be a better choice for use with YBCO thin films. The existance of such a chemical material group (photoresist, developer, developer inhibitor, and resist remover) is not currently known by the author.

7.3 Testing with thermal radiation

The effect of thermal radiation impinging onto the sensors was investigated despite the absence of HEBs with superconducting bridges. Since no great sensitivity was expected without superconductivity, self-interference of the thermal radiation in a Michelson-type interferometer was deemed unnecessary. The tests were performed only on 400 GHz twin slot devices due to the larger

possible input power from the SiC source[1].

A view of a twin slot device can be seen in Figure 7.9, where the view of the underside of an MgO substrate is observable. The twin slot antenna will radiate into the substrate, necessitating the inclusion of the hole in the brass holding plate. The 50 Ω coplanar waveguide can be seen running along in the gold ground plane. Near the centre, at the end of the 50 Ω waveguide, the low-pass stepped impedance filter is just noticable. The antenna structure is too small to be seen in the photograph.

The devices were biased with 50 μA to 100 μA of current. Illuminating the HEB with a minimum estimate of 100 nW of radiation showed no change in voltage across the signal line. Since the bridges were entirely in the normal conductive state, sensitivity depended entirely on the normal resistance varying with the input power. The small change in resistance provided by the thermal radiation, if indeed there was such a change, was too small to be measured by the test equipment.

[1]The EM power emitted from the surface of a blackbody, while theoretically comprised of all frequencies, contains much more from 400 GHz than 60 GHz. See (2.64).

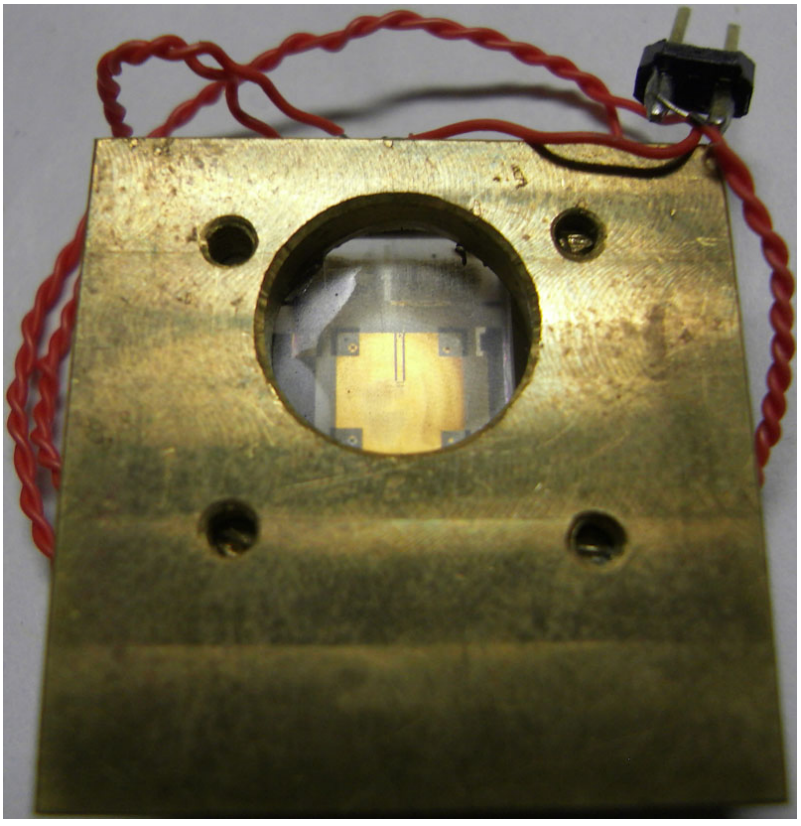

Figure 7.9: The underside of an MgO substrate. The gold ground plane and coplanar waveguide can be seen unside the circular hold in the brass plate. The twin slot antenna is located in the centre of the gold square.

Chapter 8

Conclusions and recommendations

The theory, design, and manufacture of HEB devices has been reported in this thesis. This chapter serves as a summary of the previous chapters, as well as a vehicle to convey recommendations for future work done in this area. While the testing of devices failed to show working sensors, a guide and foundation for doing so has been presented.

8.1 Thesis summary

In Chapter 2, a description of superconductivity, particularly the two-fluid model, was outlined with emphasis on frequency dependence. A general description of bolometers and more specific formulations on the operations of phonon-based and diffusion-based hot electron bolometers can be used to predict sensor performance and, along the following theory on frequency mixing, high-frequency signal detection. In order to successfully fabricate devices intended for high-frequency operation, material behaviour was discussed. Finally, the theory behind, and operation of, Fourier transform spectroscopy devices tells how one might operate an HEB to gather spectral information to both identify material composition and to verify HEB performance.

The design and simulation of microstrip and twin slot antennas and low-pass filters is discussed in Chapter 3. HEBs require low-pass filters for the retention of high-frequency radiation within an area containing the supercon-

ducting bridge. If used as a mixer, the filter must allow for the passing of the intermediate frequency, and this is demonstrated in the scattering parameter plots. The antennas simulations show the radiation efficiency of the devices as well as the direction of efficient radiation detection.

HEB simulations based on heat balance equations and input RF power from the antennas allows for an estimate on the device responsivity and the conversion gain of HEB mixers. Chapter 4 presented temperature profiles of the electrons found across a superconducting bridge. The variation of these temperature profiles to input DC and RF power was presented in detail for both niobium and YBCO bridges.

Antenna and bridge simulations present the performance of a single element in the entire system. Chapter 5 outlines designs of both mixer and spectroscopy devices. The choice of system components, such as amplifiers and optical equipment, presents the general process for constructing and experimenting with HEB.

The process of manufacturing HEBs, from film deposition to device patterning, in Chapter 6 outlines how HEBs were fabricated in Stellenbosch University facilities. AFM scans show the profile of deposited and patterned structures.

Finally, the testing of superconducing film and fabriated HEB devices was shown in Chapter 7. While the realization of a working HEB was not demonstrated, the first steps toward working HEB devices fabricated at Stellenbosch University were made. The next section draws conclusions from the results and recommendations are made that may allow for the success of projects following from this work.

8.2 Recommendations for future work

Detection of higher frequencies will allow for more input thermal power from a SiC rod. The lift off process showed no difficulties defining metallic structures down to 5 μm dimensions. With the appropriate photoresist and mask, smaller normal metallic structures may be successfully fabricated. The higher frequency radiation will better fit the heat balance models used in the simulations.

If the same mask aligner is to be used, greater alignment tolerance must be factored into any mask designs. This does not necessarily mean that device features must be larger to increase successful manufactured samples. For instance, creating a wider gap between the centre conducting lines of a coplanar waveguide would require larger contact pads for connection with the detection bridge. A small bridge that is located on this larger conduction connection will have more chance to be uncovered by the surrounding normal metal layer contacts. If the gap is large enough, analysis of superconducting microstrip lines and coplanar waveguides may be required to ensure proper device operation will occur.

Until electron beam lithography is available to allow for consistent submicron structure fabrication, bridge dimensions are constrained to be greater than 1 μm. If large signal bandwidths are desired, the use of pure niobium on silicon, assuming the material can be brought into the superconducting state, is not recommended if maximum signal bandwidth is desired. Niobium nitride and niobium titanium nitride are both known to have significantly smaller τ_{e-p} when grown on Si substrates. Investigation of the performance (as dictated by the phonon escape times into the substrate) of niobium on MgO or other substrates may allow for continued use of the pure metal.

This project lacked clear design specifications, hampering the approach to a specific solution for a specific problem. Any continuation of this project at Stellenbosch University should begin with a firm system and environment in mind before the design of a sensor should begin. HEBs can perform well in a variety of applications, but the performance and equipment needs can vary greatly. Detection of astrological signals requires the utmost sensitivity and low noise, while detection of radiation from local bodies being imaged or for spectroscopy may allow for, as an example, larger device volumes and less sensitivity, but more active imaging using mm-wave of THz-wave sources to illuminate an object.

Device performance (signal intensity versus frequency or wavenumber) can be estimated from the use of careful experiment with Fourier transform spectroscopy. Such a system is ideal for discovering absorption peaks in materials, which can lead to the identification of many different chemicals. The use of a local oscillator and frequency mixing will be a faster and simpler method of

producing images of objects. To experiment on such a process, obviously such a local oscillator must be acquired.

References

[1] Badenhorst, L.R.: *Cryogenic Amplifiers for Integrating superconductive Systems to Room Temperature Electronics*. Master's thesis, University of Stellenbosch, December 2008.

[2] Hansen, H.J.: Standoff detection using millimeter and submillimeter wave spectroscopy. August 2007.

[3] Penubag: Electromagnetic spectrum. *Wikipedia*, 2008. http://en.wikipedia.org/wiki/Electromagnetic_spectrum.

[4] H. Liu et al: Terahertz spectroscopy and imaging for defense and security applications. In: *Proceedings of the IEEE*, vol. 95, pp. 1514 – 1527. August 2007.

[5] Fischer, B.M., Helm, H. and Jepsen, P.U.: Chemical recognition with broadband thz spectroscopy. August 2007.

[6] D. Santavicca et al: A far-infrared fourier transform spectrometer with an antenna-coupled niobium bolometer. In: *Superconductor Science and Technology*, vol. 20, pp. S398 – S402. November 2007.

[7] Berry, E.: Risk perception and safety issues. *Journal of Biological Physics*, vol. 29, 2003.

[8] Luukanen, A.: Bolometers and terahertz imaging. In: *Microsensing Seminar*, p. 25. March 2006.

[9] Hajenius, M.: *Terahertz heterodyne mixing with a hot electron bolometer and a quantum cascade laser*. Ph.D. thesis, Delft University of Technology, 2006.

[10] Orlando, T.P. and Delin, K.A.: *Foundations of Applied Superconductivity*. Addison-Wesley Publishing Company, Massachusetts Institute of Technology, 1991. p.p. 1 - 15.

[11] Rohlf, J.W.: *Modern Physics from a to Z0*. John Wiley and Sons, Inc., 1994.

[12] Kittel, C.: *Introduction to Solid State Physics.* John Wiley and Sons, Inc., 1996.

[13] Zhou, S.-A.: *Electrodynamics of Solids and Microwave Superconductivity.* John Wiley and Sons, Inc., 1999. p.p. 242 - 244.

[14] Zhou, S.-A.: *Electrodynamics of Solids and Microwave Superconductivity.* John Wiley and Sons, Inc., 1999. p.p. 341 - 347.

[15] Zhou, S.-A.: *Electrodynamics of Solids and Microwave Superconductivity.* John Wiley and Sons, Inc., 1999. p.p. 315 - 340.

[16] Bedorf, S.H.: *Development of Ultrathin Niobium Nitride and Niobium Titanium Nitride Films for THz Hot-Electron Bolometers.* Ph.D. thesis, University of Cologne, December 2005.

[17] Floet, D., Miedema, E., Baselmans, J., Klapwijk, T.M. and Gao, J.: Resistive states of superconducting hot-electron bolometer mixers: charge-imbalance vs. hotspot. *IEEE Transactions on Applied Superconductivity*, vol. 9, pp. 3749 – 3752, June 1999.

[18] Datesman, A.M.: *Fabrication of a Superconducting Hot-Electron Bolometer Receiver with Micromachined Waveguide Components.* Ph.D. thesis, University of Virginia, August 2005.

[19] Prober, D., Burke, P., Bumble, B. and LeDuc, H.: Superconducting teraherz mixer using a transition edge microbolometer. In: *Proceedings of the 1993 International Semiconductor Device Research Symposium.* December 1993.

[20] Conwell, E.M.: *High Field Transport in Semiconductors.* Acedemic Press, 1967.

[21] Sze, S.: *Heat and Thermodynamics.* John Wiley and Sons, Inc., 2002. p.p. 48 - 51.

[22] D. Floet et al: Hotspot mixing: A framework for heterodyne mixing in superconducting hot-electron bolometers. *Applied Physics Letters*, vol. 74, no. 3, pp. 432 – 435, January 1999.

[23] Brewster, H.D.: *Heat and Thermodynamics.* Oxford Book Company, 2009. p.p. 21 - 29.

[24] Zmuidzinas, J.: Coherent detection and sis mixers. In: *Proceedings of the Far-IR, sub-MM, and MM Detector Technology Workshop*, pp. 149 – 154. Montery, CA, April 2002.

[25] Ganzevles, W.F.M., Swart, L.R., Gao, J.R., de Korte, P.A.J. and Klapwijk, T.M.: Direct response of twin-slot antenna-coupled hot-electron bolometer mixers designed for 2.5 thz radiation detection. *Applied Physics Letters*, vol. 76, no. 22, pp. 3304 – 3306, May 2000.

[26] M.O. Reese et al: Niobium hot electron bolometer development for a submillimeter heterodyne array camera. *IEEE Transactions on Applied Superconductivity*, vol. 17, no. 2, pp. 403 – 406, June 2007.

[27] M.I. Finkel et al: Terahertz heterodyne receivers based on superconductive hot-electron bolometer mixers. *Radiophysics and Quantum Electronics*, vol. 48, no. 10-11, pp. 859 – 864, January 2005.

[28] Balanis, C.A.: *Advanced Engineering Electromagnetics*. John Wiley and Sons, Inc., 1989. p.p. 72 - 84.

[29] Zhou, S.-A.: *Electrodynamics of Solids and Microwave Superconductivity*. John Wiley and Sons, Inc., 1999. p.p. 40 - 47.

[30] J.C. Schultz et al.: Application of ultra-thin silicon technology to submillimeter detection and mixing. In: *WMSCI Conference 2005*. July 2005.

[31] Li, J. and Li, J.: Dielectric properties of silicon in terahertz wave region. *Microwave and Optical Technology Letters*, vol. 50, May 2008.

[32] Burns, M.J., Kleinsasser, A.W., Delin, K.A., Vasquez, R.P., Karasik, B.S., McGrath, W.R. and Gaidis, M.C.: Fabrication of high-tc hot-electron bolometric mixers for terahertz applications. *IEEE Transactions on Applied Superconductivity*, vol. 7, 1997.

[33] A.D O'Connell et al.: Microwave dielectric loss at single photon energies and millikelvin temperatures. *Applied Physics Letters*, vol. 92, 2008.

[34] Kiwa, T. and Tonouchi, M.: Time-domain terahertz spectroscopy of (100) (laalo3)0.3-(sr2altao6)0.7 substrate. *Japanese Journal of Applied Physics*, vol. 40, 2001.

[35] Archimerged: Permittivity. *Wikipedia*, 2008. http://en.wikipedia.org/wiki/Permittivity.

[36] Walther, M., Cooke, D.G., Sherstan, C., Freeman, M.R. and Hegmann, F.A.: Terahertz conductivity of thin gold films at the metal-insulator percolation transition. *Physical Review B*, vol. 76, September 2007.

[37] Balanis, C.A.: *Advanced Engineering Electromagnetics*. John Wiley and Sons, Inc., 1989. p.p. 149 - 151.

[38] Balanis, C.A.: *Advanced Engineering Electromagnetics*. John Wiley and Sons, Inc., 1989. pp. 62.

[39] Lide, D.R.: *CRC Handbook of Chemistry and Physics*. CRC Press LLC, 2003.

[40] Liddle, A.: *An Introduction to Modern Cosmology*. John Wiley and Sons, Inc., University of Sussex, UK, 2003. p.p. 13 - 15.

[41] Roos, M.: *Introduction to Cosmology*. John Wiley and Sons, Inc., 2003. p.p. 114 - 116.

[42] Steward, E.G.: *Fourier Optics: An Introduction*. Dover Publications, Inc., 2004. p.p. 169 - 188.

[43] Griffiths, P.R. and de Haseth, J.A.: *Fourier Transform Infrared Spectrometry*. John Wiley and Sons, Inc., 2007. p.p. 19 - 49.

[44] Pozar, D.M.: *Microwave Engineering*. John Wiley and Sons, Inc., 1998.

[45] Balanis, C.A.: *Antenna Theory Analysis and Design*. John Wiley and Sons, Inc., 2005. p.p. 816 - 825.

[46] Volakis, J.L.: *Antenna Engineering Handbook*. The McGraw-Hill Companies, 2007.

[47] Lee, M., Li, C., Deaver, B. and Weikle, R.: Nonlinear thz mixing in yba2cu3o7 thin film hot electron bolometers. In: *Proceedings of SPIE*. July 1998.

[48] Kobayashi, H. and Yasuoka, Y.: Slot-array antennas fed by coplanar waveguide for millimeter-wave radiation. *IEEE Transactions on Microwave Theory and Techniques*, vol. 46, 1998.

[49] Shimizu, T., Abe, Y. and Yasuoka, Y.: Thin-film slot antennas for 700ghz submillimeter wave radiation. *IEICE Transactions in Electronics*, vol. E78-C, pp. 1002 – 1006, 1995.

[50] H. Merkel et al: A two-dimensional hot-spot mixer model for phonon-cooled hot electron bolometers. *IEEE Transactions on Applied Superconductivity*, vol. 11, no. 1, pp. 179 – 182, March 2001.

[51] Merkel, H., Khosropanah, P., Yagoubov, P. and Kollberg, E.: A hot spot mixer model for superconducting phonon-cooled heb far above the quasiparticle bandgap. In: *Tenth International Symposium on Space Terahertz Technology*. March 1999.

[52] Gershenzon, E.M., Gol'tsman, G.N., Gousev, Y.P., Elant'ev, A.L., Semenov, A.D. and Pirogovskaya, I.M.: Mechanism of picosecond response of granular ybacuo films to electromagnetic radiation. *IEEE Transactions in Magnetics*, vol. 27, 1991.

[53] Corporation, T.J.S.: Thz materials. Tech. Rep., Tydex J. S. Corporation, 2010.

[54] Hudson, W.R. and Jirberg, R.J.: Superconducting properties of niobium films. Tech. Rep. TN D-6380, Lewis Research Center, NASA, June 1971.

[55] Snetler, L.H.: *High-temperature superconductor step-edge fabrication for the implementation of RSFQ circuits.* Master's thesis, Stellenbosch University, 2005.

[56] Hosseini-Gheinani, A.R.: *The anisotropic microwave electrodynamics of YBCO.* Ph.D. thesis, University of British Columbia, 2002.

[57] Patnaik, P.: *Handbook of Inorganic Chemistry.* The McGraw-Hill Companies, 2003.

[58] Bass, R.B., Lichtenberger, L.T. and Lichtenberger, A.W.: Effects of substrate preparation on the stress of nb thin films. *IEEE Transactions on Applied Superconductivity*, vol. 13, June 2003.

Appendix A

Heat balance simulation code

This is the code used to generate the temperature profiles found in Chapter 4. The constants at the beginning of the Matlab code allows one to change the material parameters and device dimensions. While the temperature is simulated across a bridge, the voltage and resistance is estimated and summed across the length as well.

```
% 4th order Runge-Kutta method with adaptive step size
% The solution is for a second-order BVP heat transfer equation. The
% shooting method is used to reach the appropriate solution for the given
% boundary values
%
% -K*U'(x) + c_e/tau_eph*(T(x) - Tb) = P_rf + j^2*rho(T(x))
%
% U(x) = T'(x)
%
% where P_rf is the power from a high frequency source
% and, in terms of ohmic power loss, proportional to rho0/(1+exp(-(T(i)-Tc1)/
    DeltaT))
% Assumed constants (often for stability):
% gamma           -> constant for electron heat capacity (c=gamma*T*V)
% K               -> thermal conductivity
% current_density -> DC bias current density
% rho0            -> normal state resistivity before transition to
    superconductor
% omega           -> RF radiation source frequency
% V               -> volume

clear
% Input parameters
format long eng
%Tc1 = 78.1; % K, YBCO
Tc1 = 5.95; % K, assume suppressed Tc -> correct for bias, if not small
% 86 YBCO, 6 Nb, unsuppressed
```

```
Tb = 3; % K, bath
Lb = 2e3; % nm
Width = 1e3; %nm
Thickness = 5; %nm
A = Width*Thickness; % nm^2
V = A*Lb; % nm^3
%current = 30e-5; % A
current = 50e-6;
current_density = current/A; % A/m^2
%gamma = 700; % J m^-3 K^-2
gamma = 7e-25; % J nm^-3 K^-2
L = 2.44e-8; % W Ohm K^-2 -> from Wiedemann-Franz law K = L*T/rho(T)
rho0 = 76; % Ohm nm Nb
%rho0 = 1500; % Ohm nm YBCO
omega = 400e9; % Hz
time = 0; % seconds
tau_eph = 1e-9; % seconds (0.625 ns Diff - 1 ns for phonon-cooled)
K = L*Tc1/rho0; % K assumed constant (/2 for Nb)
%K = 1e-9 % W nm^-1 K^-2 for YBCO
DeltaT = 0.2; % Superconducting transition width (0.2 Nb, 0.3 YBCO)
Voltage = 0;% initialize voltage across bridge
Resistance = 0; % initialize resistance across bridg3

% set power P0 for RF power
P0 = 141e-9;

%  max error in temperature
maxerr = 0.0000001;
stepsize = 1;
h = stepsize; % step size
maxbounderr = 0.01; % error tolerance of final boundary temperature
bounderr = 10; % initialize test variable to ensure process starts

% initialize position and counter
i = 1; % counter
x(i) = 0; % x starts at zero and goes to Lb

% initialize Temperature (T) and dummy variable (U)
T(i) = Tb;
Uinit1 = 0.00138; % first guess for initial change in temperature
Uinit2 = 0.0005; % second guess for initial change in temperature
U(i) = Uinit1;
iteration = 1; % counter for shooting method
TbLast = 0;
ULast = 0;


while bounderr > maxbounderr % continue until second boundary condition met
    while x(i) < Lb % go once along bridge length

        err = 2*maxerr;
```

```
while abs(err) > maxerr % continue while error is too large

    % determine if T is above Tc and use appropriate equations

    % using step size as h
    h1 = h;
    k1T = U(i);
    k1U = (gamma*Tc1/(2*tau_eph*K))*(T(i)-Tb)-(P0/K)*(0.5+0.5*cos(omega*
        time))/V-(current_density^2*rho0/K/(1+exp(-(T(i)-Tc1)/DeltaT)))
        ;
    k2T = U(i)+h1*k1U/2;
    k2U = (gamma*Tc1/(2*tau_eph*K))*((T(i)+h1*k1T/2)-Tb)-(P0/K)
        *(0.5+0.5*cos(omega*time))/V-(current_density^2*rho0/K/(1+exp
        (-((T(i)+h1*k1T/2)-Tc1)/DeltaT)));
    k3T = U(i)+h1*k2U/2;
    k3U = (gamma*Tc1/(2*tau_eph*K))*((T(i)+h1*k2T/2)-Tb)-(P0/K)
        *(0.5+0.5*cos(omega*time))/V-(current_density^2*rho0/K/(1+exp
        (-((T(i)+h1*k2T/2)-Tc1)/DeltaT)));
    k4T = U(i)+h1*k3U/2;
    k4U = (gamma*Tc1/(2*tau_eph*K))*((T(i)+h1*k3T/2)-Tb)-(P0/K)
        *(0.5+0.5*cos(omega*time))/V-(current_density^2*rho0/K/(1+exp
        (-((T(i)+h1*k3T/2)-Tc1)/DeltaT)));
    % estimation of solution using RK parameters and h1
    T1 = T(i) + (k1T + 2*(k2T + k3T) + k4T)*h1/6;
    U1 = U(i) + (k1U + 2*(k2U + k3U) + k4U)*h1/6;


    % using step size as h/2
    h2 = h/2;
    k1T = U(i);
    k1U = (gamma*Tc1/(2*tau_eph*K))*(T(i)-Tb)-(P0/K)*(0.5+0.5*cos(omega*
        time))/V-(current_density^2*rho0/K/(1+exp(-(T(i)-Tc1)/DeltaT)))
        ;
    k2T = U(i)+h2*k1U/2;
    k2U = (gamma*Tc1/(2*tau_eph*K))*((T(i)+h2*k1T/2)-Tb)-(P0/K)
        *(0.5+0.5*cos(omega*time))/V-(current_density^2*rho0/K/(1+exp
        (-((T(i)+h2*k1T/2)-Tc1)/DeltaT)));
    k3T = U(i)+h2*k2U/2;
    k3U = (gamma*Tc1/(2*tau_eph*K))*((T(i)+h2*k2T/2)-Tb)-(P0/K)
        *(0.5+0.5*cos(omega*time))/V-(current_density^2*rho0/K/(1+exp
        (-((T(i)+h2*k2T/2)-Tc1)/DeltaT)));
    k4T = U(i)+h2*k3U/2;
    k4U = (gamma*Tc1/(2*tau_eph*K))*((T(i)+h2*k3T/2)-Tb)-(P0/K)
        *(0.5+0.5*cos(omega*time))/V-(current_density^2*rho0/K/(1+exp
        (-((T(i)+h2*k3T/2)-Tc1)/DeltaT)));
    % estimation of solution using RK parameters and h1 at mid-point
    T2 = T(i) + (k1T + 2*(k2T + k3T) + k4T)*h2/6;
    U2 = U(i) + (k1U + 2*(k2U + k3U) + k4U)*h2/6;
    x2 = x(i) + h2;

    % using step size as h/2 and mid-point values
```

```
    k1T = U2;
    k1U = (gamma*Tc1/(2*tau_eph*K))*(T2-Tb)-(P0/K)*(0.5+0.5*cos(omega*
        time))/V-(current_density^2*rho0/K/(1+exp(-(T2-Tc1)/DeltaT)));
    k2T = U2+h2*k1U/2;
    k2U = (gamma*Tc1/(2*tau_eph*K))*((T2+h2*k1T/2)-Tb)-(P0/K)*(0.5+0.5*
        cos(omega*time))/V-(current_density^2*rho0/K/(1+exp(-((T2+h2*
        k1T/2)-Tc1)/DeltaT)));
    k3T = U2+h2*k2U/2;
    k3U = (gamma*Tc1/(2*tau_eph*K))*((T2+h2*k2T/2)-Tb)-(P0/K)*(0.5+0.5*
        cos(omega*time))/V-(current_density^2*rho0/K/(1+exp(-((T2+h2*
        k2T/2)-Tc1)/DeltaT)));
    k4T = U2+h2*k3U/2;
    k4U = (gamma*Tc1/(2*tau_eph*K))*((T2+h2*k3T/2)-Tb)-(P0/K)*(0.5+0.5*
        cos(omega*time))/V-(current_density^2*rho0/K/(1+exp(-((T2+h2*
        k3T/2)-Tc1)/DeltaT)));
    % estimation of solution at next interval using RK parameters and
    % h2 at mid-point
    T3 = T2 + (k1T + 2*(k2T + k3T) + k4T)*h2/6;
    U3 = U2 + (k1U + 2*(k2U + k3U) + k4U)*h2/6;


    % use estimation of the temperature error to determine if step size
    % should be changed and to modify solution

    err = T3 - T1;

    % if error is good, else it is too big
    if abs(err) < maxerr
        errfactor = 0.2;
    else
        errfactor = 0.25;
    end

    if err ~= 0
        h = h*(maxerr/abs(err))^errfactor;
    end
    %         if abs(err) > (maxerr/2)
    %            h = h*(maxerr/abs(err))^errfactor;
    %         end
    % this will go till error is acceptable
end

% error is acceptable, update solution
i = i + 1;
x(i) = x(i-1) + h1;
T(i) = T3 + err/15;
U(i) = U3 + (U3-U1)/15;
Voltage = Voltage + current_density*rho0*h1/(1+exp(-(T(i)-Tc1)/DeltaT));
Resistance = Resistance + rho0*h1/(A*(1+exp(-(T(i)-Tc1)/DeltaT)));
disp('position')
disp(x(i))
```

```
        disp('Step size')
        disp(h)
        disp('Initial Temp change')
        disp(U(1))
        disp('Temp(x)')
        disp(T(i))
        disp('maximum T')
        disp(max(T))
        disp('-----')
    end

    % test is boundary error is within tolerance
    bounderr = abs(T(i) - Tb);

    if (bounderr > maxbounderr) && (iteration == 1)
        TbLast = T(i); %store boundary temperature
        ULast = U(1);
        clear T; % clear and reset all variables
        clear U;
        clear x;
        clear Voltage;
        clear Resistance;
        i = 1; % reinitialize counter
        h = stepsize;
        iteration = iteration + 1;
        x(i) = 0;
        T(i) = Tb;
        U(i) = Uinit2; % use second initial guess
        Voltage = 0;
        Resistance = 0;
    elseif (bounderr > maxbounderr) && (iteration > 1)
        TbLastLast = TbLast;
        ULastLast = ULast;
        TbLast = T(i); % store boundary temperature
        ULast = U(1); % store initial change
        clear T; % clear and reset all variables
        clear U;
        clear x;
        clear Voltage;
        clear Resistance;

        i = 1; % reinitialize counter
        h = stepsize;
        iteration = iteration + 1;
        T(i) = Tb;
        x(i) = 0;
        Voltage = 0;
        Resistance = 0;
        % calculate slope to a better initial guess using secant method
        slope = (TbLast - TbLastLast)/(ULast - ULastLast);
```

```
        % calculate better initial guess using secant method
        U(i) = ULast + (Tb-TbLast)/slope;
    end
end

hold all
plot(x,T) % plot solution
hold all

% display calculated voltage and resistance over the bridge
disp('Voltage!')
disp(Voltage)
disp('Resistance!')
disp(Resistance)
disp('DONE!')
```

Appendix B

Manufacturing process

1. Dice silicon wafer into appropriate dimensions.
2. Clean substrates in acetone first with a wipe, then with a 5 minute session in the ultrasonic bath.
3. Rinse substrate clean of acetone with deionized water.
4. Blow substrate dry with pure dry nitrogen gas.
5. Bake substrate in an oven for 30 minutes at 200°C.
6. Blow cool with dry nitrogen gas.
7. Deposit a thin film of titanium[1] by thermal evaporation or niobium[2] by electron beam evaporation.
8. Without breaking vacuum, deposit a thick layer of gold (by thermal evaporation) on the titanium or a thin layer of gold (by electron beam evaporation) on niobium.
9. If required, clean film-coated substrate with a 5 minute acetone soak in an ultrasonic bath.
10. Spin a coat of Shipley S1818 positive photoresist onto the film-coated side of the substrate. 7000 RPM for 30 s.

[1]Titanium acts as an adhesion layer between silicon and metals such as gold and silver.
[2]Niobium adheres nicely with silicon. Intermediate frequency bandwidth increases as film thickness decreases.

11. Bake the substrate on a hotplate heated to 115°C for at least 70 s.

12. Place substrate on the mask aligner stage and position for proper mask design coverage.

13. Expose the photoresist for 15 s.

14. Develop the substrate in developer for 15 s, ceasing development by placing chip under a stream of deionized water.

15. Spin the substrate and blow dry with dry nitrogen.

16. Inspect sustrate and photoresist to determine the presence of a proper photoresist pattern. If malformed structures or aberrations are present, clean in acetone and repeat from step 10.

17. Place substrate in argon ion mill and mill for 5-10 minute sessions. Mill rate is an estimated 2 nm/min for $+1000V$ and $-1000V$ voltage settings.

18. Clean off remaining photoresist with an acetone bath. The ultrasonic bath should be used for a proper cleaning.

19. Spin on ma-N 1420 negative photoresist for 30 s at 3000 RPM.

20. Bake the chip on a 115°C hotplate for 2 min.

21. Align the chip to the desired second layer pattern on the mask and expose the chip for 90 s.

22. Develop the chip for at least 60 s. Longer development creates undercut resist edges, ideal for lift off.

23. Inspect the chip surface to determine the correct formation of the desired pattern and undercut. Small amounts of resist residue can be remove with a very short (5 minute) mill with argon ion gas. Large amounts of unwanted resist is undesirable and in such cases the resist should be removed with acetone and step 18 onwards repeated.

24. Place chip in an appropriate holder in the thermal evaporator and deposit 15 nm of titanium followed by 385 nm of gold (or aluminium or silver).

25. Remove the chip and place it into an acetone[3] bath.

26. When the unwanted metallic sections have swelled[4] on the chip remove them with short (one second[5]) bursts of ultrasonic vibrations from the ultrasonic bath.

27. Mount the chip on a brass testing plate with silver epoxy. The chip must be positioned so that wirebonds can be made from the PCB to the chip.

28. After epoxy has dried, connect the chip to the PCB with wirebonds.

[3]The appropriate proprietary remover can be used for metal lift-off processes, but acetone is found to work just as well or better with the resists used, with no damage to deposited metal layers.

[4]The author notes that many people leave the chips overnight in the acetone or photoresist remover bath so much of the unwanted metal sections are completely without photoresist undersupport. It was observed that so long as the deposited metals were properly adhering to the substrate and niobium, leaving the chip in acetone for hours is unnecessary. Proper patterns can be formed within minutes of deposition.

[5]Running the ultrasonic bath for too long should not remove the metal layers that are adhering well on the silicon. Nevertheless, there is a danger of jagged or crooked edges being formed if the removed metal is energetically torn off by long exposure to ultrasonic vibrations.